

~~NASA CR-~~

166660

101-10056

CR-14444C

"Made available under NASA sponsorship  
in the interest of early and wide dis-  
semination of Earth Resources Survey  
Program information and without liability  
for any use made thereof."

A STUDY OF THE EFFECTS  
OF THE ATMOSPHERE ON  
THEMATIC MAPPER OBSERVATIONS

Prepared for:

National Aeronautics and Space Administration  
Goddard Space Flight Center  
Greenbelt, Maryland 20771

Under NASA Contract NAS 5-23639

(E81-10056) A STUDY OF THE EFFECTS OF THE  
ATMOSPHERE ON THEMATIC MAPPER OBSERVATIONS  
(EG & G Washington Analytical Services)  
139 p HC A07/MF A01

N81-33540

CSCL 08B

Unclas  
G3/43 00056

October 1, 1977

Applied Systems Department Report No. 004-77



REPORT

WASHINGTON ANALYTICAL SERVICES CENTER, INC.  
WOLF RESEARCH AND DEVELOPMENT GROUP

A STUDY OF THE EFFECTS OF THE ATMOSPHERE  
ON THEMATIC MAPPER OBSERVATIONS

Prepared for  
National Aeronautics and Space Administration  
Goddard Space Flight Center  
Greenbelt, Maryland 20771  
under NASA Contract NAS 5-23639

Prepared by  
William A. Pearce  
Wolf Research and Development Group  
EG&G/Washington Analytical Services Center, Inc.  
6801 Kenilworth Avenue  
Riverdale, Maryland 20840

October 1, 1977

Applied Systems Department Report No. 004-77

## TABLE OF CONTENTS

<u>Section</u>	<u>Page</u>
1.0 INTRODUCTION	1
1.1 SIGNATURE CONTAMINATION BY ATMOSPHERIC SCATTERING	3
1.2 MONTE CARLO SIMULATION OF RADIATIVE TRANSFER	6
1.2.1 PHOTON TRANSPORT AND SAMPLING	7
1.2.2 GROUND SCATTERING	13
1.3 MODEL CONDITIONS	18
1.4 THEMATIC MAPPER SPECIFICATIONS	23
2.0 MODEL OBSERVATIONS OF GROUND PATTERNS	25
2.1 AN ALBEDO BOUNDARY - SEMI-INFINITE PLANES	27
2.2 SINGLE SQUARE FIELDS	40
2.3 CHECKERBOARD FIELDS	45
3.0 CALIBRATION EFFECTS	59
4.0 THEORETICAL CONSIDERATIONS	74
4.1 GENERAL FORMALISM	74
4.2 SPREAD FUNCTIONS AND MODULATION TRANSFER FUNCTIONS	79
4.3 IMAGE ENHANCEMENT	98
5.0 THE IMPACT OF THE ATMOSPHERE ON CLASSIFICATION	106
5.1 CLASSIFICATION	110
5.2 CLASSIFICATION ERRORS	114
5.3 RECOMMENDATIONS	130
6.0 CONCLUSIONS	132

## SECTION 1.0

### INTRODUCTION

This report describes a study of the effects of scattering by the atmosphere and the earth on observations of the earth to be made by the Thematic mapper scheduled for launch on LANDSAT-D. The small field of view of the sensors of this instrument, their sensitivities and high radiometric resolution may significantly increase the accuracy of classification achievable by a satellite. Atmospheric scattering of light may, however, present problems that cannot be resolved through instrumental design improvements. It is the object of this study to evaluate the impact of light scattering by the atmosphere and the earth.

Our approach to the problem is to employ a sophisticated Monte Carlo computer code to simulate the transport of radiation from its source (the sun) to the satellite-borne receivers. We can, thus, include the impact of Rayleigh and aerosol light scattering and the scattering of light by the ground both within and beyond the instantaneous field of view of the sensor.

The remaining portion of this section discusses the general problem of signature contamination by atmospheric scattering; the details of the Monte Carlo code employed in this study; the specifications of the details of the model for the atmosphere-earth-receiver system; and, finally, a summary of the specifications of the Thematic mapper.

Section 2 presents the results of a number of simulation studies employing models of the earth's reflectivity which are specifically chosen to illuminate certain effects in a quantitative way. Here, are examined, for example, the effects of a single albedo boundary on the earth, the effects of variable field size, and the effects related to the patchwork character of the earth as viewed from a satellite.

In section 3 we address the problem of calibrating the intensity, i.e., of associating a sensed intensity with a definite albedo.

A general formalism for treating atmospheric scattering is outlined in section 4. Here we introduce the concepts of the atmospheric spread function and the modulation transfer function (MTF). Specific examples are computed for the MTF and its importance as a tool for analyzing total system performance is discussed.

In section 5, we examine the problem of classification and obtain analytical tools which permit the spread function to be used quantitatively to evaluate the impact of atmospheric scattering on classification accuracy. We outline the qualitative features of the impacts of training set sampling strategies, the characteristics of the atmospheric spread function, and heterogeneous albedo patterns.

Finally, in section 6, we outline our conclusions and make a number of recommendations.

## 1.1 SIGNATURE CONTAMINATION BY ATMOSPHERIC SCATTERING

In order to understand the importance of the scattering effects of the atmosphere with respect to observations to be made by the Thematic mapper, let us consider, for the moment, the fundamental basis of remote classification schemes. The basic premise is that the character of an unknown region may be determined by measuring the intensity of light reflected from the region in several wavelength bands. Classification is achieved by identifying the measured spectral intensities with spectral intensities measured for a known region (training field) under similar conditions.

Two basic assumptions are implicit in this process. The first is that the spectral intensities of the light incident on the viewed region are known and fixed; i.e., the same for the viewed region as for the training field. Secondly, it is assumed that all light entering the sensor has been reflected from the viewed region.

Atmospheric scattering effects violate these assumptions to some (often unknown) degree in the following ways:

- 1) Some of the light entering the sensor has been reflected from the ground outside the IFOV and subsequently scattered by the atmosphere into the sensor. This becomes important when the extent and character of the region surrounding the IFOV differ markedly from that for the training field.
- 2) Some light entering the sensor has been scattered by the atmosphere only and has not been reflected from the ground. This may contribute to classification errors in two ways. If the training measurements have been taken from satellite observations when the atmospheric turbidity was different from that

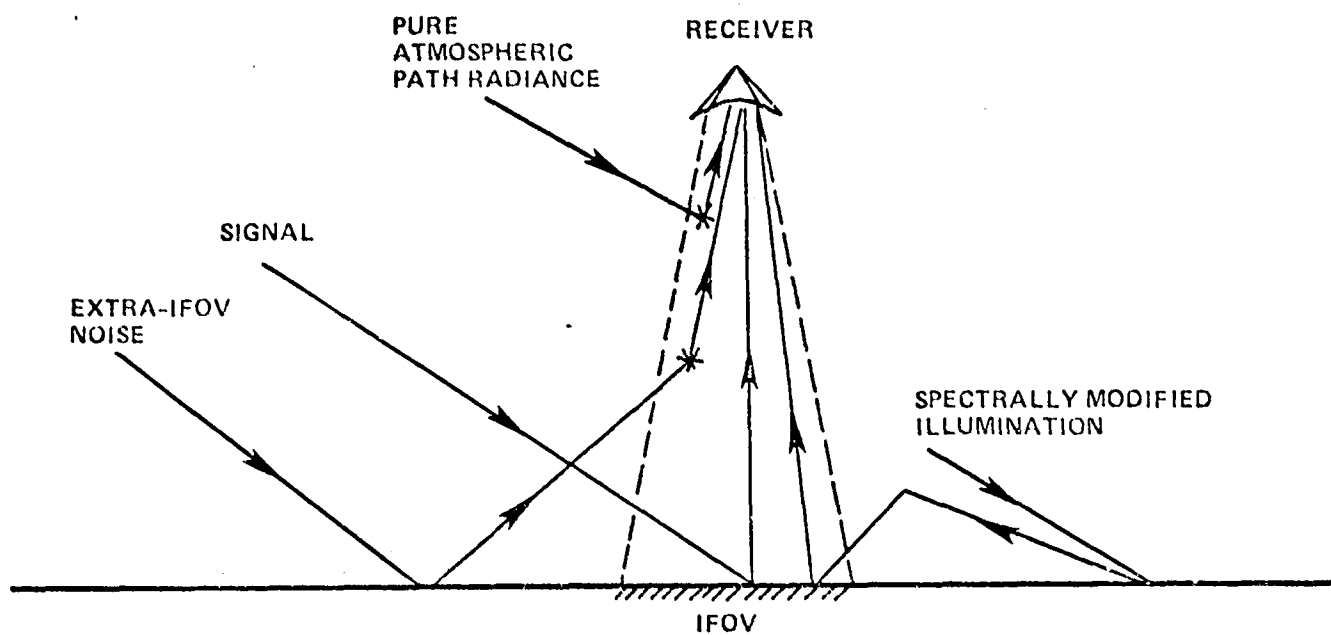


FIGURE 1.1. CONTRIBUTIONS TO THE SENSED RADIANCE

prevailing over the unknown region, then error may be introduced. Secondly, if the training sets are taken from ground level observations purely atmospherically scattered light (path radiance) adds an additional component which must be taken into account to achieve accurate classification.

- 3) Some of the light incident on the viewed region has been spectrally modified by previous reflection from the ground outside the viewed region. This can be important when the area surrounding the instantaneous field of view (IFOV) differs in character or extent from the region surrounding the test field.

Since the effects of pure atmospheric path radiance are moderately well known, this study is primarily focused upon evaluating the influence of the regions surrounding the IFOV which contribute to sensed radiances through atmospheric scattering.



## 1.2 MONTE CARLO SIMULATION OF RADIATIVE TRANSFER

In order to gain an understanding of the impact of atmospheric scattering and varigated ground reflectance patterns on Thematic mapper observations, it is necessary that calculations include consideration of all of the important aspects of the radiative transport of light from the sun to the sensor. The most straightforward means to accomplish this is through Monte Carlo simulation. The code CTRANS (Ref. 1) is well suited to the present task since it possesses the following features:

1. The atmosphere is modeled as plane-parallel and multi-layered with up to 100 homogeneous layers. Each layer may be composed of up to five optically active (scattering or absorbing) species: molecular (Rayleigh) scatterers, aerosols or biases (monodisperse or polydisperse), ozone, etc.
2. Up to 10 finite clouds of rectangular solid shape may be superimposed on the ambient atmosphere.
3. Arbitrarily high orders of atmospheric and ground scattering may be included.
4. The receiver may be modeled as having an arbitrary field of view and may be oriented arbitrarily.
5. The earth's surface may be modeled as a horizontally inhomogeneous varigated map of Lambertian reflectivity. Several such maps may be treated simultaneously, thus facilitating accurate comparisons amongst the effects of different ground reflectance patterns. Additionally, a given region can be modeled as representative of the surface of the sea using the wave slope model of Cox and Munk (Ref. 2) and Fresnel reflectance.

6. Polarization effects are taken fully into account.

### 1.2.1 Photon Transport and Sampling

CTRANS tracks photons backwards initiating them at the receiver and following them through successive scatterings on their path through the atmosphere. Backward tracking has been adopted for a number of reasons. It permits the efficient and direct simulation of receivers with finite fields of view and/or finite extent. A forward tracking scheme would require the distribution of initial photons over a wide area when horizontal inhomogeneities are present and this would introduce large variances in the results. By initiating photons at the receiver, this source of variance is largely avoided.

To understand backward tracking, consider first a single scattering event. If  $\underline{I}_0$  is the Stokes vector of incident unscattered light,  $\underline{S}$  is the scattering phase matrix and  $\underline{R}$  is a rotation matrix which serves to rotate the plane of reference of the Stokes vector into the scattering plane, the Stokes vector after scattering  $\underline{I}_f$  is given by

$$\underline{I}_f = \underline{R}_r \underline{S} \underline{R} \underline{I}_0$$

where  $\underline{R}_r$  rotates the final Stokes vector into the reference plane of the receiver. After two scatterings, the final Stokes vector will be

$$\underline{I}_f = \underline{R}_r \underline{S}_2 \underline{R}_r \underline{S}_1 \underline{R}_1 \underline{I}_0$$

Cast in this way, it is apparent that what is important is the product matrix which is built from the scattering matrices appropriate to the string of scatterings suffered by the photon.

This product can be built up either from the left or from the right with the same result; i.e., we may equally well follow the photon's history forward or backwards if we accumulate scatterings properly into the product [which we call the cumulative scattering matrix].

There is a further advantage in tracking backwards: contributions from several solar directions may be accumulated from a single track. For example, if the photon is tracked backwards from the receiver, only the last rotation and scattering contain any reference to solar direction. Replacing one sun by another means changing only these two matrices. For each solar direction, at most, two  $4 \times 4$  matrix multiplications must be performed.

Photons are initialized at the receiver; which may be general in the following ways: it may have finite or infinitesimal field of view; it may be oriented pointing toward any zenith angle with any azimuthal angle; it may be at any altitude and have any specified x-y coordinate. On the other hand, for flux calculations the receiver aperture may be finite. This is accomplished by letting the receiver be an entire cloud face (any face of any cloud, pointing into or out of the cloud).

First, initial photon coordinates are created. If the receiver is a cloud face, initial photon coordinates are chosen from a uniform distribution over the cloud face. The photon direction is then determined using: 1) uniform distribution over solid angle for a cloud-face receiver, or 2) uniform distribution over the field of view of an infinitesimal receiver, or 3) in a specified direction if the field of view is infinitesimal. For each type of distribution, the appropriate weight is computed (to be multiplied into the sampled values upon sampling).

The distance to be traversed to a scattering is computed on the basis of optical distance to be traversed: if  $p$  is a uniformly distributed random number, the optical distance to be traversed is given by

$$\tau = -\ln p \quad (1.2.1)$$

Through reference to a table containing the optical thickness of each layer of the ambient atmosphere and taking into account the added optical density in the interior of clouds, the optical distance traversed and physical distance traversed are incremented until an optical distance  $\tau$  has been reached. If, before this has occurred, the photon exits the atmosphere, the photon is terminated.

Having located the position of a scattering, the scatterer type is chosen on the basis of the relative contribution of each scattering species at that point to the local optical density. Here, a cumulative distribution function, which has been tabulated for each layer of the ambient atmosphere, is used in conjunction with any additional optical density due to the presence of a cloud. Photons are not explicitly absorbed. Instead, a weight is accumulated which at any point along the path reflects the probability that the photon has not been absorbed.

After having determined the scatterer type, the probability that the photon could have come from each sun is sampled. If  $\underline{\underline{S}}_I$  is the cumulative scattering matrix at the point of sampling, the sampled Stokes vector will be

$$\underline{\underline{I}}_s = \underline{\underline{S}}_I \underline{\underline{R}}_j \underline{\underline{S}}_j \underline{\underline{I}}_o e^{-\tau_j w} \quad (1.2.2)$$

where  $\underline{\underline{R}}_j$  is a rotation matrix appropriate to a scattering into the  $j^{\text{th}}$  solar direction;  $\underline{\underline{S}}_j$  is a scattering matrix (a Mueller matrix if the scattered is an atmospheric constituent);  $\underline{\underline{I}}_o$  is

the incident Stokes vector in the I, Q, U, V representation;  $t_j$  is the total optical distance along the path connecting the scattering point and sun<sub>j</sub>; w is a weight reflecting the probability that the photon has not been absorbed (including ground absorption for Lambertian regions encountered). There will be a different value for w for each Lambertian albedo map. Note that the above form assumes that  $I_0$  represents initially unpolarized light. If the incident light from the sun were polarized, an additional rotation would be necessary.  $R_j$  has the form

$$R_j = \begin{pmatrix} 1 & 0 & 0 & 0 \\ 0 & \cos 2X & \sin 2X & 0 \\ 0 & -\sin 2X & \cos 2X & 0 \\ 0 & 0 & 0 & 1 \end{pmatrix} \quad (1.2.3)$$

where X is the rotation angle between the normal to the previous scattering plane (or the reference direction in the case of first scatterings) and the normal to the scattering plane for a scattering into the  $j^{\text{th}}$  solar direction.  $S_j$  has the general form

$$S_j = \frac{1}{4\pi} \begin{pmatrix} S_{11} & S_{12} & 0 & 0 \\ S_{12} & S_{22} & 0 & 0 \\ 0 & 0 & S_{33} & S_{34} \\ 0 & 0 & -S_{34} & S_{44} \end{pmatrix} \quad (1.2.4)$$

where  $S_{\ell,m}$  depends upon scattering angle. For Rayleigh scattering,  $S_{11} = S_{22} = \frac{3}{4} (1 + \cos^2 \beta_j)$

$$S_{12} = \frac{3}{4} (\cos^2 \beta_j - 1)$$

$$S_{33} = S_{44} = \frac{3}{2} \cos \beta_j$$

$$S_{34} = 0$$

where  $\beta_j$  is the scattering angle for a scattering into the  $j^{\text{th}}$  solar direction. For Lambertian scattering at the ground  $S_{11} = 4 \cos \theta_j$ , where  $\theta_j$  is the zenith angle of the  $j^{\text{th}}$  sun and all other matrix elements are zero. Lambertian reflection thus is perfectly depolarizing.

Mie scattering and Fresnel scattering both have matrices with the form of Eq. (1.2.4). Mie elements are stored in tabular form and values for particular scattering angles are obtained by interpolation. The Fresnel matrix elements are given in the discussion of ground reflectance.

The next step after sampling is to accumulate a "real" scattering. Knowing the scatterer type, an appropriate scattering angle is found. If the scattering angle were chosen from a uniform distribution, and if the scattering matrix appropriate to the medium exhibited sharp peaks, then most photons would rapidly lose weight and large numbers of photon tracks would be necessary in order to achieve a reasonably small variance. To resolve this difficulty, we use the concept of importance sampling. We choose the scattering direction from a biased distribution designed to maximize the resultant contribution. The bias thus introduced is then removed by applying a weight. More concretely, we wish to fold in a scattering matrix

$$S = \begin{pmatrix} S_{11} & S_{12} & 0 & 0 \\ S_{12} & S_{22} & 0 & 0 \\ 0 & 0 & S_{33} & S_{34} \\ 0 & 0 & -S_{34} & S_{44} \end{pmatrix} \frac{d\omega}{4\pi}$$

$$\frac{1}{f(\beta)} \begin{pmatrix} S_{11} & S_{12} & 0 & 0 \\ S_{12} & S_{22} & 0 & 0 \\ 0 & 0 & S_{33} & S_{34} \\ 0 & 0 & -S_{34} & S_{44} \end{pmatrix} \frac{f(\beta) d\omega}{4\pi} \quad (1.2.5)$$

Instead of choosing the scattering angle from a probability distribution corresponding to the probability density  $\frac{d\omega}{4\pi}$  (uniform), we use the distribution corresponding to the probability density  $\frac{f(\beta) d\omega}{4\pi}$ . The weight of the photon following the scattering can thus be maximized by choosing  $f(\beta) = S_{11}$  times a constant chosen so that the first matrix element is always unity. A real scattering is accumulated by multiplying into the cumulative scattering matrix first a rotation, and then the scattering matrix.

The process is repeated until either a designated maximum number of scatterings have been suffered, the photon leaves the atmosphere or its weight drops below the assigned threshold (due, for example, to atmospheric absorption).

### 1.2.2 Ground Scattering

CTTRANS has the capability to model reflections from spatially inhomogeneous ground. In the present version of the code, the physical mechanism of reflection may be modeled as either Lambertian reflection or as Fresnel reflection from a rough surface and these modes may be intermixed in a patchwork fashion.

Reflectance type is basically controlled by a reflectance type map which dictates the reflectance character from point to point across the infinite ground plane. When a photon strikes the ground, its impact coordinates are computed and then used to decide whether the point of impact was within a Lambertian or a rough Fresnel region.

Since Lambertian reflection is not physically dependent upon the direction of incidence or reflection but only upon a scalar Lambertian albedo, CTRANS can model simultaneously the effect of several values (up to 220) of the albedo for each of the Lambertian regions. This is accomplished in the following way: A vector of scalar weights is maintained; one for each albedo map. When a Lambertian scattering occurs, the albedo at the point of impact is determined for each of the albedo maps and this is multiplied into the corresponding albedo weight to obtain a new weight for subsequent use. Upon sampling, each current albedo weight is folded into the sampled Stokes vector to obtain samples corresponding to each of the allowed albedo maps. If the impact point lies within a Fresnel region, however, the vector of albedo weights is left unchanged (since it represents the cumulative effects of only the Lambertian regions).



Symbolically, the entire reflection process is as follows: given an old cumulative scattering matrix  $S_0$ , the new one,  $S_N$ , is computed as:

$$S_N = S_0 R s$$

where  $R$  is a rotation matrix and  $s$  depends upon the reflectance type at the impact point. Specific examples are

$$\text{Lambertian} \quad s = \begin{pmatrix} \cos \theta & 0 & 0 & 0 \\ 0 & 0 & 0 & 0 \\ 0 & 0 & 0 & 0 \\ 0 & 0 & 0 & 0 \end{pmatrix}$$

and

$$\text{Fresnel} \quad s = \begin{pmatrix} S_{11} & S_{12} & 0 & 0 \\ S_{12} & S_{11} & 0 & 0 \\ 0 & 0 & S_{33} & 0 \\ 0 & 0 & 0 & S_{33} \end{pmatrix}$$

where  $S_{ij}$  represent Fresnel matrix elements:

$$S_{11} = (R_{11}^2 + R_1^2)/2$$

$$S_{12} = (R_{11}^2 - R_1^2)/2$$

$$S_{33} = R_{11} R_1$$

$$R_{11} = \frac{n \cos \chi_i - \cos \chi_t}{n \cos \chi_i + \cos \chi_t}$$

$$R_1 = \frac{\cos \chi_i - n \cos \chi_t}{\cos \chi_i + n \cos \chi_t}$$

$n$  = relative index of refraction of the surface

$\chi_i$  = angle of incidence

$\chi_t$  = angle of refraction, computed for  $\chi_i$  through Snell's law at the interface:  $n \sin \chi_t = \sin \chi_i$ .

The vector of scalar weights is renewed according to

$$A_i^{\text{new}} = A_i^{\text{old}} \times a_i(J; X, Y)$$

$X, Y$  = coordinates of impact point

$J=0$  = region is Lambertian and the values of  $a_i$  ( $i=1, 220$ ) are determined from the Lambertian albedo maps according to the coordinates  $(X, Y)$

$J=1$  = region is Fresnel  $a_i = 1$  ( $i=1, 220$ ).

For rough Fresnel regions, the roughness is characterized as a distribution of randomly oriented sloping plane facets (ref. 2). The probability density for the distribution of slopes was chosen to have two-dimensional Gaussian form.

$p(z_x, z_y) \delta z_x \delta z_y$  is the fraction of a small horizontal unit area of surface for which the  $x, y$  components of the slope are within the limits  $z_x \pm \frac{1}{2} \delta z_x$  and  $z_y \pm \frac{1}{2} \delta z_y$ . We specify  $p(z_x, z_y)$  as:

$$p(z_x, z_y) = (\pi\sigma^2)^{-1} \exp [-(z_x^2 + z_y^2)/\sigma^2]$$

The variance,  $\sigma^2$  is specified either by three parameters W0, W1, W; or as a set value specified on input. When specified through parameters,  $\sigma^2$  is given as

$$\sigma^2 = W0 + W1 \times W$$

W represents wind speed (m/sec) in a model for the surface of the sea<sup>1)</sup> and W0, W1 have either their default values (W0 = .0015, W1 =  $2.54 \times 10^{-3}$ ) or values specified by card input. In the present code, all rough Fresnel regions share the same parametric values.

The above form for  $p(z_x, z_y)$  represents that applicable for a photon incident from the vertical. For photons incident from some other direction, the distribution must be modified. Let the photon's direction be given by unit vector  $\hat{k}$ , the direction of the normal to a facet be  $\hat{n}$ , and the vertical direction be  $\hat{z}$ . The probability of encounter will then be given by

$$\frac{\hat{k} \cdot \hat{n}}{(\hat{n} \cdot \hat{z})(\hat{k} \cdot \hat{z})} p(\hat{n})$$

Having determined a slope at the photon impact point, the angle of incidence and, thence, the Fresnel matrix elements can be determined. If  $\hat{k}$  and  $\hat{k}'$  are the directions of propagation of the incident and reflected photons, their relation to  $\hat{n}$  is

$$\frac{\hat{k}' - \hat{k}}{|\hat{k}' - \hat{k}|} = \hat{n}$$

When sampling the contributions of unscattered photons from the Sun at a Fresnel scattering point, the direction of reflection is given by the solar direction and one merely evaluates the probability of having encountered a slope having the proper orientation. Note that in the present model the location of the Sun is given by a Dirac delta function (incoming plane waves) rather than being spread over a small angular region. The implied integration over the solar direction (or, equivalently, the change of variables within the delta function specifying the solar direction) introduces an additional factor of

$$.25 (\hat{n} \cdot \hat{z})^{-3} (\hat{k} \cdot \hat{n})^{-1}$$

### 1.3 MODEL CONDITIONS

An atmosphere was chosen so as to represent clear normal conditions characteristic of the rural midwest. This choice was dictated by the task of the Thematic Mapper to classify agricultural regions. Because ozone is only weakly optically active over the wavelengths included in the bands sensed by the Thematic Mapper, it was omitted from the simulation. The particle number density for the aerosol and Rayleigh atmospheric components are shown in figure 1.2. The aerosol is represented by a "Haze C" polydispersion with a particle size distribution give by

$$\begin{aligned} n(d) &= 0 & d \leq d_0 \\ n(d) &= c & d_0 < d \leq d_1 \\ n(d) &= c d^{-4} & d_1 \leq d \leq d_{\max} \end{aligned} \quad (1.3.1)$$

Normalization provides that  $c$  is given by

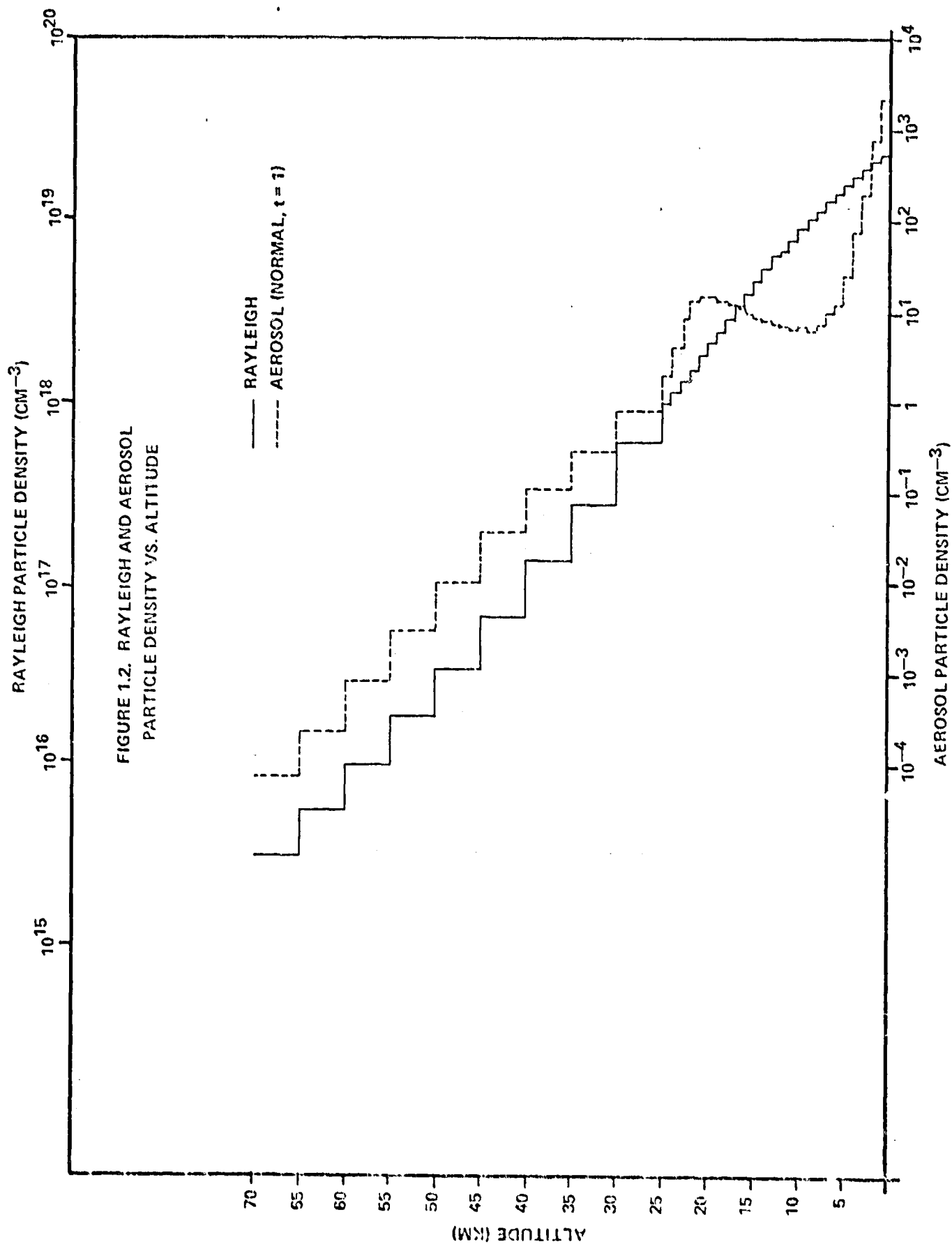
$$c = N \frac{3 d_1^4}{4 d_1^{-3} d_0} \quad (1.3.2)$$

where  $N$  is the total number of particles per cubic centimeter and the values chosen for  $d_0$  and  $d_1$  were

$$d_0 = 0.06 \mu\text{m}. \quad (d_{\max} = 16.16 \mu\text{m}.)$$

$$d_1 = 0.2 \mu\text{m}.$$

The aerosol particle index of refraction was chosen to be  $m=1.50+0.0i$ , i.e., the aerosol was non-absorbing.



In the calculations to be reported here, we used our standard atmosphere modified to span the turbidity levels to be expected in the vicinity of agricultural regions. This was accomplished by using our standard model for the Rayleigh (molecular scatterers) portion of the atmosphere together with aerosol components obtained from the standard model by scaling the aerosol densities by a numerical factor which we call the turbidity,  $t$ . The models considered here include  $t=0, 1, 3$ . The vertical optical thicknesses corresponding to the Rayleigh and aerosol components as a function of wavelength are given in Table 1.1.

The receiver or detector was placed at an altitude of 704 km pointed towards the nadir. No attempt has yet been made to model the cross-track scan of the receiver since this is to be expected to contribute only weakly to changes in viewed radiance across a scene. Sources of variance in detected radiance while scanning include bidirectional reflectance effects, small changes in attenuation due to variation in the slant path range between the IFOV and the detector, and small changes in the pure atmospheric path radiance (due to changes in the slant path range and to changes associated with the angular dependence of the scattering phase functions for primary scattering).

The field of view of the receiver was modeled as finite in most of the calculations. Our initial studies assumed a circular field of view with an apex semi-angle of 42.6 microradians resulting in a ground footprint which was circular with a 60 m diameter. This was changed in our later calculations to a square field of view with angular spread of 42.6 microradians (30 m square footprint) in order to conform more exactly with the specifications of the Thematic Mapper. In addition, some calculations were performed with an infinitesimal field of view. The response of the receiver was taken to be uniform (flat) over the field of view for the square field of view.

$\lambda$ ( $\mu\text{m}$ )	$\tau_{\text{Rayleigh}}$	$\tau_{\text{Aerosol}}$ <span style="float: right;">—————→ optical thickness</span>		
		$t=0$	$t=1$	$t=3$ <span style="float: right;">—————→ turbidity</span>
.47	.18934	0.0	.24359	.73076
.55	.10037	0.0	.21237	.63711
1.65	.001189	0.0	.07332	.21997

Table 1.1  
Rayleigh and Aerosol Vertical Optical Thickness  
for Modeled Wavelengths and Turbidities



Ground reflectances were modeled as Lambertian throughout the initial study even though the code CTRANS has the capacity to treat other types of reflectance. The reflectivity of the ground was modeled as horizontally inhomogeneous, consisting of various one and two dimensional patterns specifically chosen to aid in the analysis of the impact of ground and atmospheric scattering on observed radiances. These patterns included models of the boundary between two semi-infinite planes with differing albedos, albedo patterns varying sinusoidally (used to compute the atmospheric modulation transfer function), isolated square regions of varying size situated on an infinite, uniform background, pairs of adjoining square regions, and, checkerboard regions, and infinite uniform ground planes.

The effects of clouds and horizontal gradients in the atmospheric turbidity have not yet been studied. The present code, CTRANS is, however, capable of treating these additional complications.

The solar zenith angles for which most of our calculations were performed were:  $40^\circ$ ,  $55^\circ$ ,  $70^\circ$  and are representative of the range expected to be encountered by the Thematic Mapper.

Primarily for reasons of economy, we have not modeled all of the wavelength bands of the Thematic mapper. This study treats explicitly three wavelengths spanning the visible and near infrared:  $.45\mu\text{m}$ ,  $.55\mu\text{m}$ , and  $1.65\mu\text{m}$ . It should be noted that we have modeled the transport of light of specific wavelengths and have made no attempt to integrate over the bands. Additionally, we should point out that the normalization of the solar flux incident upon the top of the atmosphere was taken, for all wavelengths, to be unity. Thus, actual expected intensities at the receiver may be obtained by scaling the modeled intensity by the value of the extraterrestrial solar flux for the appropriate wavelength.

## 1.4 THEMATIC MAPPER SPECIFICATIONS

For information purposes, we include here a brief description of the specifications of the Thematic Mapper (ref.3) Spectral Bands:

Band No.	Band (micrometers)	Radiometric (NE $\rho$ )	(NETD at 300k)
1	0.45-0.52	0.008	
2	0.52-0.60	0.005	
3	0.63-0.69	0.005	
4	0.76-0.90	0.005	
5	1.55-1.75	0.01	
6	10.40-12.50		0.5K

Where NE $\rho$  is the noise equivalent reflectance and NETD is the noise equivalent temperature difference. The spectral region and radiometric performance of a seventh proposed band had not yet been specified at the inception of this study.

### ORBIT

The orbit is to be sun synchronous and circular with an orbit inclination of 98.2 degrees. The design altitude is 705 km and the north to south equatorial crossing time is 0930 hours local time.

### SPATIAL COVERAGE

The cross-track and along-track IFOV will be approximately 42.6 microradians for bands 1-5 corresponding to a 30 m field of view. The IFOV boundary is at the 50% response level. Cross track scanning will be approximately  $\pm 7.5^\circ$ , or about 185 km coverage.

## SQUARE WAVE RESPONSE

The square wave modulation response (defined as the ratio of the peak-to-peak signal modulation produced by scanning a series of high contrast square wave targets to the signal modulation produced by scanning a series of square wave targets with half cycles of 500 m) is given below:

Band 1-5, and 7

ground target size (m)	500	60	45	30	15
modulation response	1	0.85	0.70	0.35	information only

## STEP RESPONSE

When scanning a step function (edge) of input radiance final steady state response (within 0.5%) it is to be achieved by the fourth receiver field of view dwell time after the start of the response. Overshoot/undershoot is to be limited to 1% of the step size. Rise time will be less than 1.6 receiver field of view dwell times (2% of steady state to 2% of steady state).

## DIGITIZATION

Eight bit digitiation will be used (up to 256 grey levels).

## SECTION 2.0

### MODEL OBSERVATIONS OF GROUND PATTERNS

Since we are primarily interested in the results of image degradation as induced by the interactions at atmospheric and ground scattering, a very natural approach is to choose certain definite and particularly useful ground albedo patterns for use as investigative probes. Since CTRANS can treat a number of Lambertian ground patterns simultaneously, it can model a scan across a boundary simply by modeling a series of identical patterns with successive incremental displacements. When the same set of photons is used to compute results for a number of albedo patterns, there is an important additional benefit: the variance in the computed intensities from one pattern to another is greatly reduced (even though the variance in the absolute values of the intensities are larger). An example of this is found in scans across the boundary of two semi-infinite planes: there will be relatively little error from point to point along the scan but there may be larger error (normal statistical variation) in the overall scaling which would amount to a shift of the entire curve up or down. This should be remembered especially when evaluating comparisons between statistically independent runs [results for each turbidity are derived from separate runs].

The results to be presented here are derived from three patterns: a semi-infinite plane, a square field on a uniform background, and a checkerboard pattern. The boundary of the semi-infinite plane is scanned, as is a boundary of the checkerboard. The isolated field is allowed to expand in order to investigate, specifically, field size effects. With each study, we also have included albedo patterns corresponding to infinite uniform planes. This provides asymptotic values, a means for intercomparison and calibration constants required to transform the sensed intensities to effective albedoes as discussed in Section 3.

Some of our earlier calculations were performed using a circular IFOV with a 30 m radius, while later results model the IFOV of the Thematic Mapper more closely, i.e., as a 30-m square.

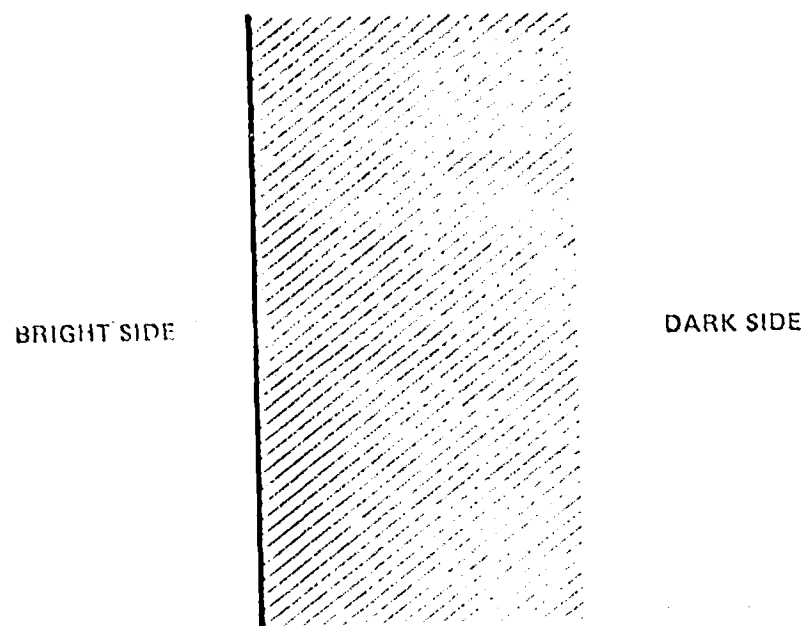
## 2.1 AN ALBEDO BOUNDARY: SEMI-INFINITE PLANES

In order to study effects which are induced merely by the presence of boundaries in the albedo pattern of the earth, it is extremely useful to analyze the simplest possible case: the boundary between two semi-infinite ground planes of differing Lambertian albedo (illustrated in figure 2.1). In order to simulate a scan across such a boundary, CTRANS models the observed radiance for a number of independent ground albedo maps differing by the location of the boundary with respect to the instantaneous field of view (IFOV).

In our initial computation, illustrated in figure 2.2, we compare the intensities sensed while traversing boundaries with three differing contrasts. The albedo pairs of the semi-infinite planes were (0.6, 0.0), (0.5, 0.1), (0.4, 0.2). The atmosphere in this case was our standard atmosphere and the wavelength was 0.55 $\mu$ m. Several significant effects are to be noted. Even at distances as large as 2 km from the boundary, the sensed intensity differs from its asymptotic value. As the IFOV approaches the boundary, the effects of the boundary begins to strongly affect the intensities at a distance dependent upon the contrast of the boundary. For high contrast the inner region of strong interaction may be as large as one kilometer. This is, to some extent, dependent upon the size and shape of the IFOV, which in this initial computation was taken to be circular with a diameter of 60 m at the ground, i.e., larger than the IFOV for the Thematic Mapper.

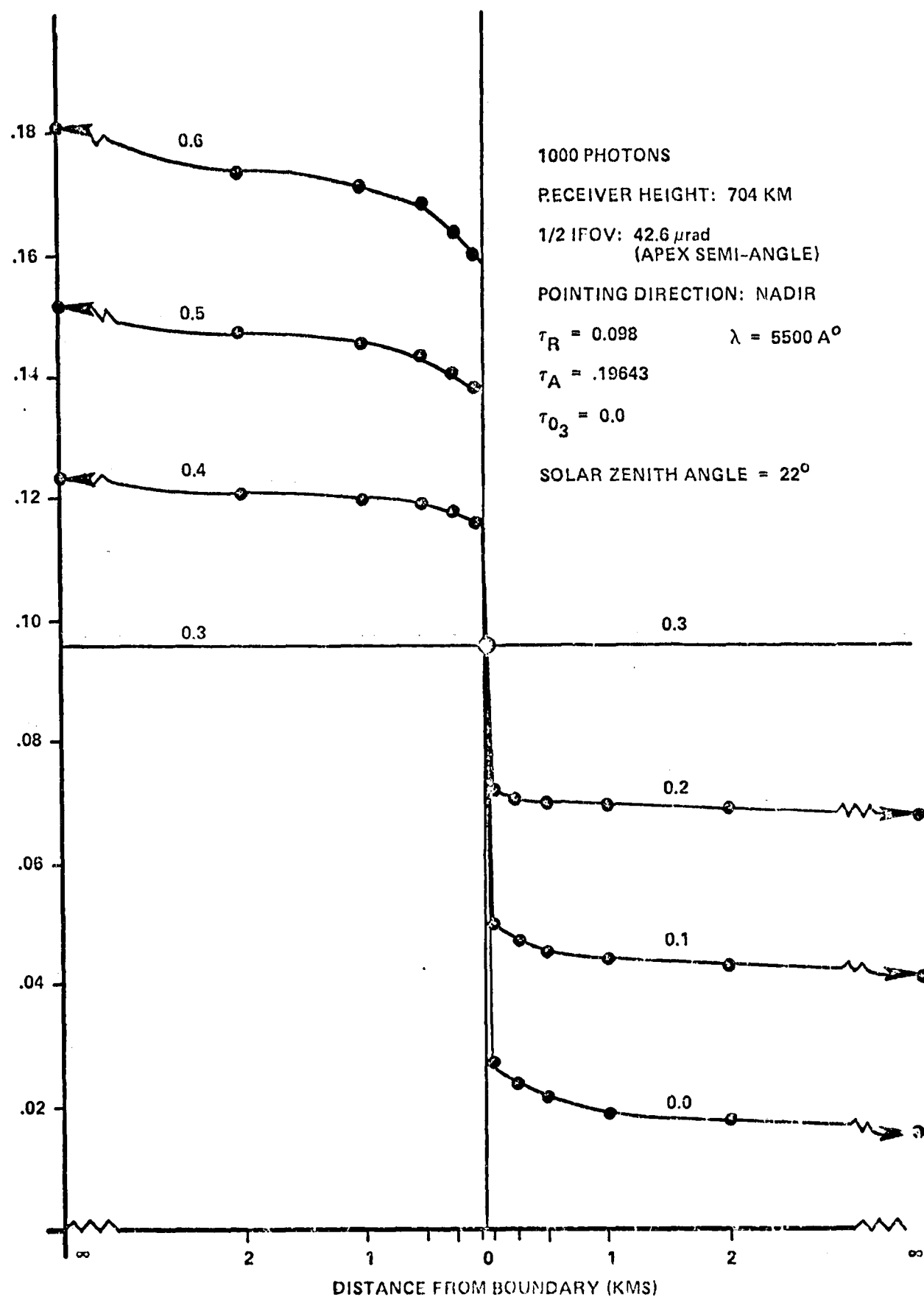
The boundary effects are due to the scattering properties of the atmosphere. These scattering properties will be functions of aerosol content and distribution as well as being wavelength dependent. The strongest part of the wavelength dependence arises from the fact that the Rayleigh (molecular) scattering cross section is proportional to  $\lambda^{-4}$

FIGURE 2.1.  
SCHEMATIC ILLUSTRATION OF REFLECTANCE GEOMETRY 1:  
HALF PLANES



INTENSITY  
(ster<sup>-1</sup>)

FIGURE 2.2.  
ALBEDO BOUNDARY EFFECTS





The aerosol scattering cross section is also wavelength dependent but varies much more slowly with changes in wavelength than the Rayleigh cross section. In order to examine these effects we repeated the semi-infinite plane calculation for three atmospheres differing in aerosol content and computed results for three wavelengths: 0.47, 0.55, and 1.65  $\mu$ . Additionally, the range of distances from the boundary was extended to 10.0 kms. and the size and shape of the IFOV was modeled to match that of the Thematic Mapper i.e., as a 30 m square on the ground. The three aerosol distributions are given in terms of the ratio of the aerosol density at a given altitude to the aerosol density at the same altitude for the normal atmosphere. This ratio is termed the turbidity. Taking turbidities of 0, 1, and 3, we span the expected aerosol content range for agricultural regions.

A summary of the results of these computations is presented in figures 2.3 through 2.7. Here, the distance of the IFOV from the boundary is presented on a logarithmic scale. The top three curves correspond to the bright side of the boundary while the bottom curves describe the behavior on the dark side. The dashed portions of the curves are the results of interpolations between computed points on either side of the boundary. Comparison of figures 2.3, 2.4 and 2.5 illustrates the effect of changing the wavelength with other parameters held constant. Figure 2.3 includes scales indicating the percent error from the intensity values corresponding to infinite uniform planes. In figure 2.4, we compare results computed for solar zenith angles of  $40^\circ$  and  $70^\circ$ . It is seen that the major effect of increasing the solar zenith angle is attenuation which shrinks the curves and reduces the contrast observed while scanning across the boundary. Figures 2.6 and 2.7 indicate the impact of reduced contrast at the boundary. One effect of decreased contrast is to shift the curves relative to one another making the bright side intensity

FIGURE 2.3.

INTENSITY VS DISTANCE FROM BOUNDARY FOR STEP FUNCTION ALBEDO PATTERN (0., .6)

WAVELENGTH =  $0.47 \mu\text{m}$   
 RECEIVER ALTITUDE = 704 km  
 RECEIVER FOOTPRINT = .03 km square  
 SOLAR ZENITH ANGLE =  $40^\circ$

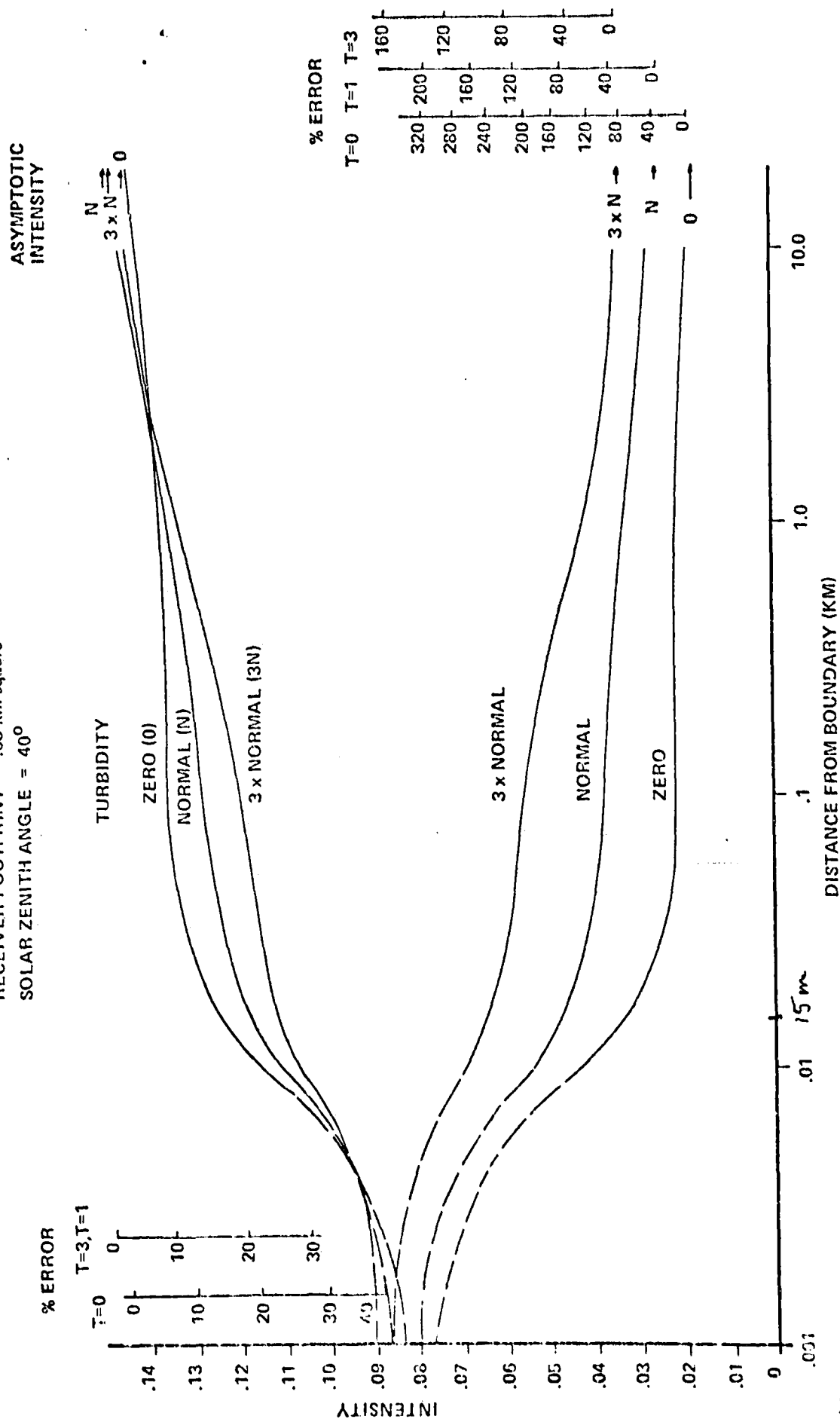


FIGURE 2.4.

INTENSITY VS DISTANCE FROM BOUNDARY FOR STEP FUNCTION ALBEDO PATTERN (0., .6)

WAVELENGTH =  $0.55 \mu\text{m}$

RECEIVER ALTITUDE = 704 Km

RECEIVER FOOTPRINT = .03 Km SQUARE

— SOLAR ZENITH ANGLE =  $40^\circ$

- - - SOLAR ZENITH ANGLE =  $70^\circ$

ASYMPTOTIC  
INTENSITY

TURBIDITY  
( $40^\circ$ )  
ZERO

NORMAL

3 x NORMAL

3 x N  
N  
0

TURBIDITY  
( $70^\circ$ )  
ZERO

NORMAL

3 x NORMAL

0  
3 x N  
N

3 x NORMAL

NORMAL

ZERO

3 x N

N

0

DISTANCE FROM BOUNDARY (KM)

INTENSITY

**FIGURE 2.5.**  
**INTENSITY VS DISTANCE FROM BOUNDARY FOR STEP FUNCTION ALBEDO PATTERN = (0., .6)**

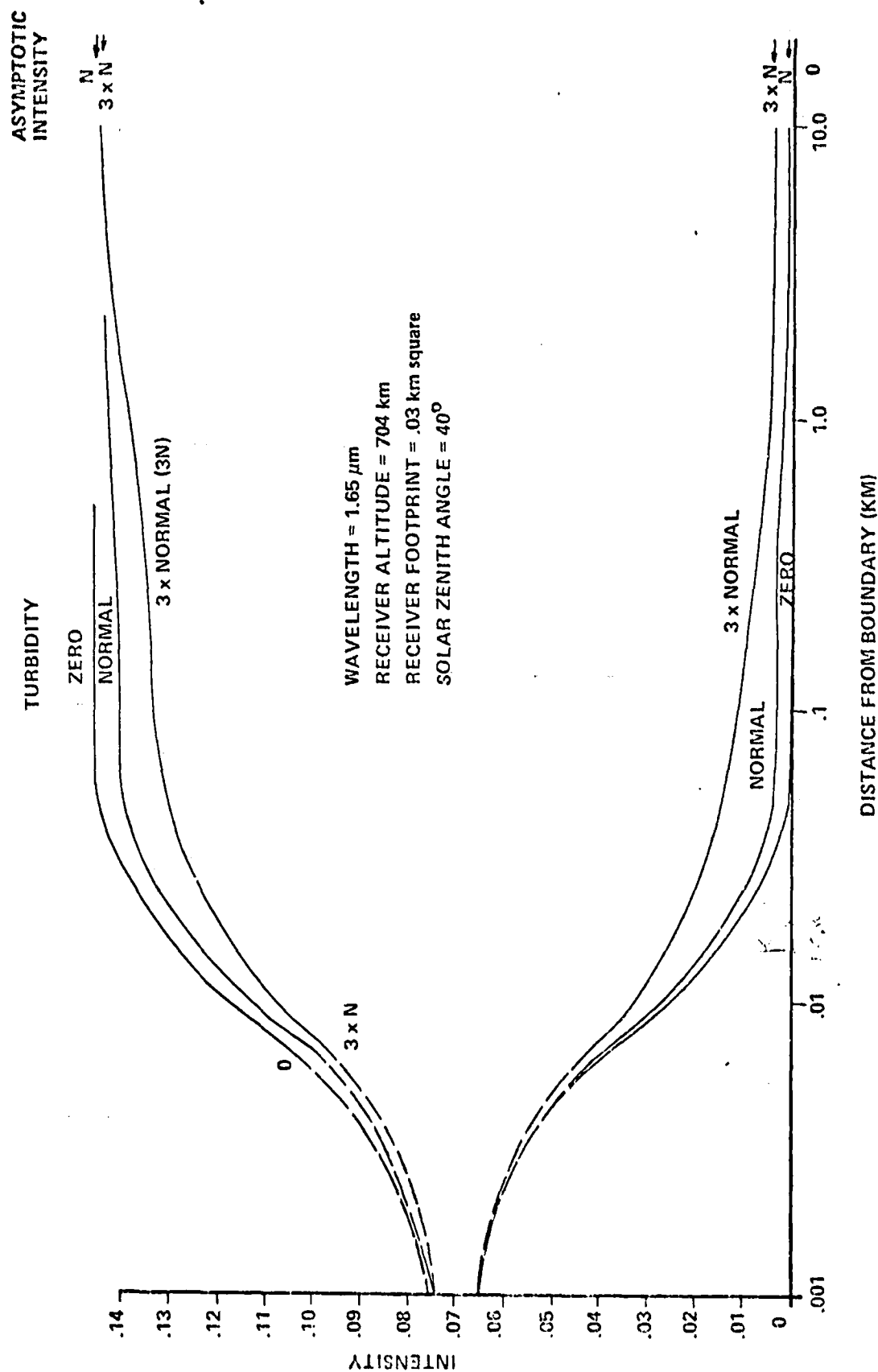


FIGURE 2.6.

INTENSITY VS DISTANCE FROM BOUNDARY FOR STEP FUNCTION ALBEDO PATTERN (.1, .5)

WAVELENGTH =  $0.55 \mu\text{m}$   
 RECEIVER ALTITUDE = 704 km  
 RECEIVER FOOTPRINT = .03 km square  
 SOLAR ZENITH ANGLE =  $40^\circ$

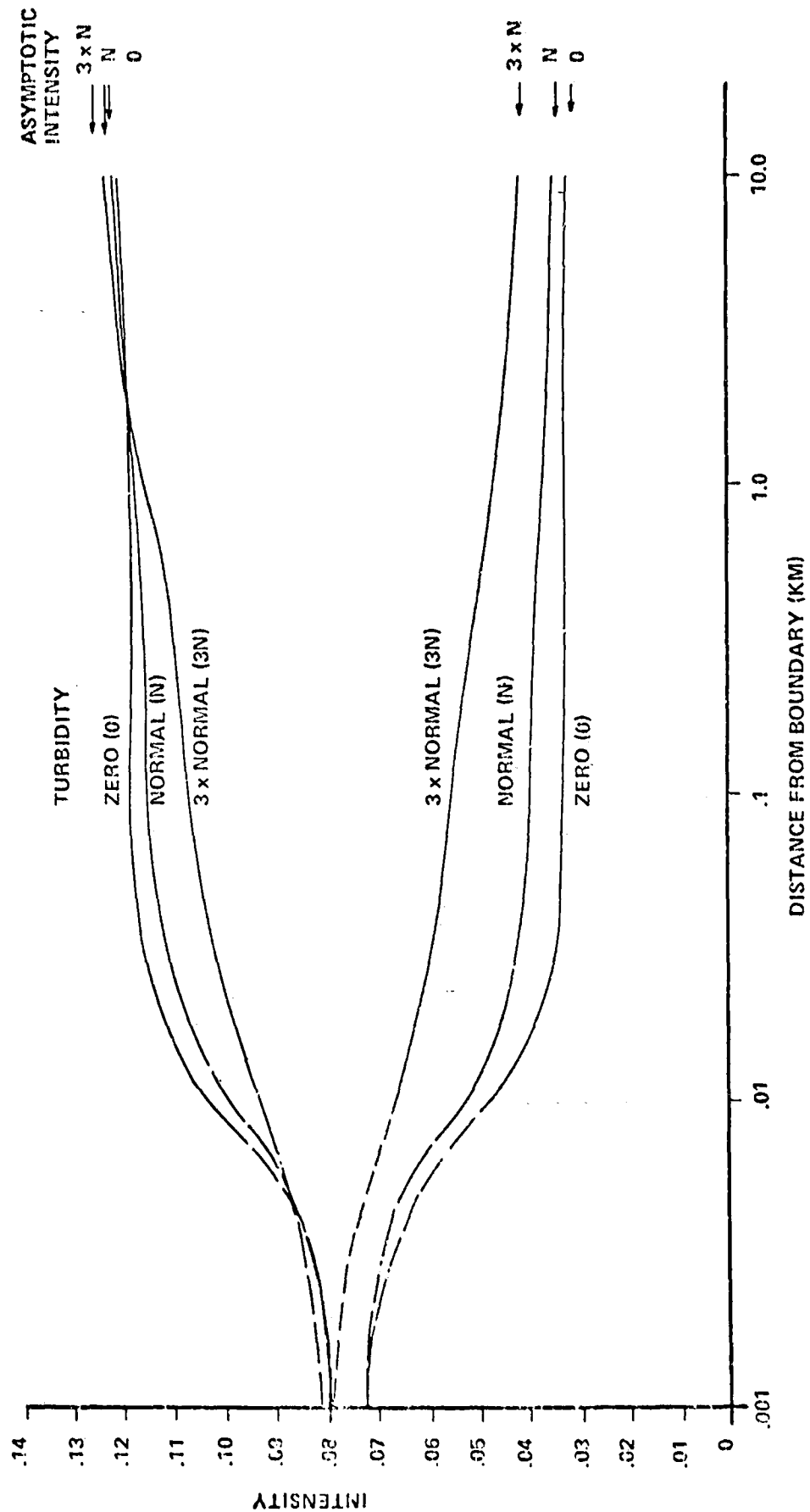
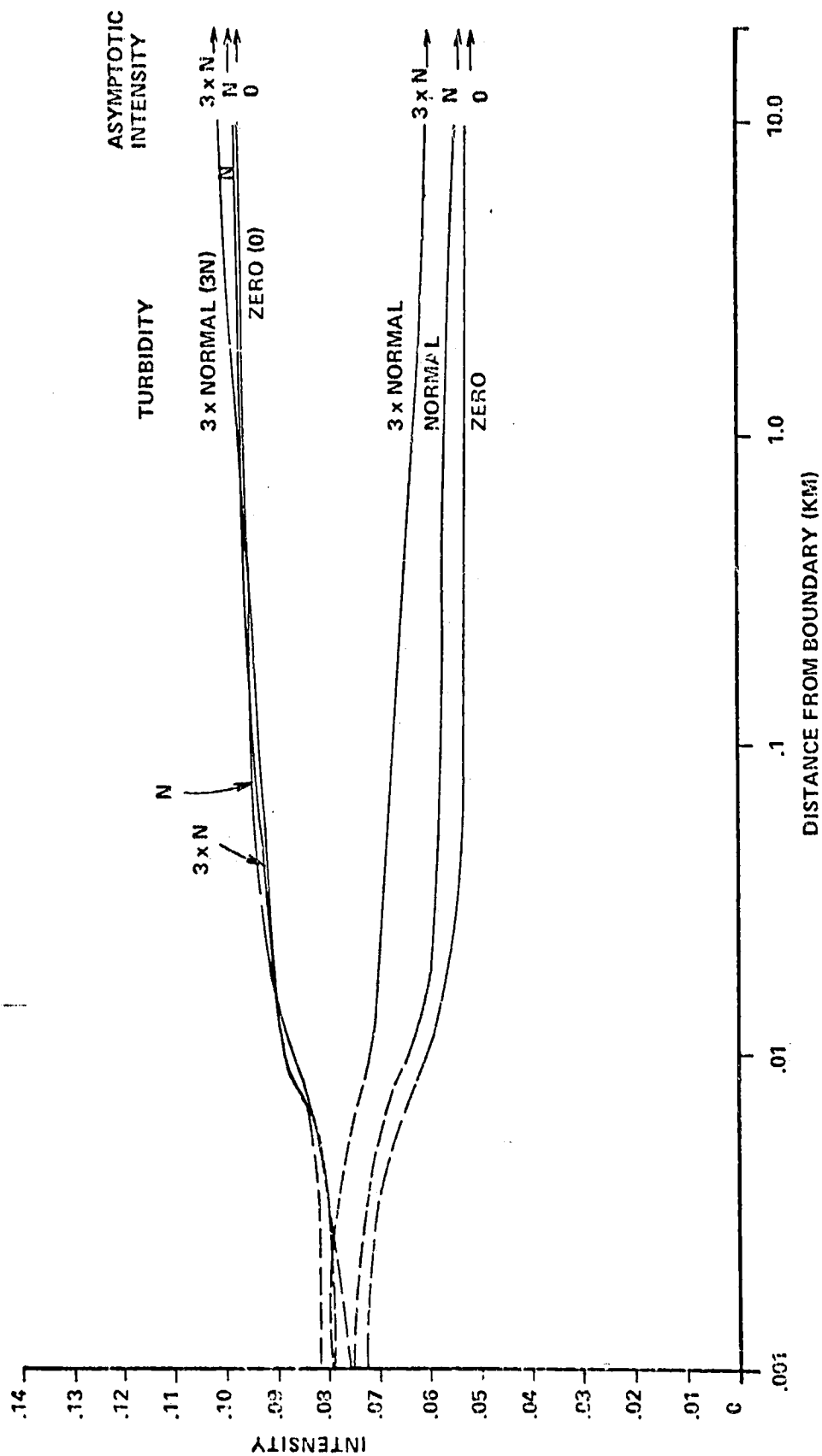


FIGURE 2.7.  
 INTENSITY VS DISTANCE FROM BOUNDARY FOR STEP FUNCTION ALBEDO PATTERN (2, .4)

WAVELENGTH =  $0.55 \mu\text{m}$   
 RECEIVER ALTITUDE = 704 km  
 RECEIVER FOOTPRINT = .03 km square  
 SOLAR ZENITH ANGLE =  $40^\circ$



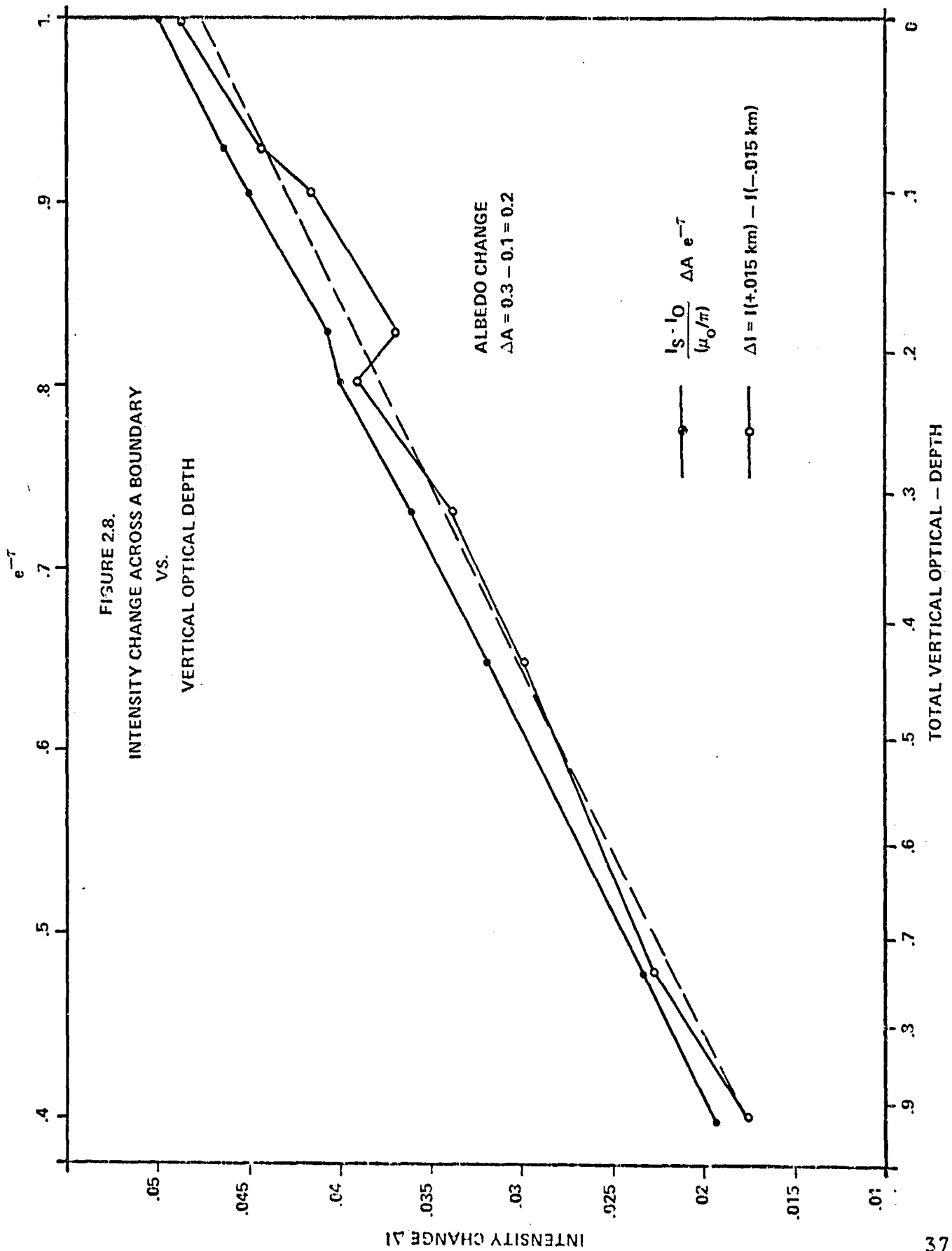
relatively more, independent of atmospheric turbidity than the dark side curves. This is particularly evident in figure 2.7.

As may be seen, at a distance of 10 km, the dark side intensities have very nearly achieved their asymptotic values. For the bright side for shorter wavelengths, higher turbidities and high contrast, the presence of the boundary is still felt to some extent even 10 km distant from it. When the boundary contrast is reduced, however, the asymptotic values are achieved by 10 km.

One important feature of the curves which we shall discuss later is that they are nearly linear in the logarithm of the distance from the boundary over a fairly wide range. This behavior cannot be true close to the boundary and must not be precisely true at great distances from the boundary. Nevertheless, for intermediate distances (on the order of 0.5 to 2.0 km for low contrast) this linear behavior is an important characteristic.

Some further insight may be gained by considering together computations for all wavelengths and turbidities. It is true that the scattering properties of one atmosphere at a given wavelength and turbidity will not be the same as those for an atmosphere with lower turbidity at a shorter wavelength even though the total vertical optical depths may be the same. Nevertheless, some insight may be achieved by examining the boundary effects simply as functions of the total vertical optical depth. Table 2.2 gives the total vertical optical depth for each wavelength and turbidity.

In figure 2.8 we have plotted the change in intensity at the boundary of two semi-infinite planes of albedo  $A=0.3$  and  $A=0.1$  as a function of  $\text{EXP}(-\tau)$  where  $\tau$  is the total vertical optical depth. As may be seen, the behavior is very nearly



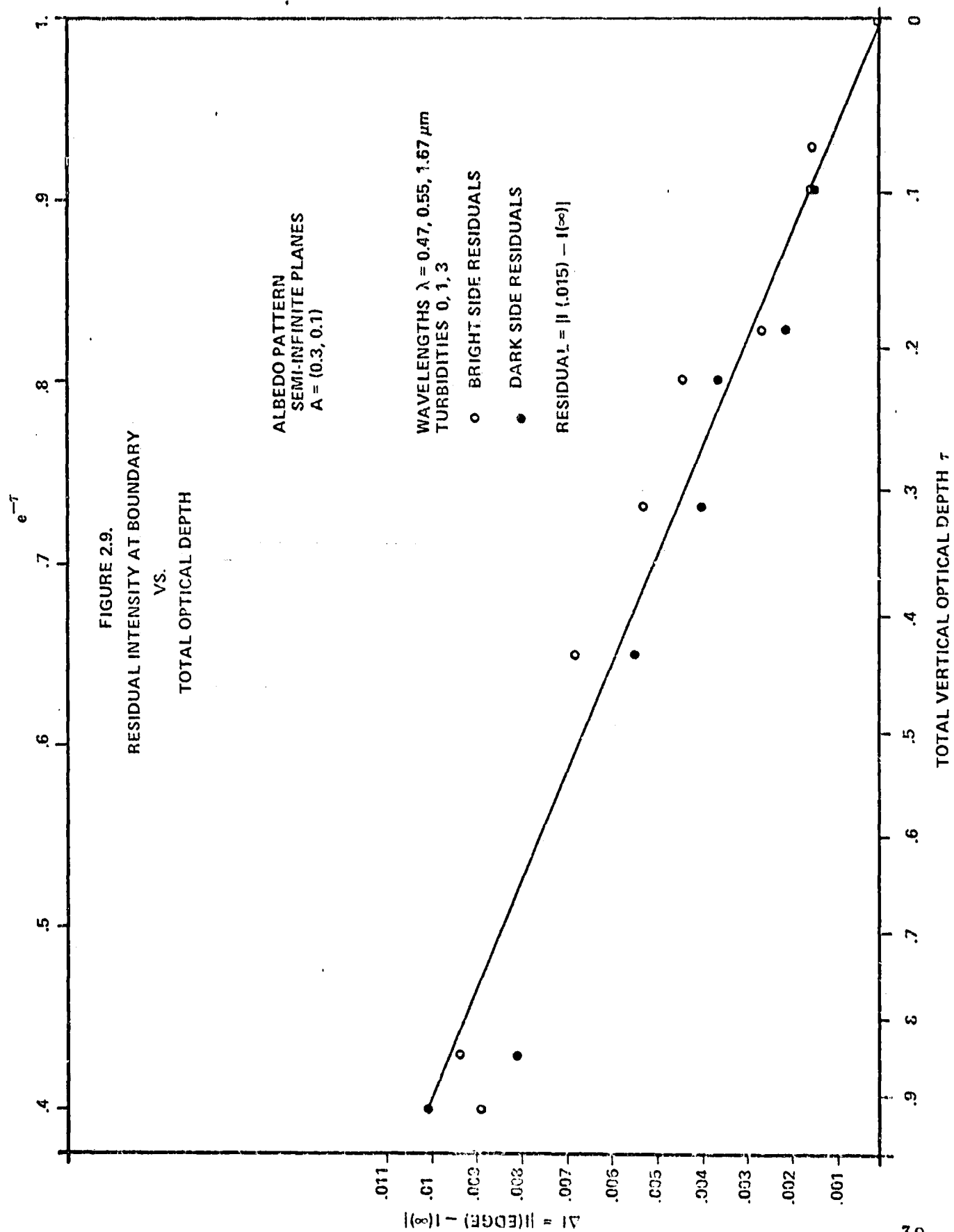


linear. The excursions from linearity are due mainly to the differences between the scattering properties of Rayleigh and Aerosol atmospheres of equal optical depth. The second curve of figure 2.8 is a crude approximation to the effect.  $I_S$  is the extraterrestrial incident intensity ( $I_S = 1$ , here).

$I_0$  is the path radiance, and  $\mu_0$  is the cosine of the solar zenith angle. Also included in the figure is a straight line fit to the  $\Delta I$  curve:  $\Delta I \approx -.0021 + .0495 \text{ EXP}(-\tau)$  (with correlation coefficient  $r^2 = .9853$ ). The fit parameters cannot be regarded as exact since we know that  $I$  must approach zero as  $\tau \rightarrow \infty$ .

Apart from the rapid change of intensity as an albedo boundary is crossed, the chief striking feature of the boundary effect is the difference between the intensity very near to the boundary and its asymptotic value very far away from the boundary. Both effects have a theoretical connection which we will discuss later. We can examine the gross behavior of this residual intensity in the same fashion as for the intensity change across a boundary: we examine it as a function of the total vertical optical depth (or, more precisely, as a function of  $\text{EXP}(-\tau)$ ). Figure 2.9 depicts the behavior of the residual intensity both for the dark and bright sides of the boundary. The linearity of the general trend is accentuated by the straight line fitted to the points by eye. Note that the residual intensity must vanish at  $\tau=0$ .

The simplicity of the gross behavior of the intensity change at a boundary and the residual intensity suggests the possibility that simple semi-empirical methods might be found for correcting observed intensities for atmospherically induced boundary effects.



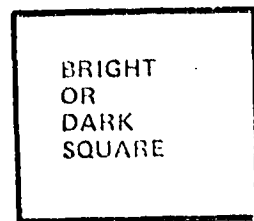
## 2.2 SINGLE SQUARE FIELDS

An estimation of the effects to be expected from two dimensional ground reflectance patterns can be made from a study of the simplest two dimensional pattern: a single square field surrounded by an infinite uniform region of contrasting albedo. This pattern is shown schematically in figure 2.10. Rather than scanning the plane, as was done for the semi-infinite plane pattern, the IFOV is fixed in the center of the field and the size of the field is varied.

Figure 2.11 presents an example of simulation results obtained with a circular IFOV: wavelength,  $\tau=0.55\mu\text{m}$ ; solar zenith angle,  $\theta_0=22^\circ$ ; turbidity=1; IFOV=circular with 30 m radius. The intensity values approached as the field size becomes infinite are shown by the arrows. Here it is made very clear that the finite size of the field may have a large impact on the sensed intensity even when the fields are of quite considerable size (on the order of or greater than 8 km.). The magnitude of the residual from the infinite field size case is diminished when the contrast between the field and its background is reduced. Also notable is the roughly linear behavior of the intensity with field size for fields larger than 2-3 km.

The changes in behavior associated with variable turbidity are illustrated in figures 2.12 and 2.13. For these calculations, the IFOV was 30 m square; the solar zenith angle was  $40^\circ$ ; and, again, the wavelength was  $0.55\mu\text{m}$ . It is seen that changes in turbidity can greatly modify the intensity sensed from the centers of small fields. It is to be noted that the effect is moderated somewhat when the contrast is reduced but is nevertheless still quite large for moderate contrasts as shown in figure 2.13.

FIGURE 2.10.  
SCHEMATIC ILLUSTRATION OF REFLECTANCE GEOMETRY 2:  
EXPANDING SQUARES



DARK  
OR  
BRIGHT  
BACKGROUND

FIGURE 2.11.  
INTENSITY OBSERVED AT CENTER OF SQUARE PATCH

$$\lambda = 5500 \text{ \AA}$$

$$\theta^0 = 22^0$$

ALBEDO SET = (INSIDE ALBEDO, OUTSIDE ALBEDO)

FOOTPRINT = CIRCULAR WITH 30 METER RADIUS

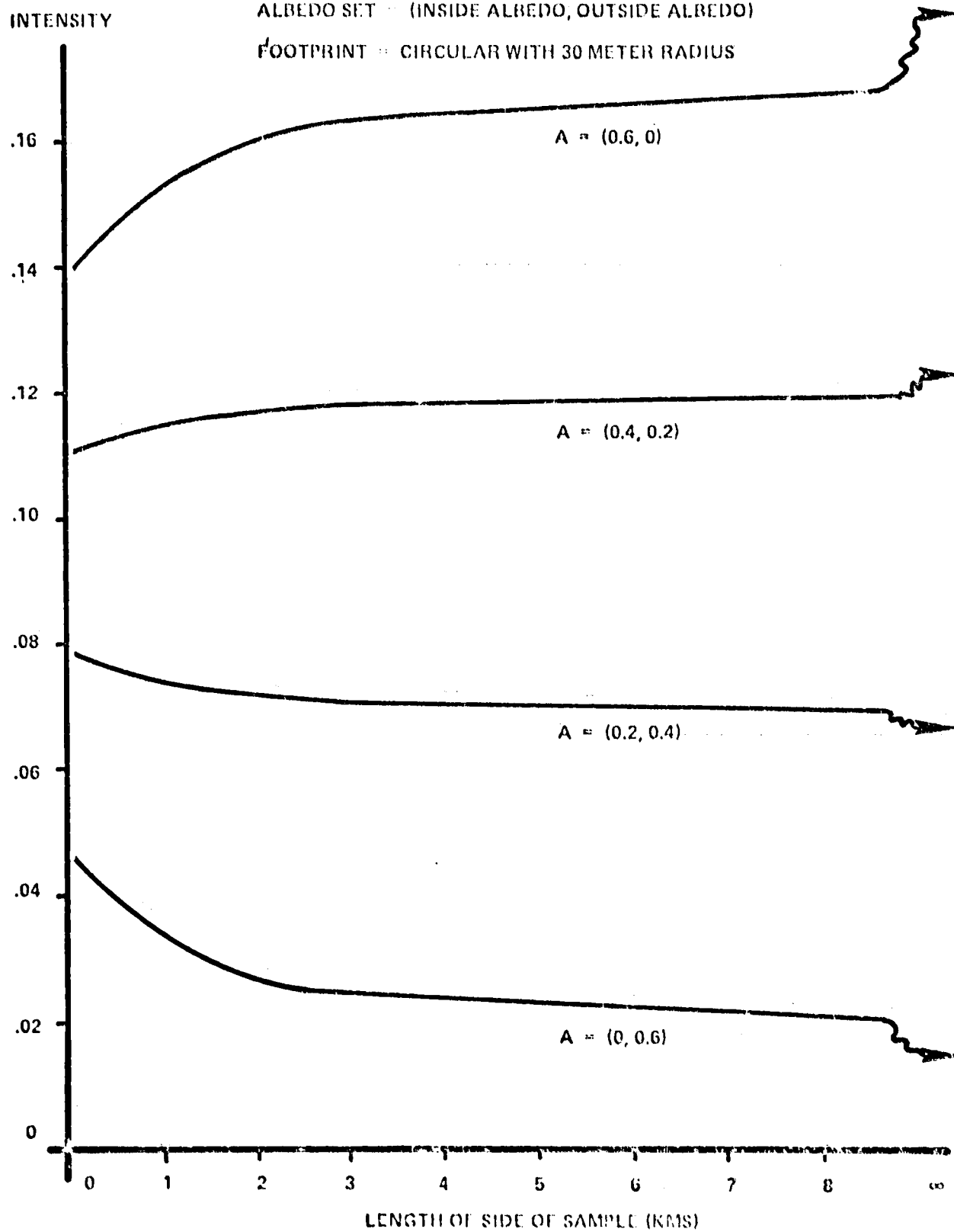


FIGURE 2.12.  
INTENSITY VS TARGET SQUARE EDGE LENGTH

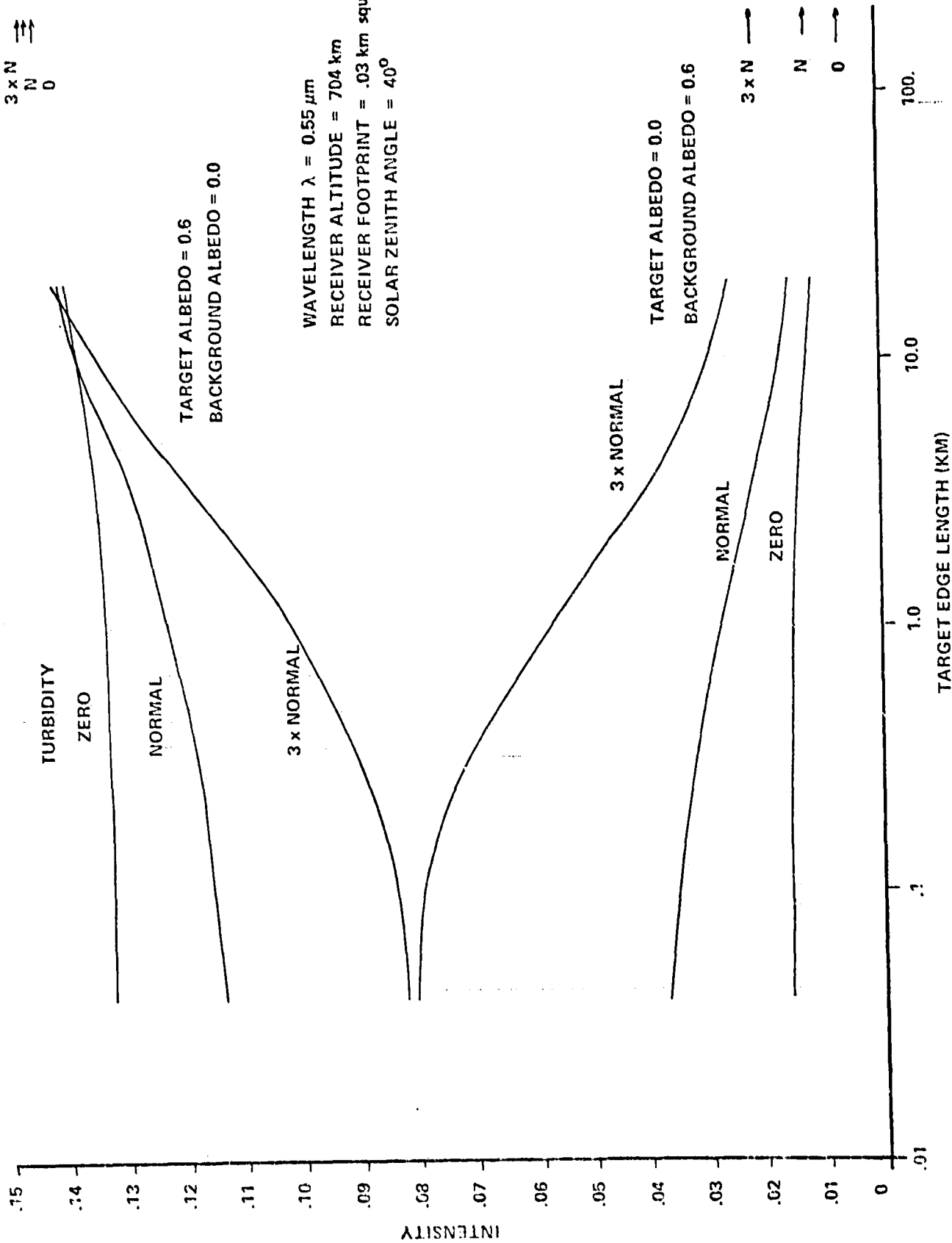
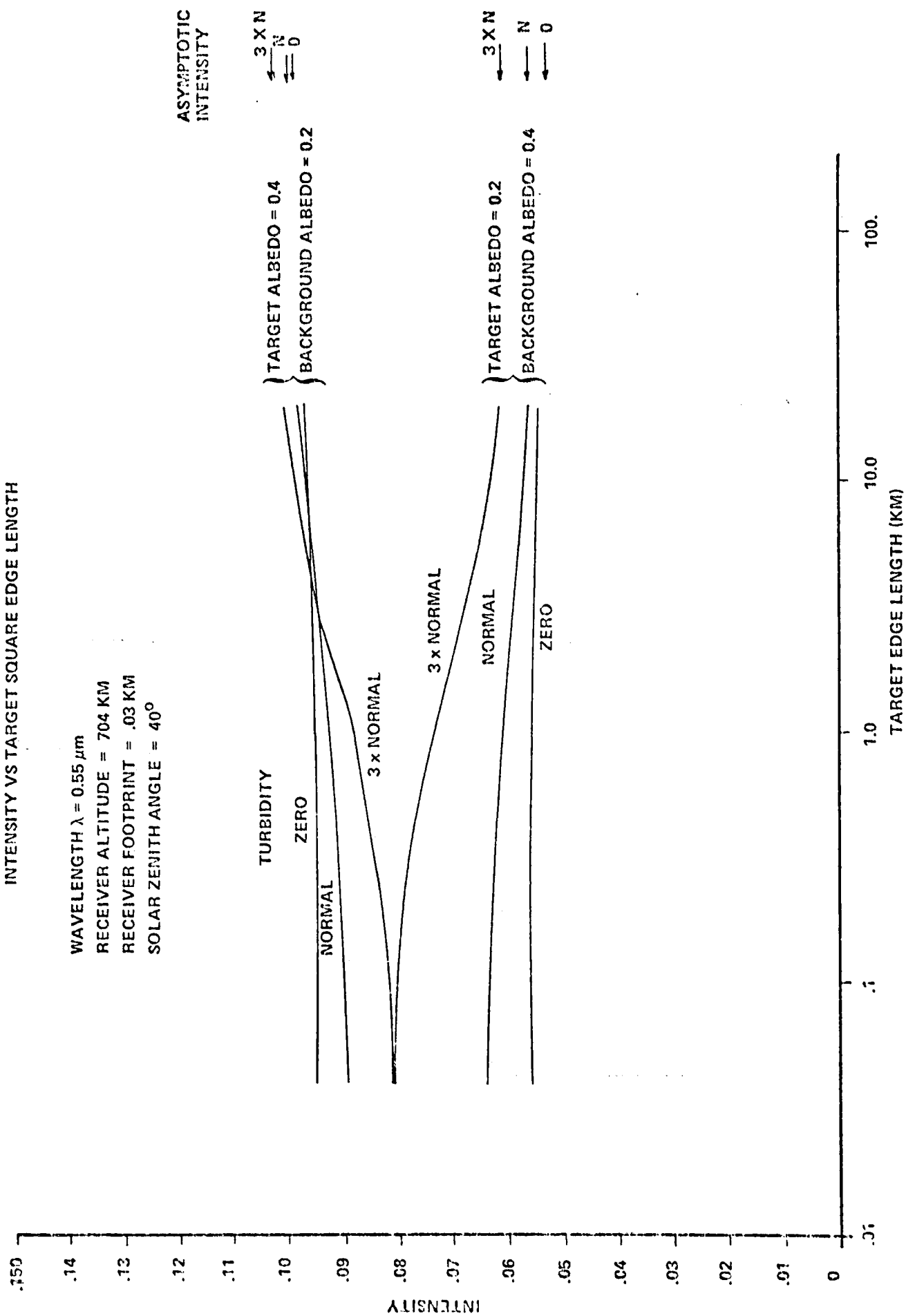


FIGURE 2.13.  
INTENSITY VS TARGET SQUARE EDGE LENGTH



### 2.3 CHECKERBOARD FIELDS

The ground as viewed from a satellite more nearly resembles a patchwork pattern than any of the albedo patterns we have studied thus far. It is clear that this will modify the behavior of the intensity along a scan across the ground. This can be expected primarily because that part of the sensed radiance which originates from ground scattering outside the field of view tends towards some average value as the "grain" of the ground pattern becomes finer and finer. In order to study this effect, we have modeled the ground pattern as a checkerboard with alternating high and low albedo squares. Our simulations modeled a scan across a typical boundary by simultaneously modeling a number of such checkerboard patterns with incremental displacements in position with respect to the IFOV. This pattern is shown schematically in figure 2.14.

There is an additional, more technical reason for studying a checkerboard pattern. As shown in section 4, the gradient of the intensity across an albedo boundary is a measure of the atmospheric spread function and will be faithful if the regions on either side of the boundary are sufficiently large. We have examined checkerboard patterns to give an indication as to how large these regions must be.

Figures 2.15 through 2.23 illustrate our results for checkerboards with "checks" one kilometer square. Since the effects which we wish to study here are maximal at shorter wavelengths, we show the results for  $\lambda=0.47\mu\text{m}$ . This set of calculations includes turbidities 0, 1, and 3 and checkerboards with the following sets of contrasting albedos: (0.2, 0.15), (0.4, 0.2), (0.6, 0.0). In all cases shown here, the IFOV was 30 m square and the solar zenith angle was  $40^\circ$ .

In order to evaluate the relative impact of the checkerboard pattern on intensity gradient methods for measuring



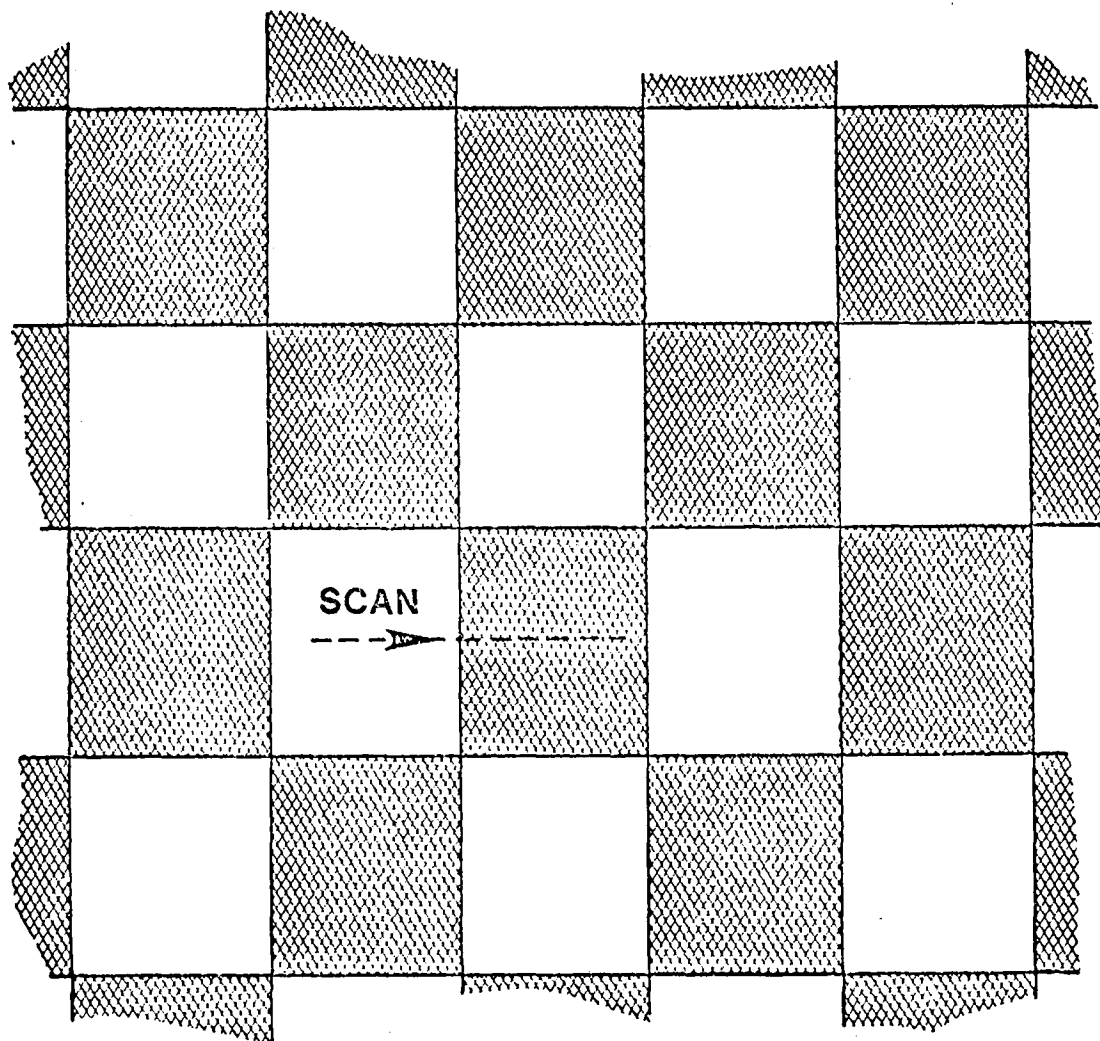


FIGURE 2.14. SCHEMATIC ILLUSTRATION OF CHECKERBOARD REFLECTANCE PATTERN

FIGURE 2.15.

INTENSITY VS DISTANCE FROM BOUNDARY  
CHECKERBOARD COMPARED TO SEMI-INFINITE PLANE

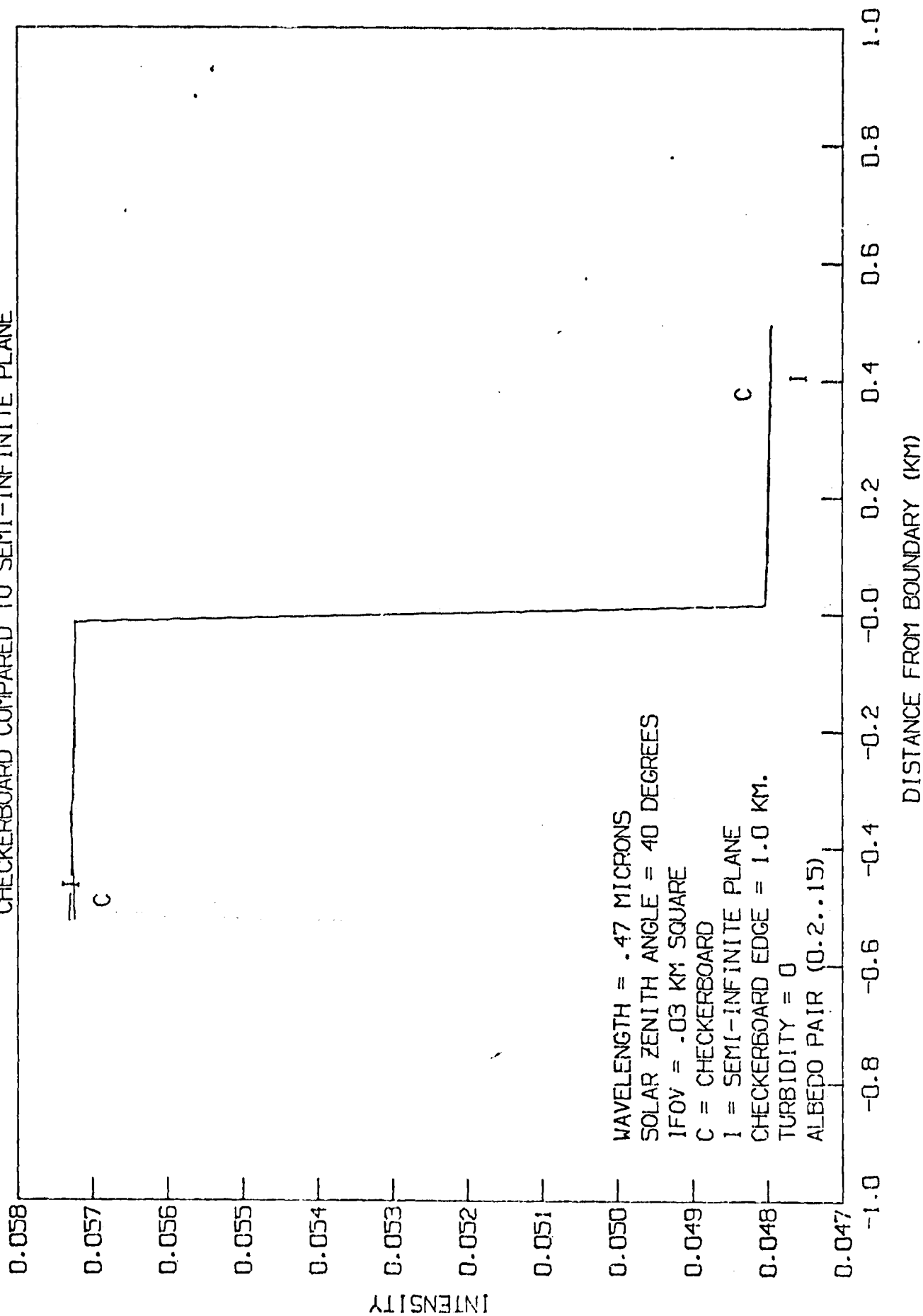


FIGURE 2.16.

INTENSITY VS DISTANCE FROM BOUNDARY  
CHECKERBOARD COMPARED TO SEMI-INFINITE PLANE

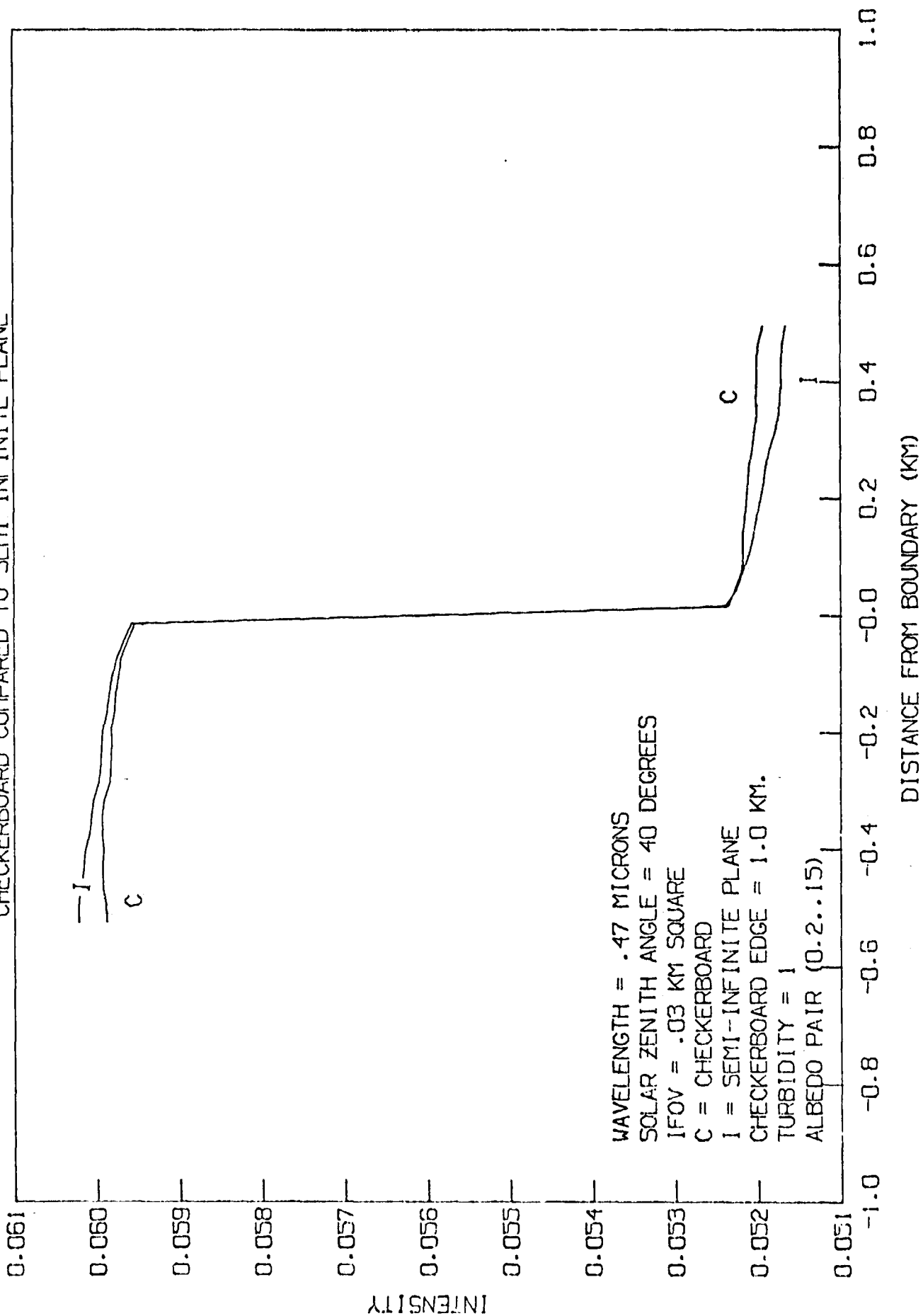


FIGURE 2.17.  
INTENSITY VS DISTANCE FROM BOUNDARY  
CHECKERBOARD COMPARED TO SEMI-INFINITE PLANE

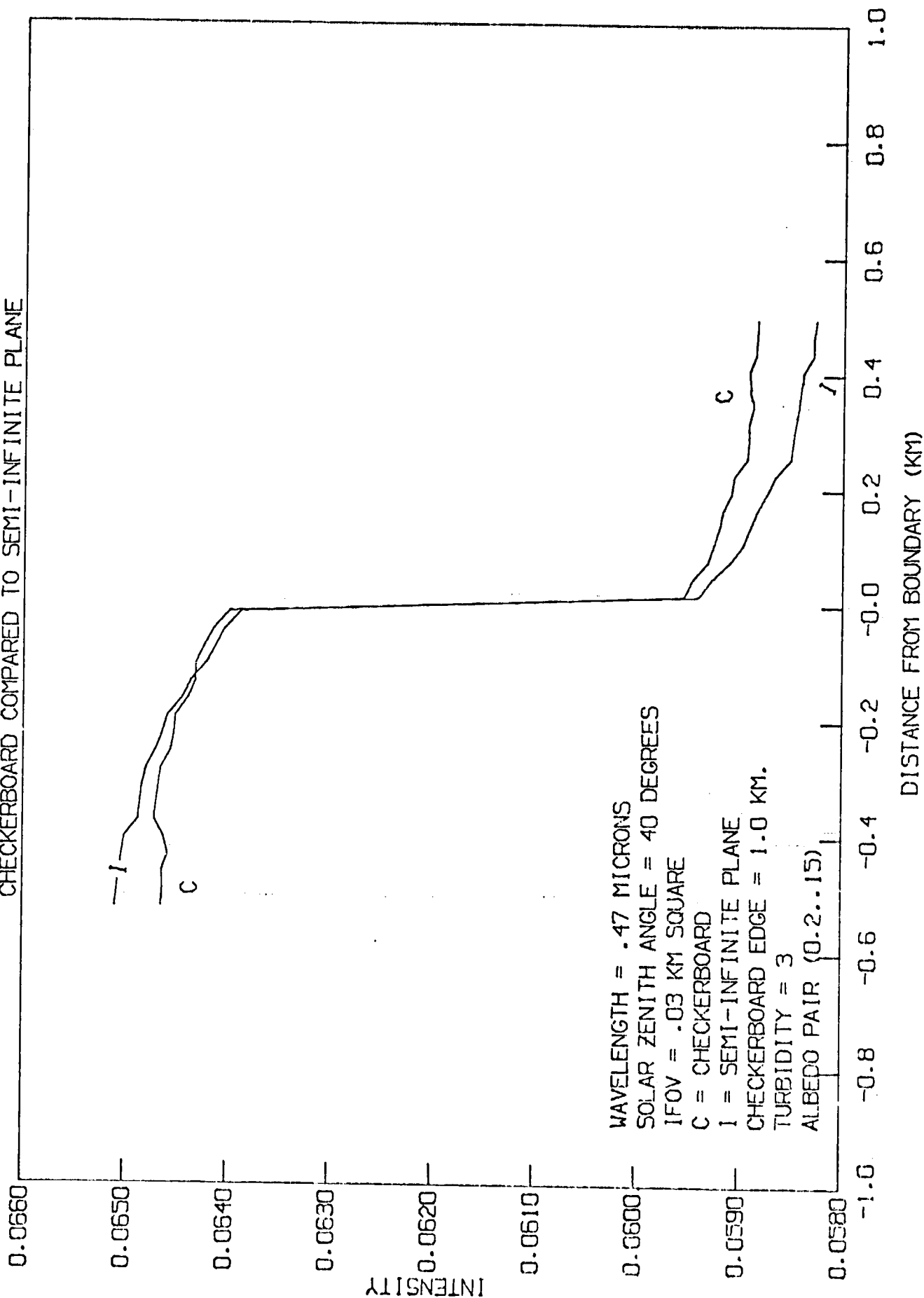


FIGURE 2.18.

INTENSITY VS DISTANCE FROM BOUNDARY  
CHECKERBOARD COMPARED TO SEMI-INFINITE PLANE

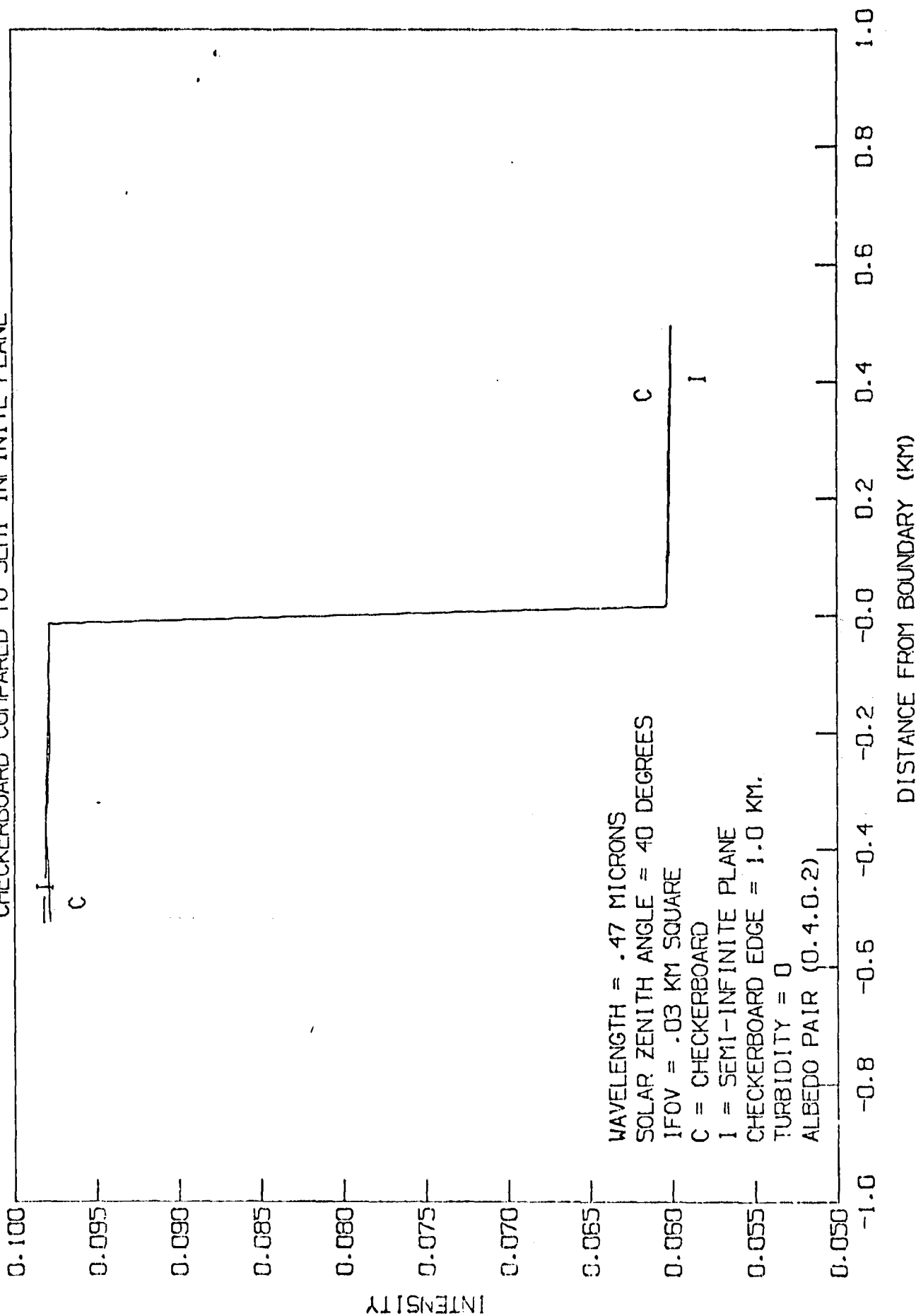


FIGURE 2.19.

INTENSITY VS DISTANCE FROM BOUNDARY  
CHECKERBOARD COMPARED TO SEMI-INFINITE PLANE

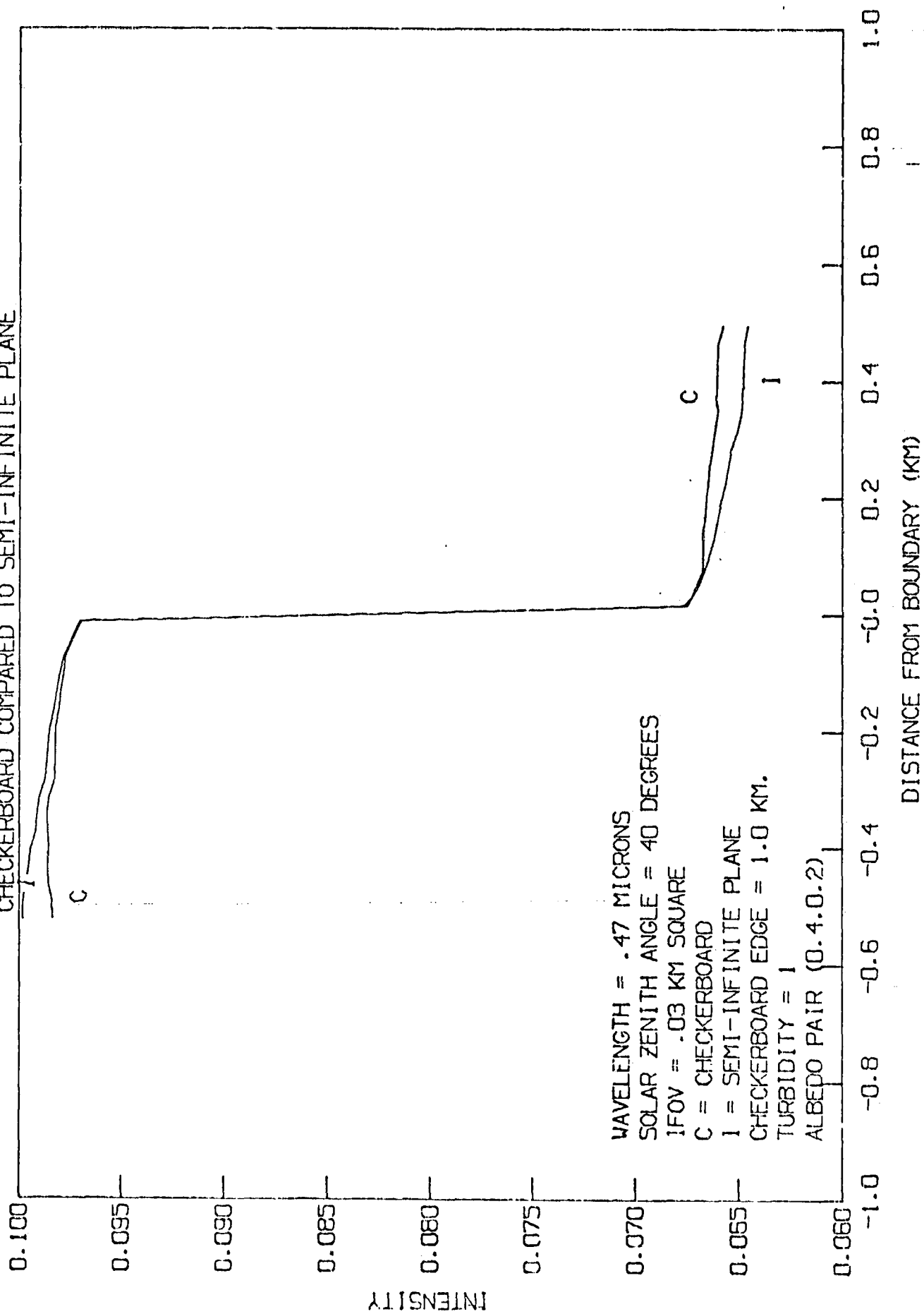


FIGURE 2.20.

INTENSITY VS DISTANCE FROM BOUNDARY  
CHECKERBOARD COMPARED TO SEMI-INFINITE PLANE

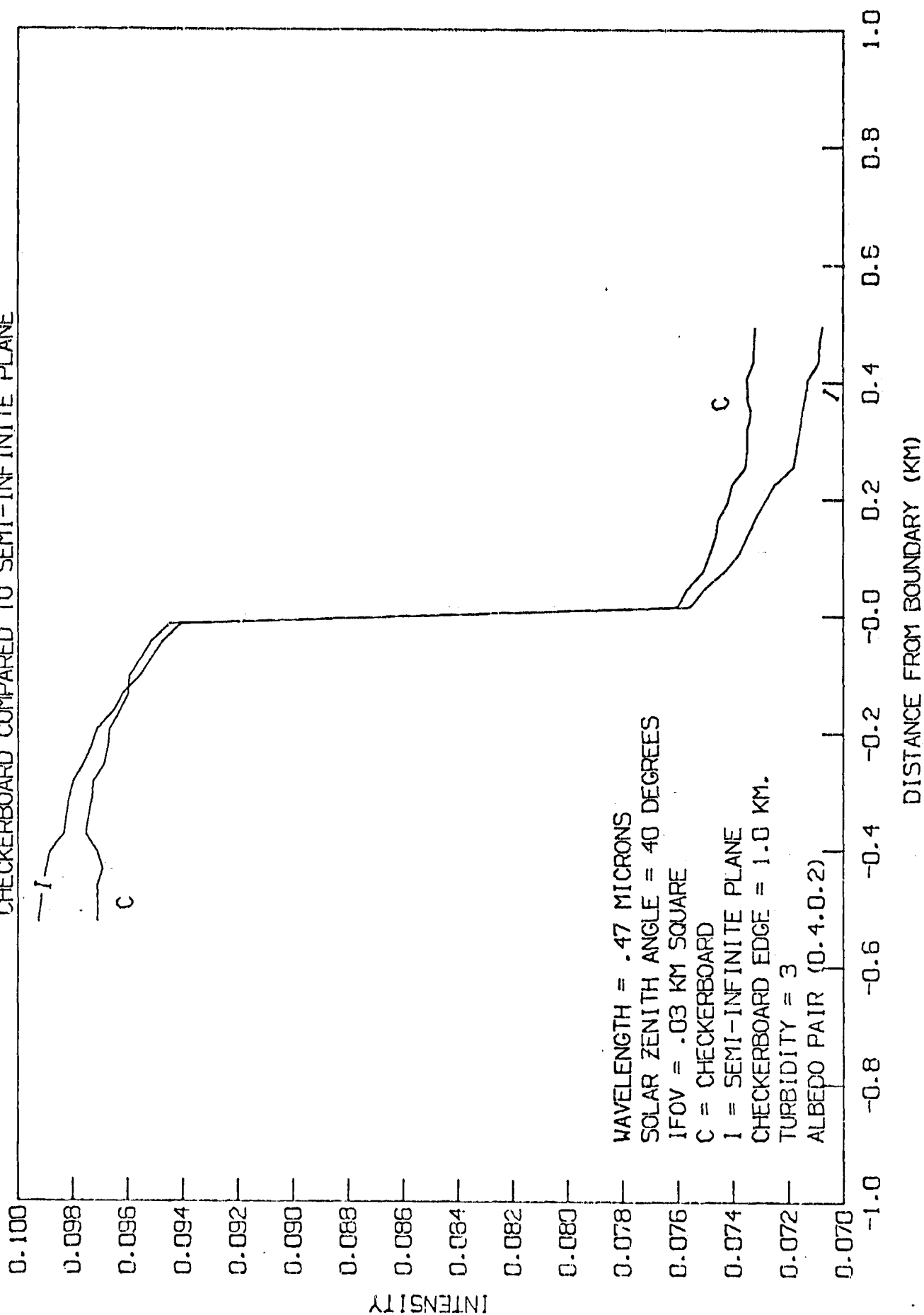


FIGURE 2.21.  
 INTENSITY VS DISTANCE FROM BOUNDARY  
 CHECKERBOARD COMPARED TO SEMI-INFINITE PLANE

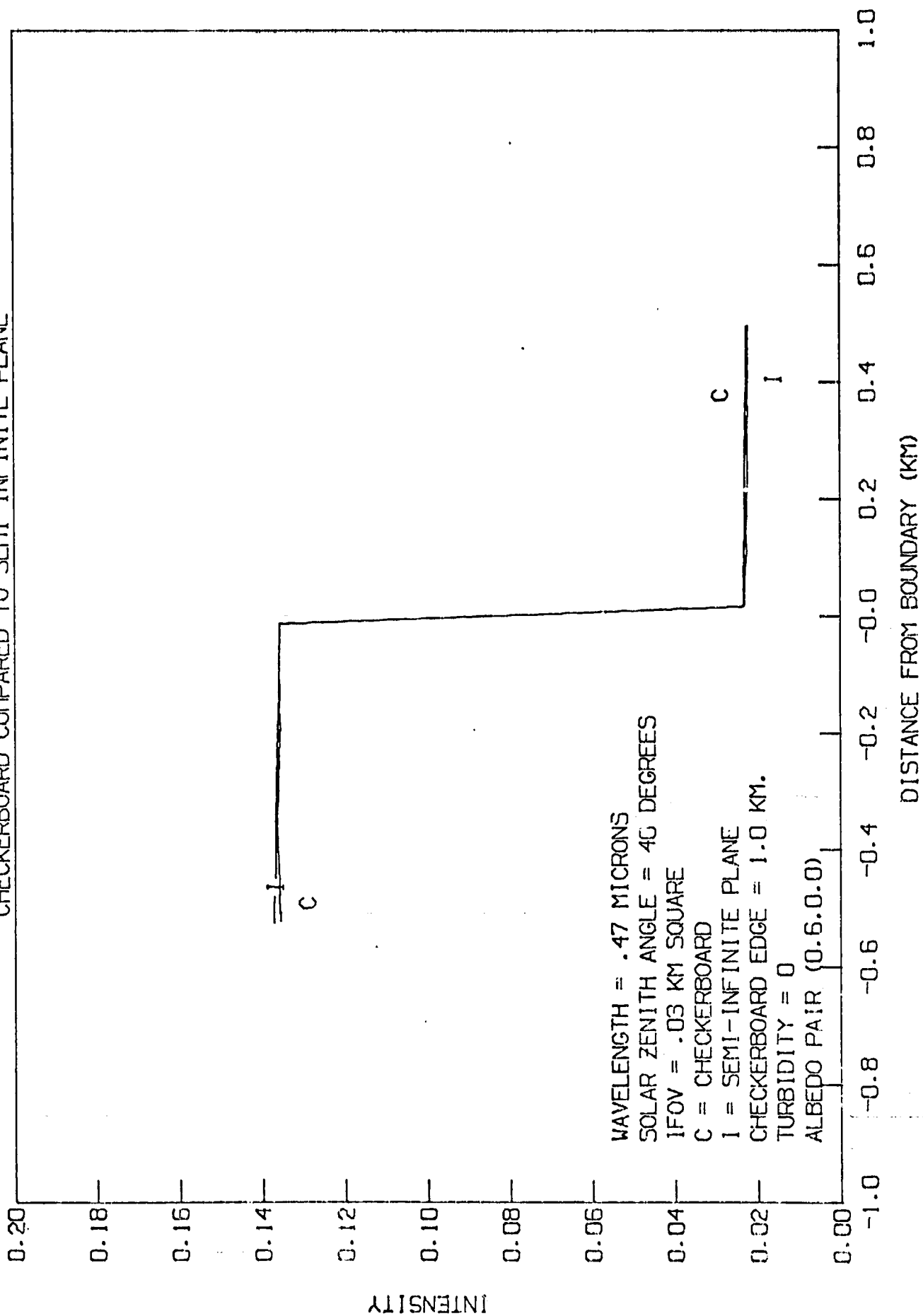




FIGURE 2.22.

INTENSITY VS DISTANCE FROM BOUNDARY  
CHECKERBOARD COMPARED TO SEMI-INFINITE PLANE

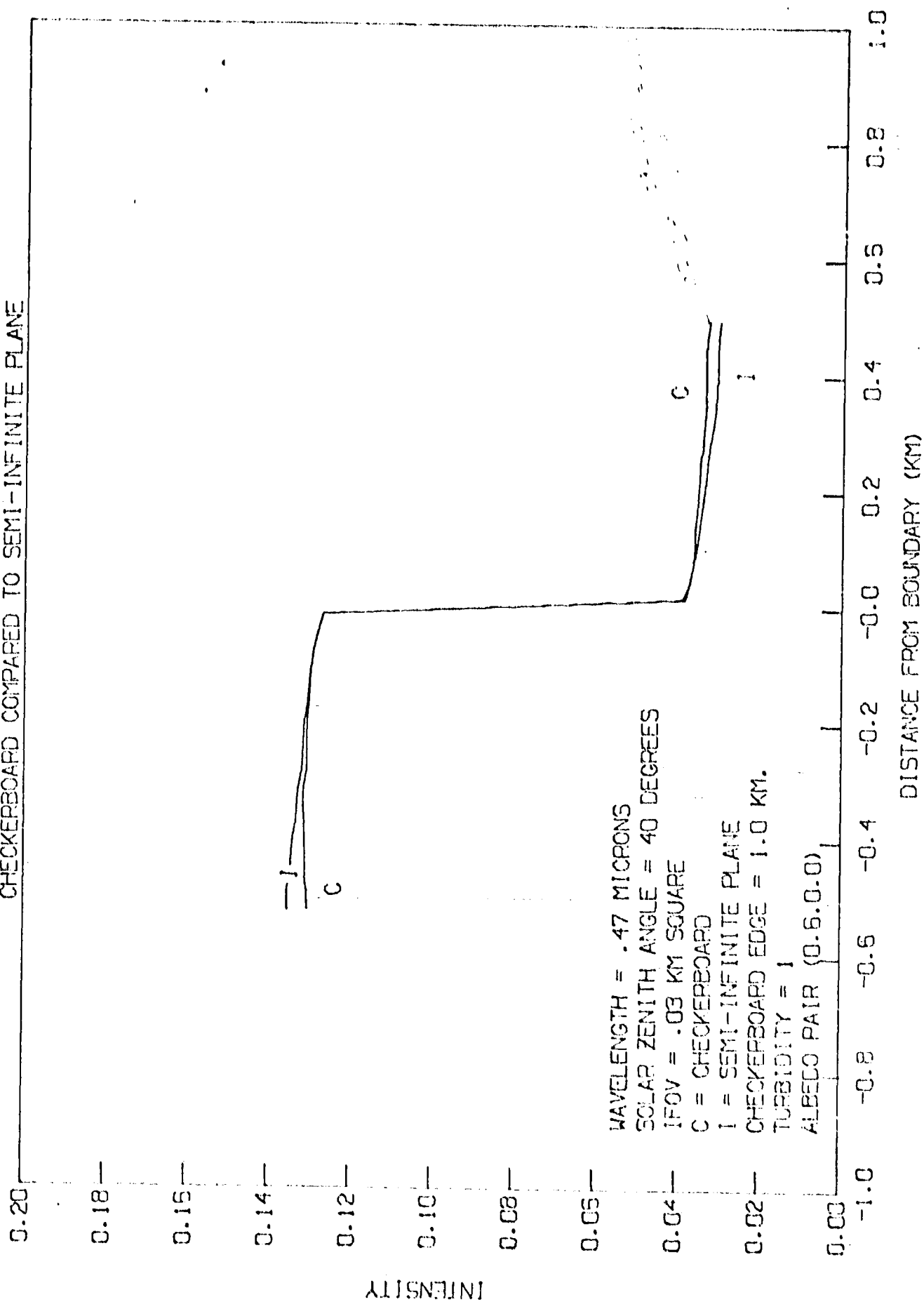
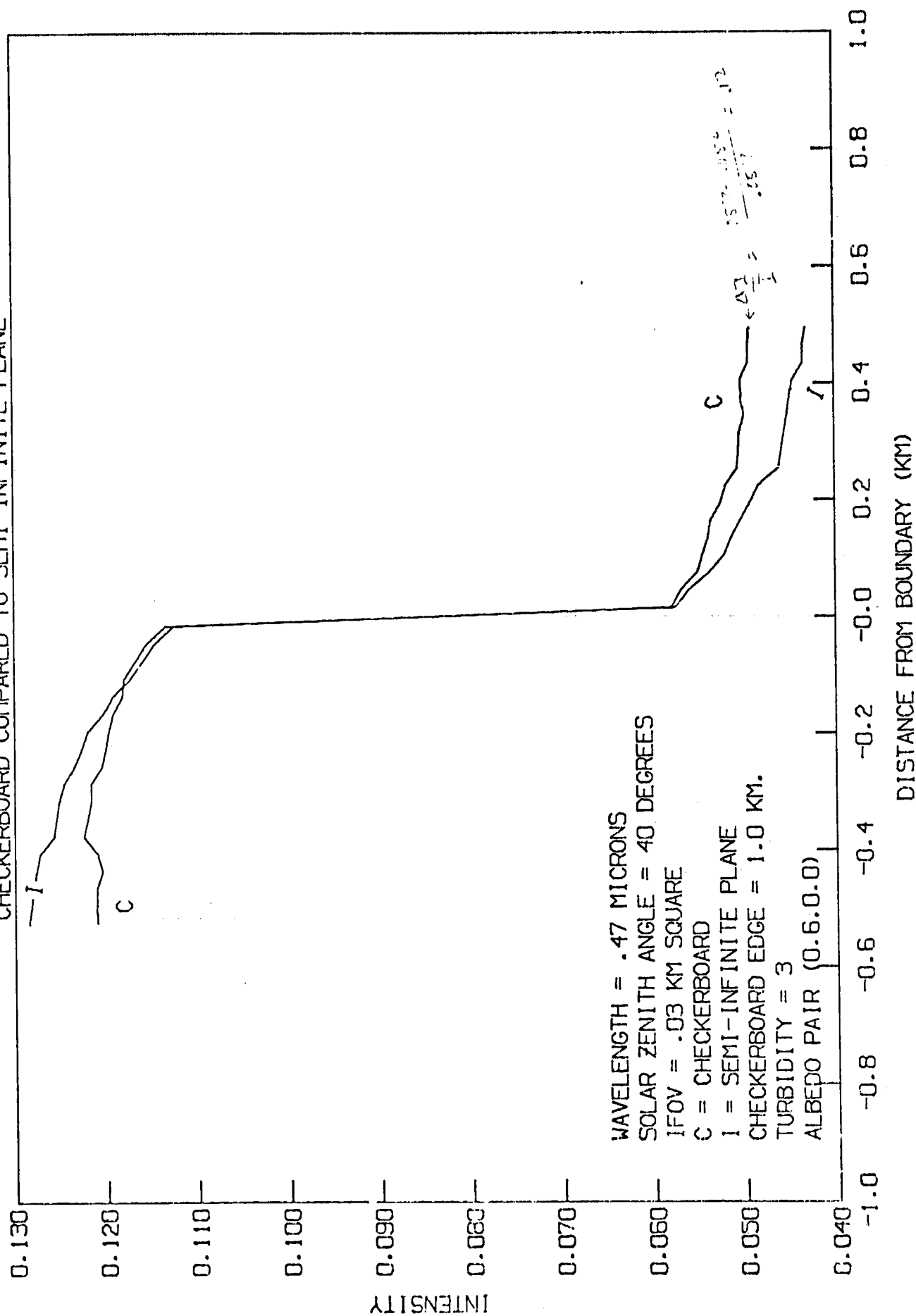


FIGURE 2.23.

INTENSITY VS DISTANCE FROM BOUNDARY  
CHECKERBOARD COMPARED TO SEMI-INFINITE PLANE



the spread function, we simultaneously modeled a scan across the boundary of a semi-infinite plane. These curves (labeled I) are also shown in the figures for comparison with the checkerboard pattern results (labeled C in the figures).

The results shown are not smoothed since they have been automatically plotted. The roughness in the curves reflects the statistical jitter inherent in Monte Carlo computation. The fact that the jitter in the results are correlated is a consequence of their having been computed simultaneously (i.e., with the same set of "photons") so that statistical variations are shared.

The intensity variation across the boundary may be seen to be appreciably flatter for the checkerboard pattern than for the semi-infinite plane. This is to be expected, for on symmetry arguments alone it must be true that

$$\left. \frac{dI}{dx} \right|_{x=x_0} = 0$$

where  $x$  denotes the distance along a scan perpendicular to a boundary and  $x_0$  denotes the center or center-line position on a square.

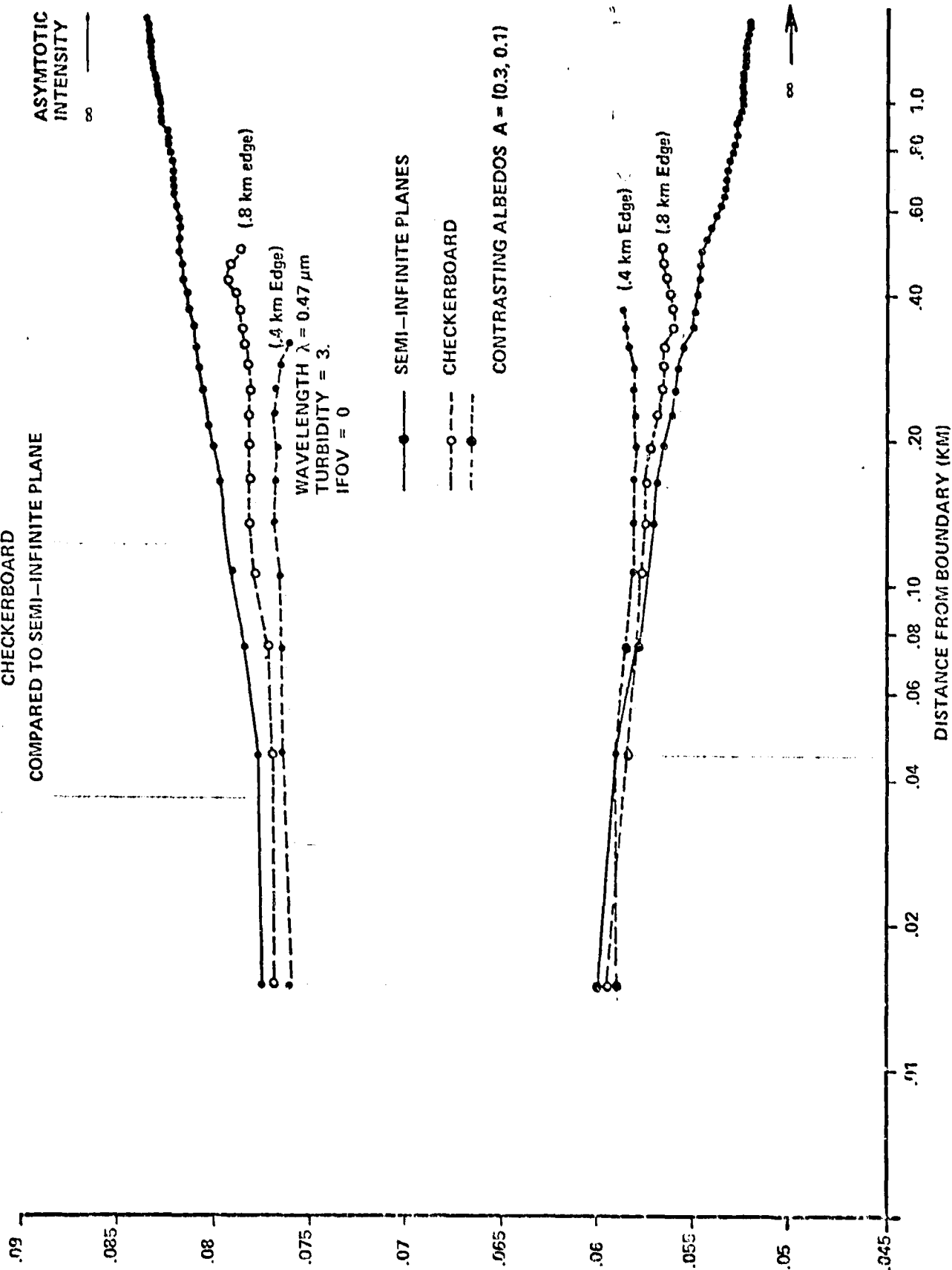
The intensity gradient very near to the boundary is seen, however, to be very nearly the same for the two patterns. This means that the inner part of the spread function might indeed be measured by intensity gradient methods when the field sizes are this large. Of course, smoothing would be very necessary for gradient methods since differentiation is an inherently noisy process.

It is of interest to investigate the effect of shrinking the scale of the checkerboard pattern. In our initial attempts to do so, we noticed increasing level of statistical

jitter as the pattern became finer and finer. This can be traced, in part, to the statistical variation in the distribution of photons over the field of view (even though the field of view is already quite small). In order to suppress these effects, we adopted an infinitesimal field of view and computed results for pixel centers separated by 30 m. Figure 2.23 compares results for checkerboards with edge lengths of 0.4 km and 0.8 km with the results for a semi-infinite plane boundary. Here, the turbidity=3, the wavelength was  $0.47\mu\text{m}$  and the contrasting albedoes were (0.3, 0.1). Also shown are the asymptotic values of the intensity which would be achieved over an infinite uniform plane. The curves in the figure appear in two branches corresponding to each side of the boundary.

As may be seen, for field sizes as small as 0.4 km the gradient method may only be used quite close to the boundary (3 to 4 pixels away) and becomes unreliable at greater distances as a guide to the behavior of the spread function. This critical distance increases when the field size increases. It is interesting to note that gradient methods seem likely to be more usable on the dark side of the boundary. This is a consequence, we believe of the effects of the variation in the illumination of the ground.

### CHECKERBOARD INTENSITY VS. DISTANCE FROM BOUNDARY COMPARED TO SEMI-INFINITE PLANE



### SECTION 3.0

#### CALIBRATION EFFECTS

One of the main problems encountered in an effort to apply satellite observations to the classification of regions on the ground is that of calibration. The calibration of sensed radiances to ground albedos is made more difficult by effects attributable to atmospheric scattering.

Even for the simplest conceivable ground reflectance pattern, a uniform plane, the calibration curve relating radiance to ground albedo is non-linear. The non-linearity results from photons which scatter multiply from the ground, thus illuminating regions of high albedo more strongly than regions of low albedo. There is also a residual radiance due to light scattered into the receiver without having interacted with the ground. This we call "path radiance" or  $I_0$ .

The calibration equation for uniform ground planes may be easily derived. Let  $S$  be the overall probability that a photon which has been scattered from the ground returns to the ground. Let  $T$  be the probability that a photon reflected at the ground is scattered into the receiver multiplied by the flux incident upon the ground. The albedo  $A$  is the probability that a photon incident upon the ground will be reflected (rather than absorbed). Then

$$I = I_0 + TA[1+SA+(SA)^2+(SA)^3+....] \quad (3.1)$$

or

$$I = I_0 + \frac{TA}{1-SA} \quad (3.2)$$

Calibration curves, computed by CTRANS, for uniformly Lambertian ground planes are given in Figures 3.1 through 3.3.

$I_0$ ,  $T$ , and  $S$  are all dependent upon atmospheric composition and structure and are in themselves difficult to compute analytically. They are all very closely correlated, however, as shown in Figures 3.4 through 3.6. The figures are based upon values derived from uniform plane cases (with solar zenith angle=40° and receiver nadir angle=0°) for wavelengths 0.47, 0.55, and 1.65  $\mu\text{m}$  and turbidities  $T=0,1$ , and 3. Table 3.1 lists the numerical values obtained for  $I_0$ ,  $T$ , and  $S$  for these cases. Also shown in the figures are least squares fits to the points using both linear and power law forms. The goodness of fit is measured by the correlation coefficient

$$r^2 = \frac{\left| \sum x_i y_i - \frac{\sum x_i \sum y_i}{n} \right|^2}{\left[ \sum x_i^2 - \frac{(\sum x_i)^2}{n} \right] \left[ \sum y_i^2 - \frac{(\sum y_i)^2}{n} \right]} \quad (3.3)$$

for a linear fit; for a power law fit,  $x_i$  and  $y_i$  are replaced by  $\ln x_i$  and  $\ln y_i$ .  $n$  is the number of fitted points.

Table 3.1. Uniform Plane Intensity Calibration Constants  
 Solar Zenith Angle =  $40^\circ$   
 Receiver Nadir Angle =  $0^\circ$

$\lambda (\mu\text{m})$	t	$e^{-\tau}$	$\tau$	$I_o$	T	S
.47	0	.828	.1893	.01730	.1967	.1416
.47	1	.649	.4329	.02130	.1894	.2084
.47	3	.398	.9201	.03278	.1638	.2671
.55	0	.905	.1004	.01036	.2161	.0825
.55	1	.731	.3127	.01422	.2031	.1414
.55	3	.478	.7375	.02351	.1828	.2280
1.65	0	.999	.0012	.00005	.2435	.0013
1.65	1	.928	.0745	.00163	.2339	.0307
1.65	3	.802	.2212	.00468	.2296	.0735



FIGURE 3.1.  
INTENSITY AT SATELLITE  
VS.  
UNIFORM PLANE SURFACE ALBEDO

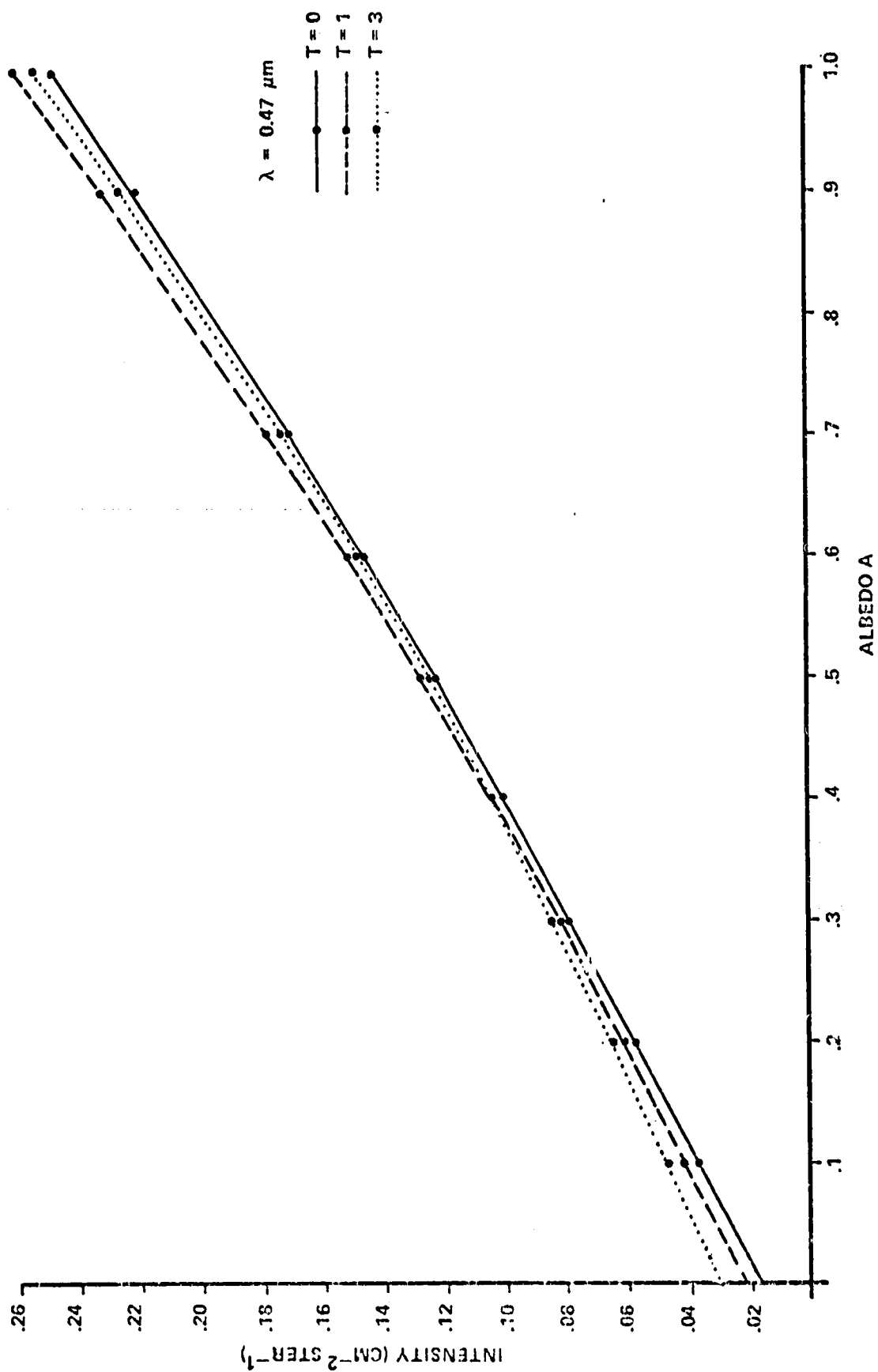


FIGURE 3.2.  
INTENSITY AT SATELLITE  
VS.  
UNIFORM PLANE SURFACE ALBEDO

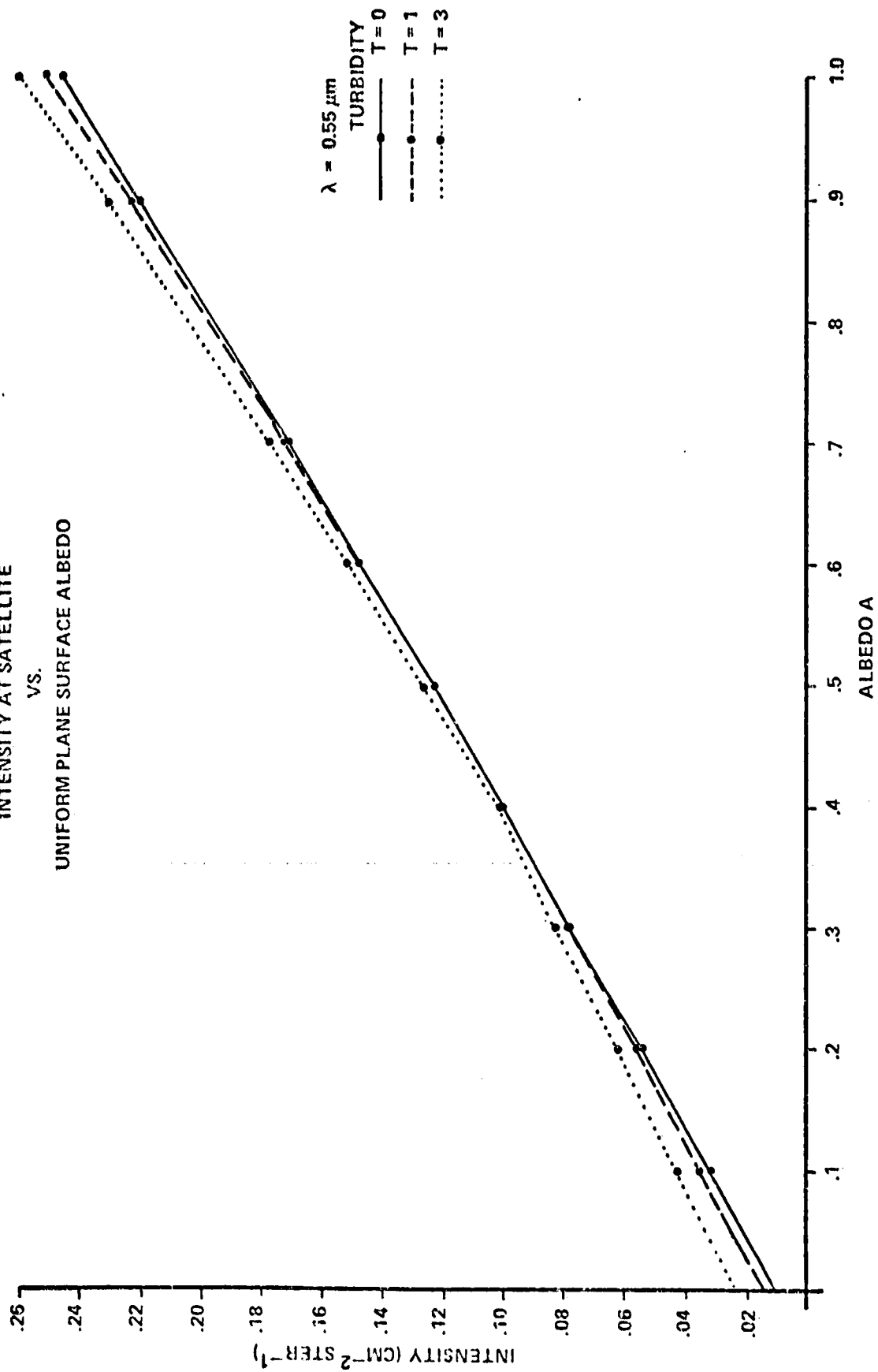


FIGURE 3.3.  
 INTENSITY AT SATELLITE  
 VS.  
 UNIFORM PLANE SURFACE ALBEDO

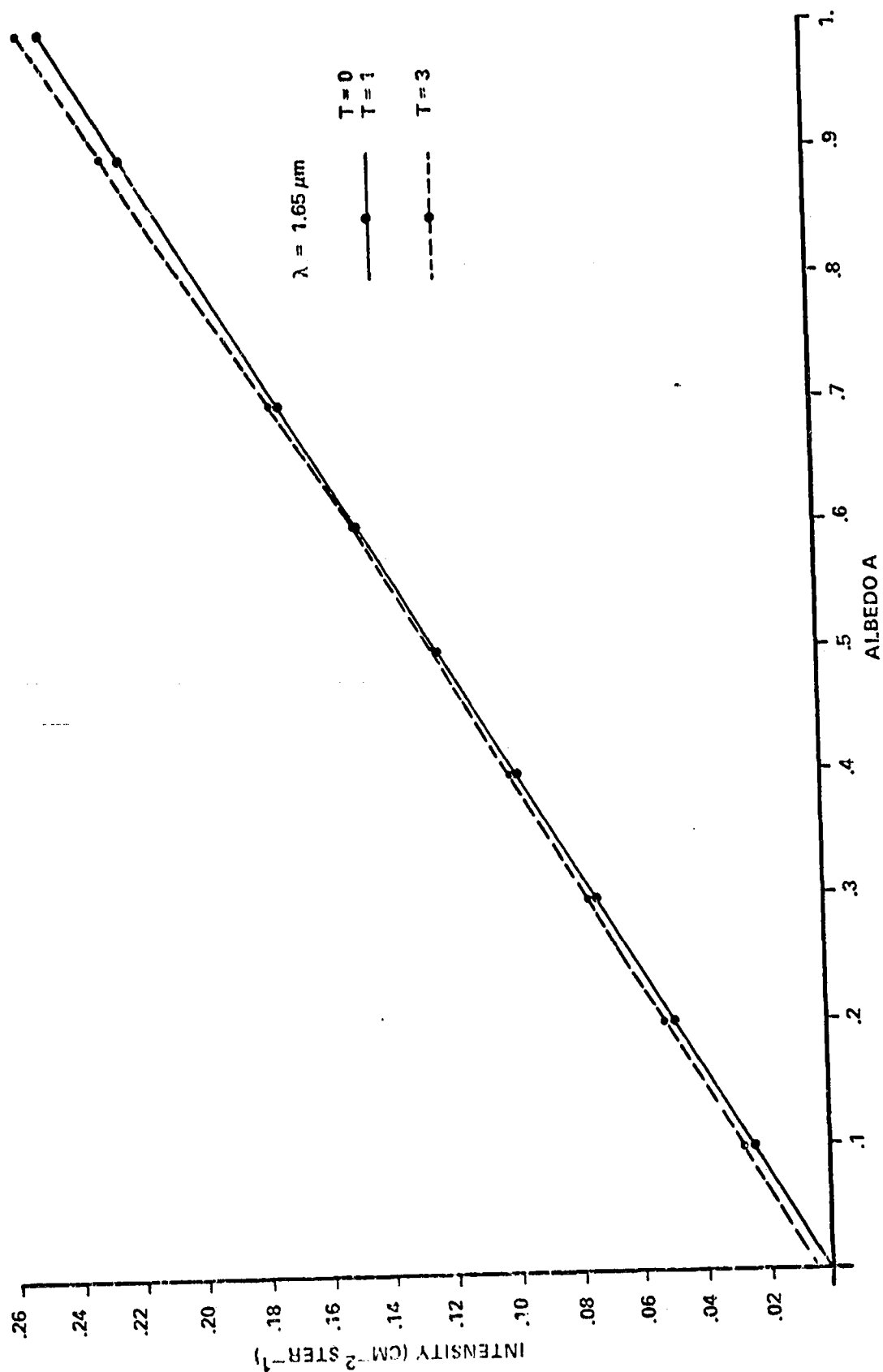


FIGURE 3.4.  
CALIBRATION CONSTANTS  
 $I_0$  AS A FUNCTION OF  $S$

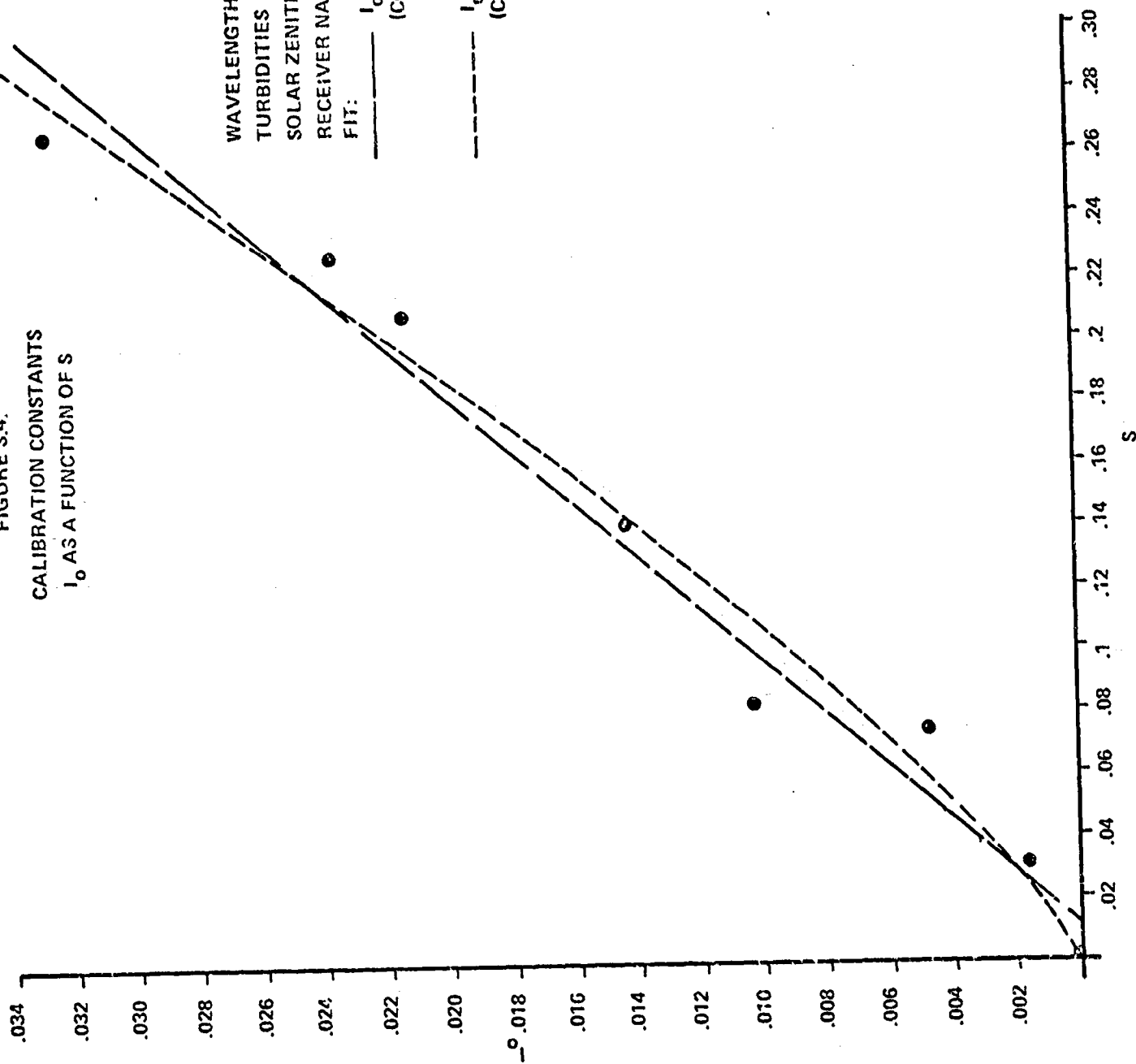


FIGURE 3.5.  
CALIBRATION CONSTANTS  
 $I_0$  AS A FUNCTION OF T

WAVELENGTHS  $\lambda = 0.47, 0.55, 1.65 \mu\text{m}$   
TURBIDITIES  $T = 0, 1, 3$   
SOLAR ZENITH ANGLE  $= 40^\circ$   
RECEIVER NADIR ANGLE  $= 0^\circ$

FIT:  
—  $I_0 = .3867 (N_0/\pi - T)$   
(CORRELATION COEFFICIENT  
 $r^2 = 0.9933$ )  
- - -  $I_0 = .73665 (\mu_0/\pi - T)(1.2321)$   
(CORRELATION COEFFICIENT  
 $r^2 = 0.9927$ )

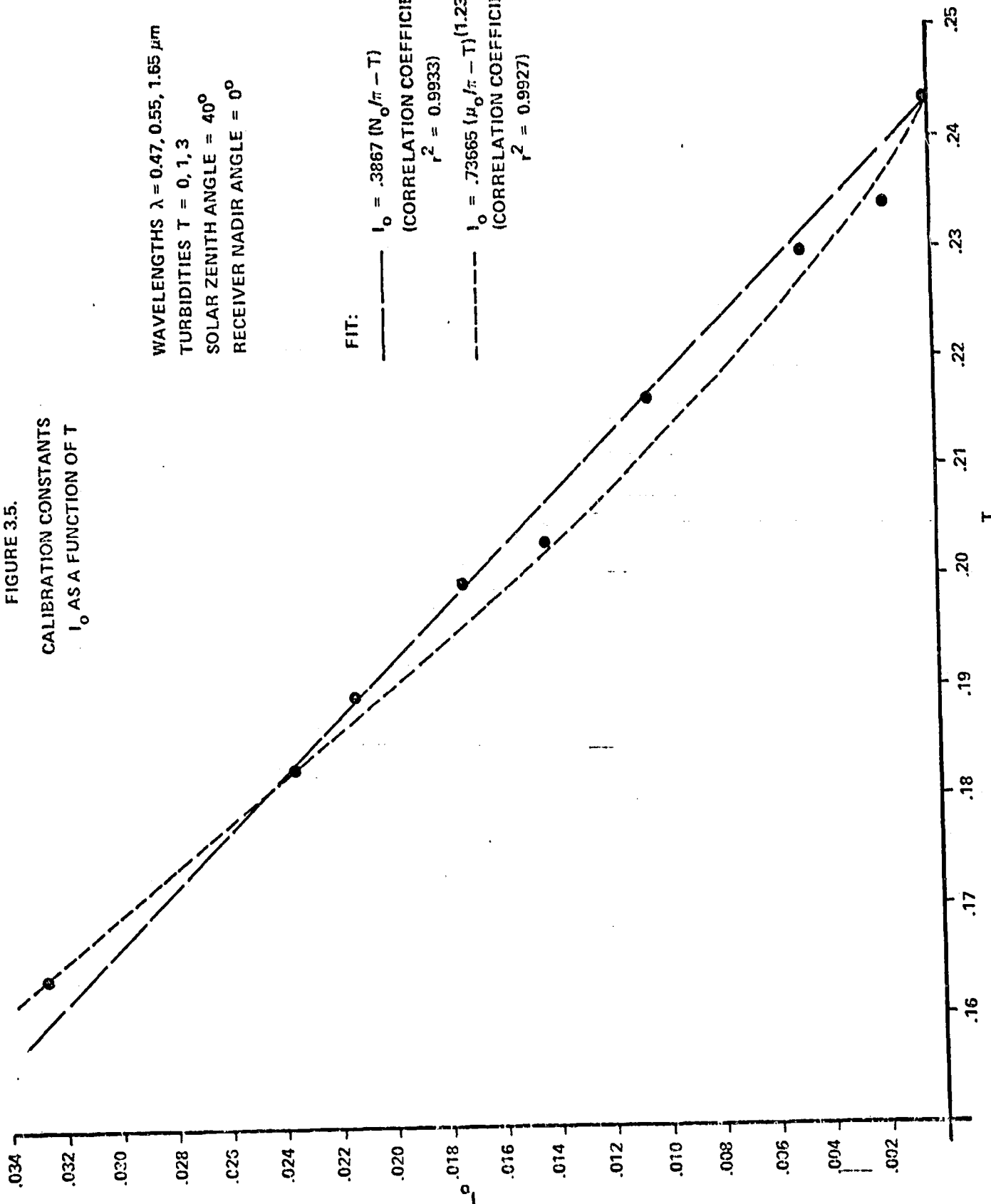
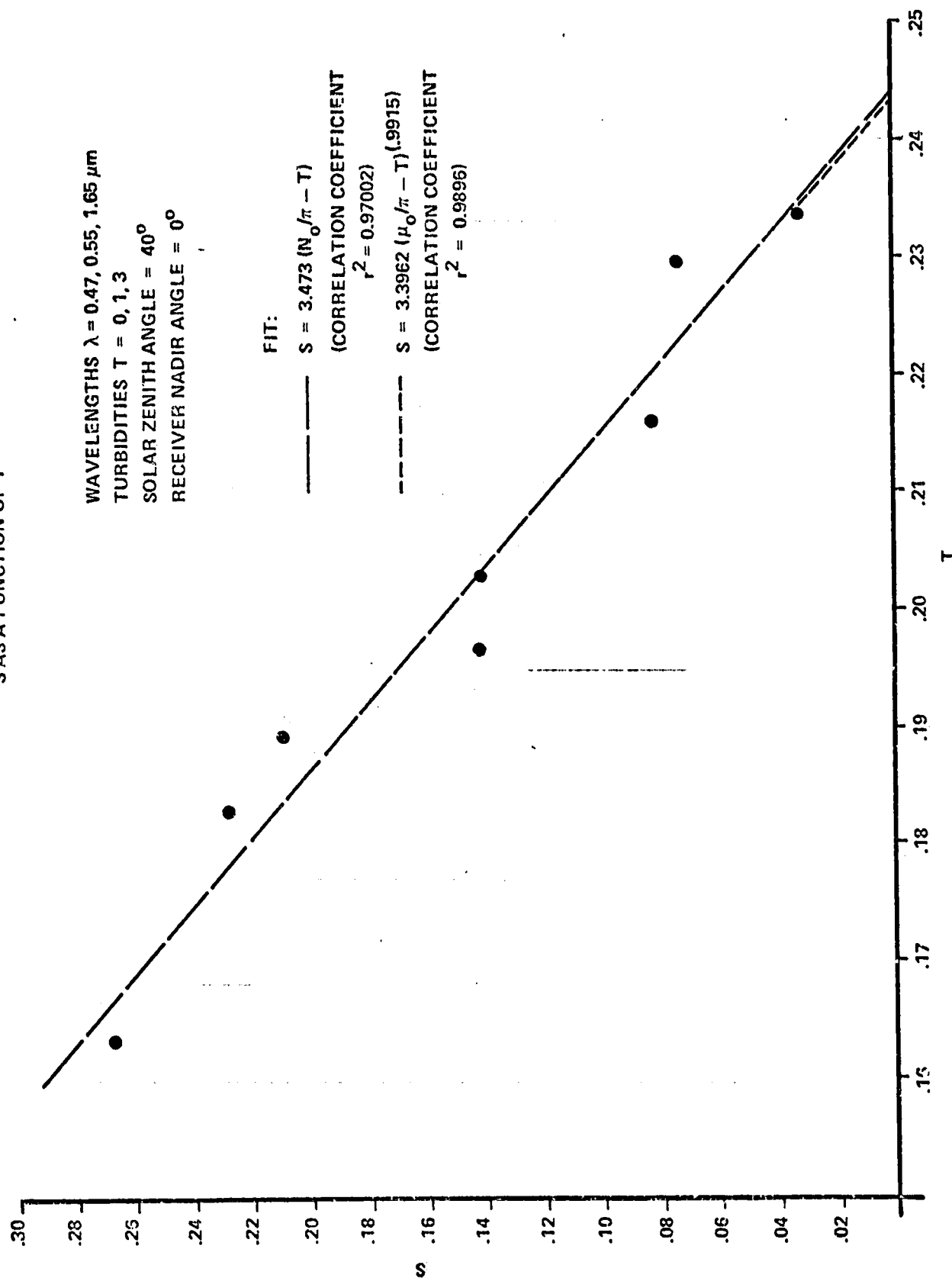


FIGURE 3.6.  
CALIBRATION CONSTANTS  
S AS A FUNCTION OF T



The regression parameters are generally functions of the solar zenith angle and receiver nadir angle.  $I_0$  and  $T$  themselves depend upon the relative geometry of the solar and receiver directions, while  $S$  depends only upon the atmosphere and ground reflectance character. Using an appropriately computed regression relationship, then, one might deduce approximate values for any pair of the parameters given a knowledge of one of them.

Having established a set of values for  $I_0$ ,  $S$ , and  $T$  by some means, an effective albedo may be associated with a sensed radiance through the inverse of Equation 3.2:

$$\Lambda_{\text{eff}} = \frac{I - I_0}{T + S(I - I_0)} \quad (3.4)$$

The effective albedos so derived would be exact if the ground plane were uniform; i.e., the transformation 3.4 eliminates the effects of the non-linearities in the calibration curves.

The transformation of Equation 3.4 does not, however, eliminate the effects induced by an albedo boundary. Application of the transformation to intensities sensed in the neighborhood of a boundary nevertheless has merit: the shifting and scaling thus provided tend to symmetrize the boundary effects with respect to the bright and dark sides of a boundary. Examples of the effective albedo computed in this fashion using the intensity near the boundary of two uniform half-planes are shown in Figures 3.7 and 3.8. Comparison of Figure 3.8 with the corresponding sensed intensity as shown in Figure 2.7 provides a clear example of the utility of the transformation. The asymptotic values are aligned and the bunching of the intensity curves on the bright side of the boundary (caused by the convergence of the calibration curves for different turbidities) is removed; the curves corresponding to different turbidities are symmetrized.

The effective albedo obtained for the expanding squares albedo patterns are illustrated in Figures 3.9 and 3.10. Figure 3.9 may be compared with its intensity counterpart shown in Figure 2.11. Note that these are from our earlier calculation, the parameters being: Turbidity=1, wavelength =0.55  $\mu\text{m}$ , solar zenith angle  $\theta_0=22^\circ$ . Figure 3.10 illustrates the behavior of the effective albedo in a very low contrast situation. The asymptotic values achieved for infinitely large squares is also shown in the figures, dramatically illustrating the very long range effects which occur even for very large fields (edges  $\geq 8$  km).



FIGURE 3.7.  
EFFECTIVE ALBEDO VS DISTANCE FROM BOUNDARY  
STEP FUNCTION ALBEDO PATTERN (0, .6)

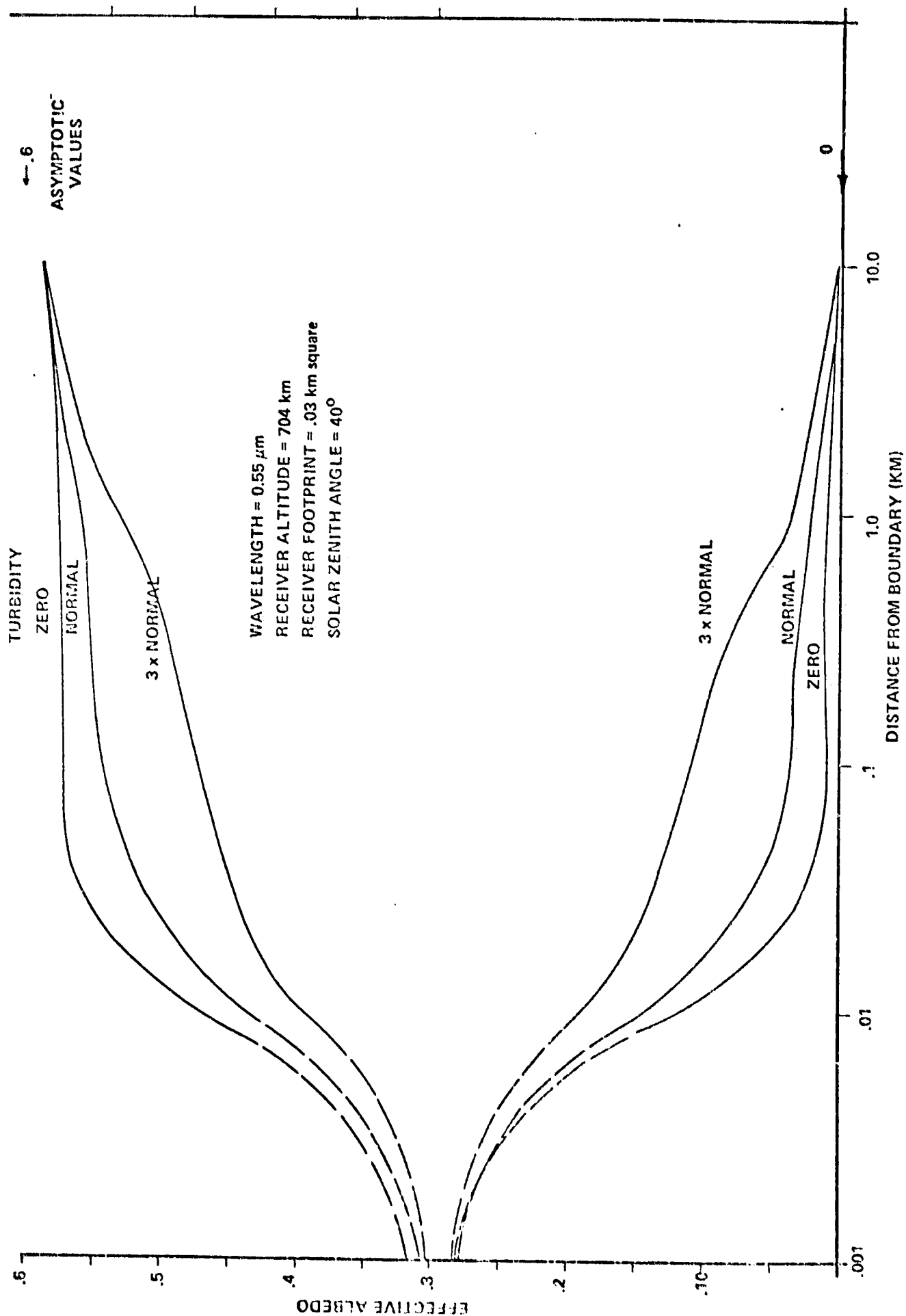


FIGURE 3.8.  
EFFECTIVE ALBEDO VS DISTANCE FROM BOUNDARY STEP  
STEP FUNCTION ALBEDO PATTERN (2, 4)

WAVELENGTH =  $0.55 \mu\text{m}$   
RECEIVER ALTITUDE = 704 km  
RECEIVER FOOTPRINT = .03 km square  
SOLAR ZENITH ANGLE =  $40^\circ$

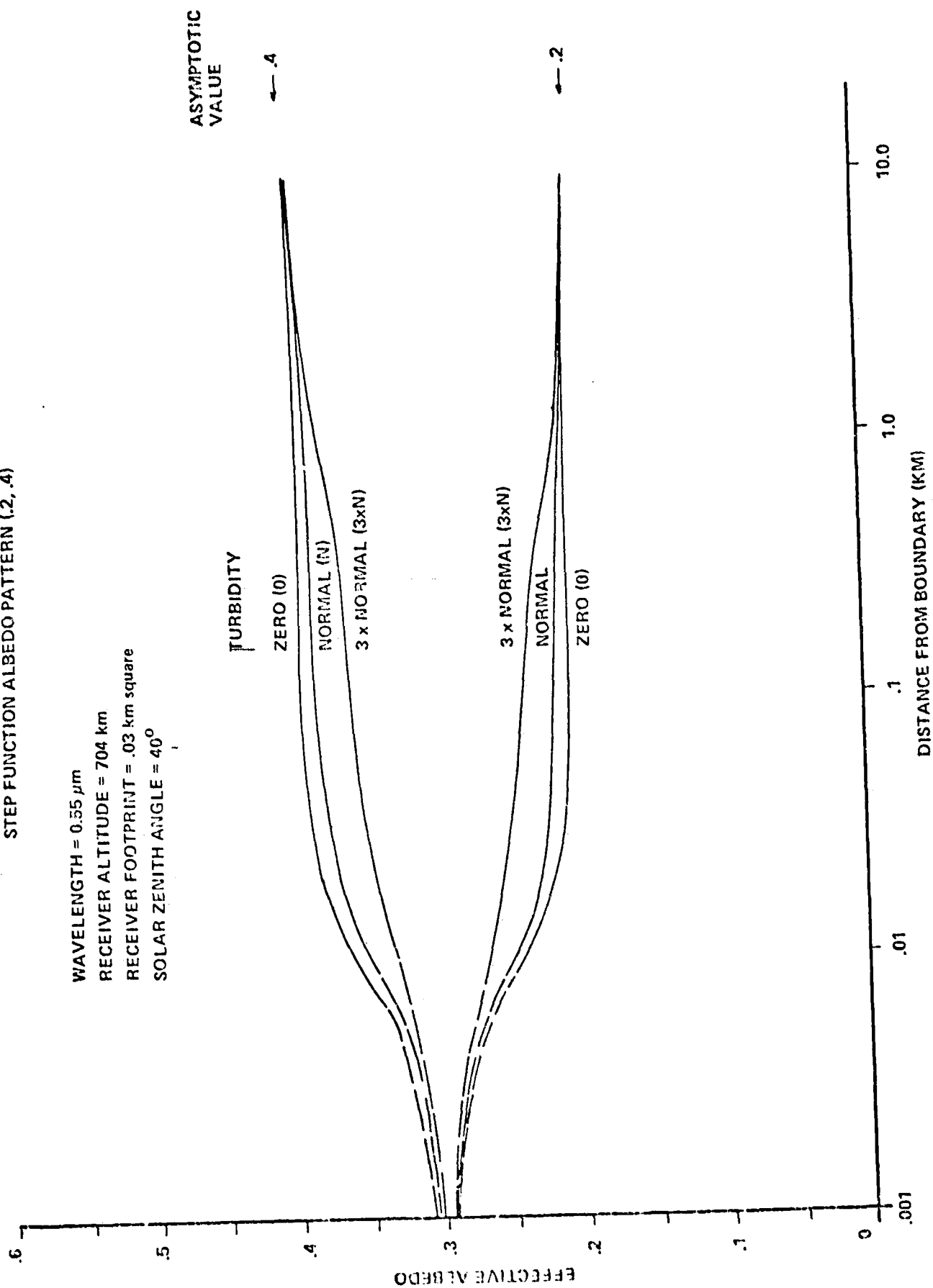


FIGURE 3.9.  
COMPUTED ALBEDO AT CENTER OF SQUARE PATCH

$$\lambda = 0.55 \mu\text{m}$$

$$\theta_o = 22^\circ$$

$$\text{TURBIDITY} = 1$$

COMPUTED  
ALBEDO

ALBEDO SET = (INSIDE ALBEDO, OUTSIDE ALBEDO)

FOOTPRINT = CIRCULAR WITH 30 METER RADIUS

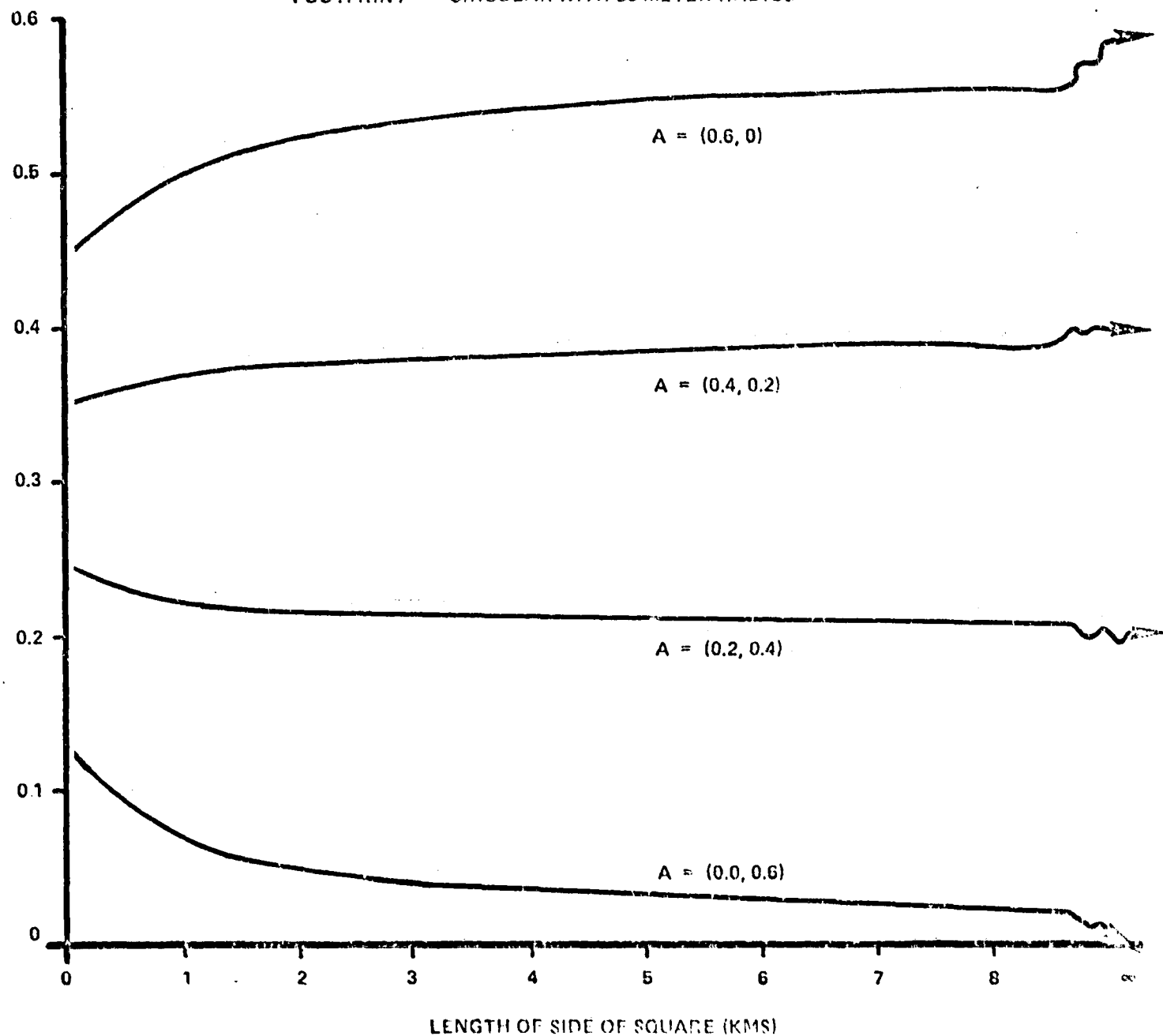


FIGURE 3.10.  
COMPUTED ALBEDO AT CENTER OF SQUARE PATCH

$$\lambda = 0.55 \mu\text{m}$$

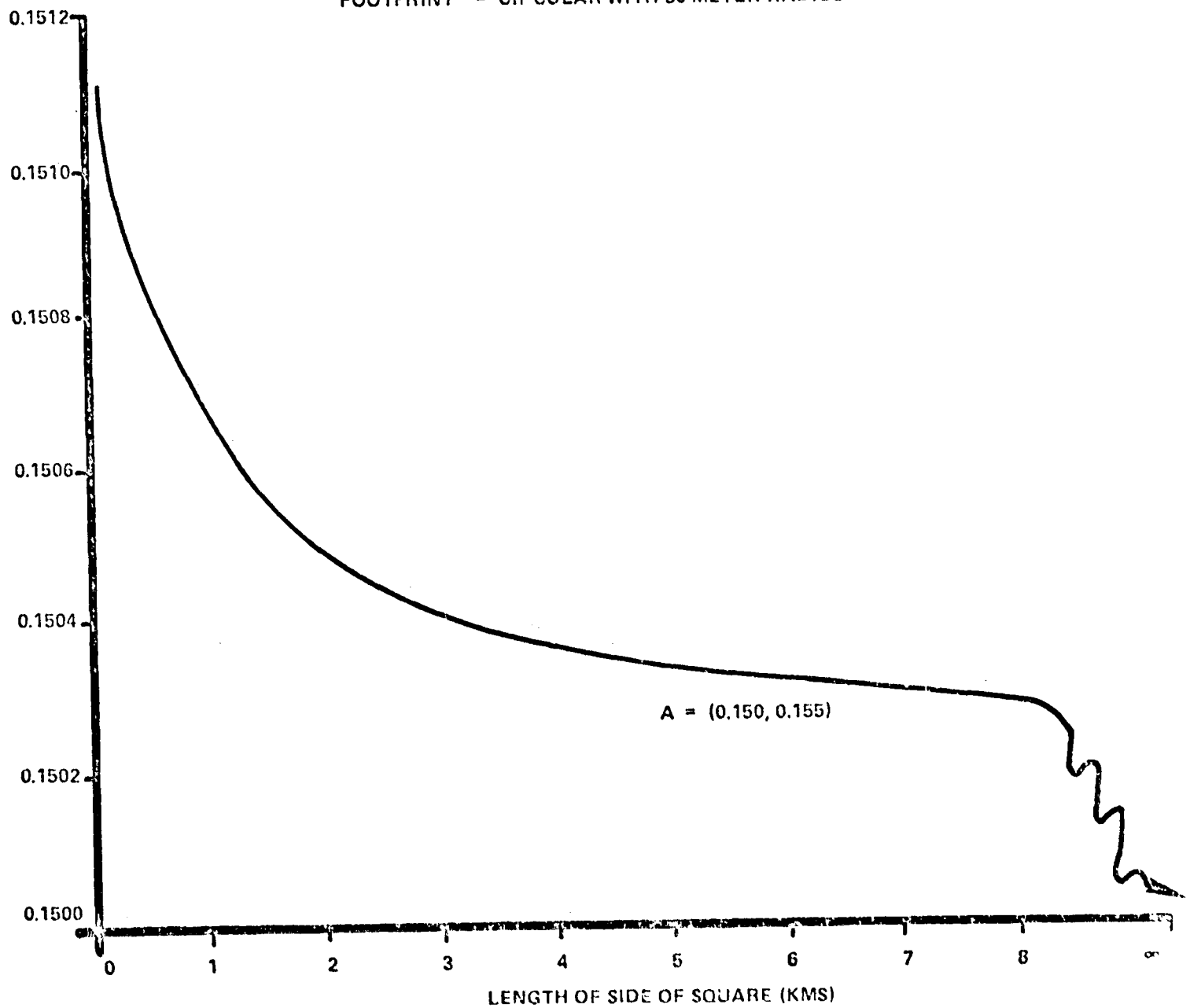
$$\theta_0 = 22^\circ$$

$$\text{TURBIDITY} = 1$$

COMPUTED  
ALBEDO

ALBEDO SET = (INSIDE ALBEDO, OUTSIDE ALBEDO)

FOOTPRINT = CIRCULAR WITH 30 METER RADIUS



## SECTION 4.0

### THEORETICAL CONSIDERATIONS

In order to establish a basic theoretical framework suitable for discussion of the impact of variegated patterns of ground reflectance on sensed intensities, we shall adopt an abstract integral operator formalism. Within this formalism, the multiplication of an intensity by a scattering or transport operator implies integrations over all intermediate physical parameters. We retain explicitly only those parameters which are of immediate interest to the discussion.

#### 4.1 GENERAL FORMALISM

We may formulate our treatment most simply in terms of the following:

- $i_R$  the intensity (or Stokes vector of the light) sensed by the receiver
- $i_s$  the solar intensity incident upon the top of the atmosphere
- $\alpha_{gs}$  The radiation transport operator whose action is to transport radiation from the top of the atmosphere to the ground including all orders of atmospheric scattering (but no ground scattering)  $\equiv e^{-\tau(\mu_0)} + \frac{t(\mu_0)}{\mu_0}$
- $\alpha_{Rg}$  The radiation transport operator whose action is to transport radiation from a point on the ground to the receiver including all orders of atmospheric scattering (but no ground scattering)
- $\alpha_{Rs}$  The radiation transport operator transporting radiation from the sun to the receiver (including all atmospheric, but no ground scattering).

$\alpha_{gg}$  The radiation transport operator whose action is to transport radiation from one point on the ground back to the ground including all orders of intermediate atmospheric scattering but no intermediate interactions with the ground.

$g$  The ground reflectance operator which reflects radiance from the ground and includes absorption at the ground (proportional to the albedo for Lambertian surfaces)

Thus, we may write the intensity at the receiver in terms of contributions from light which has suffered zero, one, two, three, ... interactions with the ground:

$$i_R = \alpha_{Rs} i_s + \alpha_{Rg} g \alpha_{gs} i_s + \alpha_{Rg} g \alpha_{gg} g \alpha_{gs} i_s + \alpha_{Rg} g \alpha_{gg} g \alpha_{gg} g \alpha_{gs} i_s + \dots \quad (4.1)$$

formally a geometric series in terms of the basic ground interaction. The first term,  $\alpha_{Rs} i_s$  may be identified with the path radiance (denoted by  $I_0$  in the treatment of Section 3). Assuming that the atmosphere is horizontally homogeneous (or relatively so) and that the ground is a Lambertian reflector varying from point to point by its scalar albedo, we may collect together all terms contributing to the illumination incident on the ground at a point  $r'_0$  and write them as  $I(r'_0)$ :

$$i_R = \alpha_{Rs} i_s + \int \alpha_{Rg} (\underline{r}_0 - \underline{r}'_0) g(\underline{r}'_0) I(\underline{r}'_0) d\underline{r}'_0 \quad (4.2)$$

The separable angular dependence of Lambertian reflectance has permitted implicit integration over angles; thus,  $l(\underline{r}'_0)$  is, in fact, the flux incident on the ground at  $\underline{r}'_0$ .

The argument of  $\alpha_{Rg}$  indicates that its action is to transport light which has been reflected from the ground at the point  $\underline{r}'_0$  into the receiver which is aimed at a point  $\underline{r}_0$  on the ground (assuming, for the moment, that the field of view of the receiver is infinitesimal). Equation 4.2 has the form of a convolution and  $\alpha_{Rg}$  acts as a spread function.

Under the Lambertian ground reflectance assumption,  $I(\underline{r}_0)$  may be obtained from the solution of a linear integral equation with a kernel of the polar form:

$$I(\underline{r}_0) = \alpha_{gs} i_s + \int d\underline{r}'_0 \alpha_{gg}(|\underline{r}_0 - \underline{r}'_0|) g(\underline{r}'_0) I(\underline{r}'_0) \quad (4.3)$$

For illustration, it is useful to examine the special case of a ground plane whose Lambertian albedo is uniform over the whole plane. In this case,  $g(\underline{r}_0) = g$  is constant as is  $I(\underline{r}_0)$  so that

$$I = \frac{\alpha_{gs} i_s}{1 - gS} \quad (4.4)$$

where  $S = \int d\underline{r}'_0 \alpha_{gg}(|\underline{r}_0 - \underline{r}'_0|)$  is the probability that a photon emanating from the ground will return to the ground. Inserting equation 4.4 into 4.2 yields

$$i_R = \alpha_{Rs} i_s + \frac{\int \alpha_{Rg}(\underline{r}_0 - \underline{r}'_0) g \alpha_{gs} i_s d\underline{r}'_0}{1 - gS} \quad (4.5)$$

which has the form of equation 3.2:

$$I = I_o + \frac{TA}{1 - SA} \quad (4.6)$$

with the correspondences  $T \sim \int \alpha_{Rg}(r_o - r'_o) \alpha_{gs} i_s dr'_o$

$$A \sim g$$

$$I_o \sim \alpha_{Rs} i_s$$

$$I \sim i_R$$

Returning to equation 4.3, if the spatial variations in the ground reflectance,  $g(r_o)$  are rapid with respect to the range of the ground-to-ground spread function  $\alpha_{gg}(r_o - r'_o)$  or if the variations in ground albedo are small (low contrast ground patterns), we may obtain  $I$  approximately from

$$I(\underline{r}_o) = \frac{\alpha_{gs} i_s}{1 - S \bar{A}(\underline{r}_o)} \quad (4.7)$$

$$\text{where } \bar{A}(\underline{r}_o) = \frac{\int d\underline{r}'_o \alpha_{gg}(|\underline{r}_o - \underline{r}'_o|) g(\underline{r}'_o)}{\int d\underline{r}'_o \alpha_{gg}(|\underline{r}_o - \underline{r}'_o|)} \quad (4.8)$$

is the local ground albedo averaged over the range of the spread function  $\alpha_{gg}$  and

$$S = \int d\underline{r}'_o \alpha_{gg}(|\underline{r}_o - \underline{r}'_o|) \quad (4.9)$$

is the probability that a photon emitted from the ground will return to the ground.

The fundamental importance of equation 4.2 rests upon the fact that it has the form of a convolution. This permits us to find a solution for the product  $g(r_o)I(r_o)$  by taking advantage

ORIGINAL PAGE IS  
OF POOR QUALITY



of the Faltung theorem from Fourier analysis. Let  $F$  represent the Fourier transform operator and  $F^{-1}$  its inverse. For a suitable function  $u(x)$  the Fourier transform is (in one dimension)

$$F(u) = U(v) = \int_{-\infty}^{\infty} u(x) e^{2\pi i v x} dx$$

and its inverse is

$$u(x) = F^{-1}(U) = \int_{-\infty}^{\infty} e^{-2\pi i v x} U(v) dv$$

If

$$s(x) = \int_{-\infty}^{\infty} u(y) v(x-y) dy$$

then

$$F(s) = F(u) F(v)$$

so that

$$F(u) = \frac{F(s)}{F(v)}$$

or

$$u(x) = F^{-1} \left[ \frac{F(s)}{F(v)} \right]$$

Applying the Faltung theorem to equation 4.2, we obtain

$$I(\underline{r}) g(\underline{r}) = F^{-1} \left[ \frac{F(i_R^{-\alpha} R_s i_s)}{F(\alpha_{Rg})} \right] \quad (4.10)$$

where now  $F$  represents a two-dimensional Fourier transform.

Thus knowledge of the point spread function  $\alpha_{Rg}$ , the path radiance  $\alpha_{Rs}$   $i_s$  and the illumination of the ground,  $I$  permits the ground albedo pattern to be obtained through Fourier deconvolution.

#### 4.2 SPREAD FUNCTIONS AND MODULATION TRANSFER FUNCTIONS

If the  <sup>$A \ll 1$</sup>  albedo is low or if the  <sup>$S \ll 1$</sup>  atmosphere is not optically thick, the major function affecting satellite observations of the earth is the atmospheric spread function. From a modeling viewpoint the point spread function  $\alpha_{Rg}$  is difficult to assess, but a function closely related to it, the line spread function is relatively amenable to computation. The point spread function is essentially the response at the receiver to a single point at the ground (after subtracting the pure atmospheric scattering). The line spread function, similarly, is the response to a line on the ground. Denoting the point spread function by  $\alpha_p$ , the line spread function,  $\alpha_L$ , is obtained as an integral:

neglect  
 $\frac{1}{1-A\bar{S}}$  factor  
interaction  
between  
atmos and  
etc.

$$\alpha_L(x) = \int_{-\infty}^{\infty} \frac{2\rho \, d\rho \, \alpha_p(\rho)}{\sqrt{\rho^2 - x^2}} = \int_{-\infty}^{\infty} \alpha_p(\sqrt{x^2 + y^2}) \, dy \quad (4.11)$$

We have assumed, then, that the point spread function is azimuthally symmetric. This will be the case when the receiver is pointed towards the nadir and the atmosphere is horizontally homogeneous. Away from nadir, azimuthal symmetry will obtain approximately if the receiver field of view is sufficiently small. Assuming azimuthal symmetry, the point spread function may be obtained from the line spread function by solving equation 4.11 as an integral equation. The result is

$$\alpha_p(r) = -\frac{1}{2\pi r} \frac{d}{dr} \int_r^{\infty} \frac{\alpha_L(x)}{\sqrt{x^2 - r^2}} 2x \, dx \quad (4.12)$$

This is useful because the line spread function may be obtained in a straightforward way through modeling.

If the ground-to-ground spread function  $\alpha_{gg}$  is small (optically thin atmospheres) or if the ground albedo pattern changes rapidly with respect to  $\alpha_{gg}$ , then the illumination of the ground will be approximately constant. Under this assumption,  $\alpha_L$ , the line spread function, may be computed from the response to a set of sinusoidal albedo patterns. Let the albedo patterns be of the form (ref. 4)

$$g(x) = b_0 + b_1 \cos 2\pi vx$$

which is illustrated schematically in Figure 4.1. If the illumination of the ground is approximately uniform and equal to  $I$  then the portion of radiation seen by the receiver which comes from the ground is given by

$$i_+ - i_0 = \int_{-\infty}^{\infty} \alpha(x-x') \left\{ b_0 + \frac{b_1}{2} (e^{2\pi i vx'} + e^{-2\pi i vx'}) \right\} I dx'$$

where  $i_0$  is the path radiance.

The difference of these responses at each frequency is therefore proportional to the symmetric part of the Fourier transform of  $\alpha$ . If the receiver points towards the origin, we have

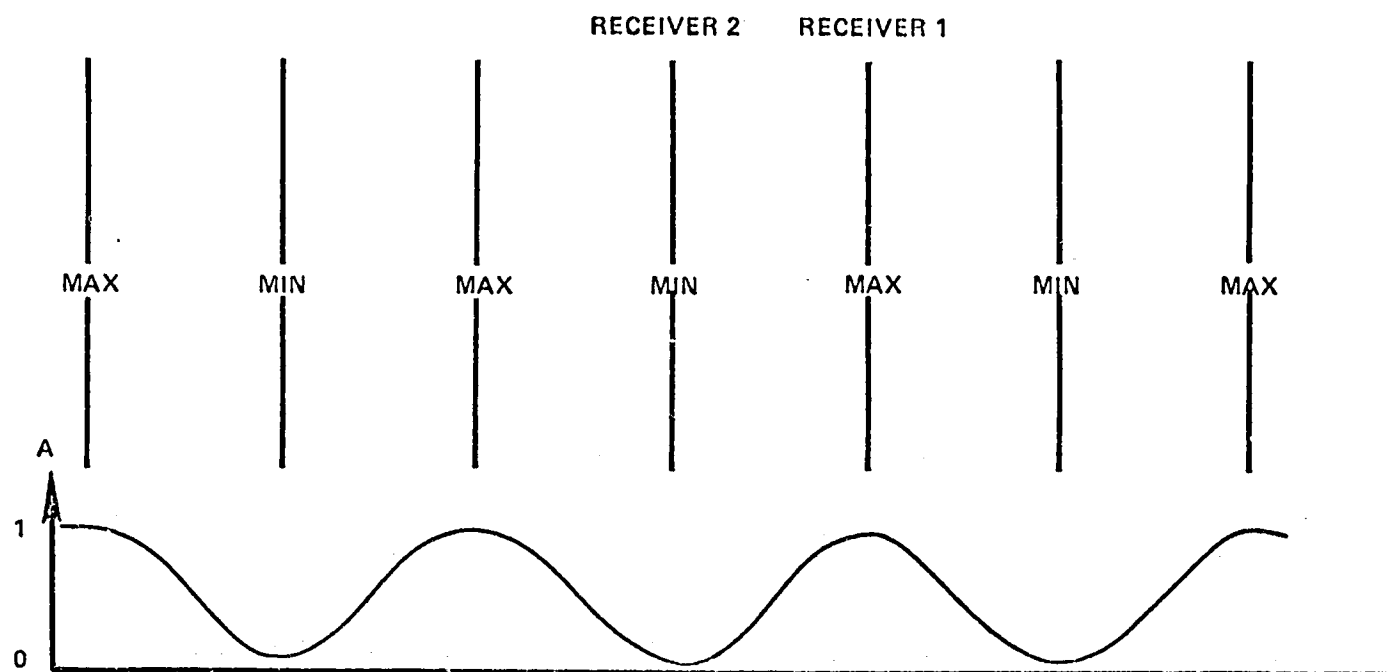
$$\begin{aligned} i_+(0) - i_-(0) &= b_1 \int_{-\infty}^{\infty} \alpha(-x') [e^{2\pi i vx'} + e^{-2\pi i vx'}] I dx' \\ &= b_1 [a(v) + a(-v)] I \end{aligned}$$

with

$$a(v) = \int_{-\infty}^{\infty} e^{-i2\pi vx} \alpha(x) dx$$

ORIGINAL PAGE IS  
OF POOR QUALITY

FIGURE 4.1.  
SCHEMATIC ILLUSTRATION OF REFLECTANCE GEOMETRY 3.:  
SINUSOIDAL PATTERNS



The normalization is obtained from the sum

$$\begin{aligned} i_+(o) + i_-(o) - 2 i_o &= 2b_o \int_{-\infty}^{\infty} \alpha(x') I dx' \\ &= 2b_o a(o) I \end{aligned}$$

Thus, the ratio becomes an estimate of the modulation transfer function (MTF):

$$\frac{b_o}{b_1} \frac{i_+(o) - i_-(o)}{i_+(o) + i_-(o) - 2i_o} \approx \frac{a(v) + a(-v)}{2a(o)} = \text{MTF} \quad (4.13)$$

$$= \frac{a(v)}{a(o)} \quad \text{if } \alpha(x) = \alpha(-x)$$

Figures 4.2 through 4.4 show normalized modulation transfer functions computed for wavelengths  $.47\mu\text{m}$ ,  $.55\mu\text{m}$  and  $1.65\mu\text{m}$  and compare results for turbidities 0, 1, and 3. As may be noted, the MTF is approximately independent of solar zenith angle. The figures also show the component of the MTF contributed by the finite field of view of the receiver which is the MTF for no atmosphere. The system MTF is merely the product of the MTF's of each component in the system; i.e., the total MTF is the product of the MTF for an infinitesimal field of view and the MTF of the field of view. This is illustrated in figure 4.5 which compares the MTF's (computed for the effective albedos) for the field of view, an infinitesimal field of view, and a finite field of view (taken in this case to be circular).

The MTF displays some characteristic features which are worth noting. First, since it is normalized, the MTF approaches 1.0 (or 100%) in the low frequency limit. Secondly, when the field of view is infinitesimal, the MTF approaches a non-zero value or plateau in the high frequency limit. This

FIGURE 4.2.  
INTENSITY MTF VS ALBEDO PATTERN SPATIAL FREQUENCY

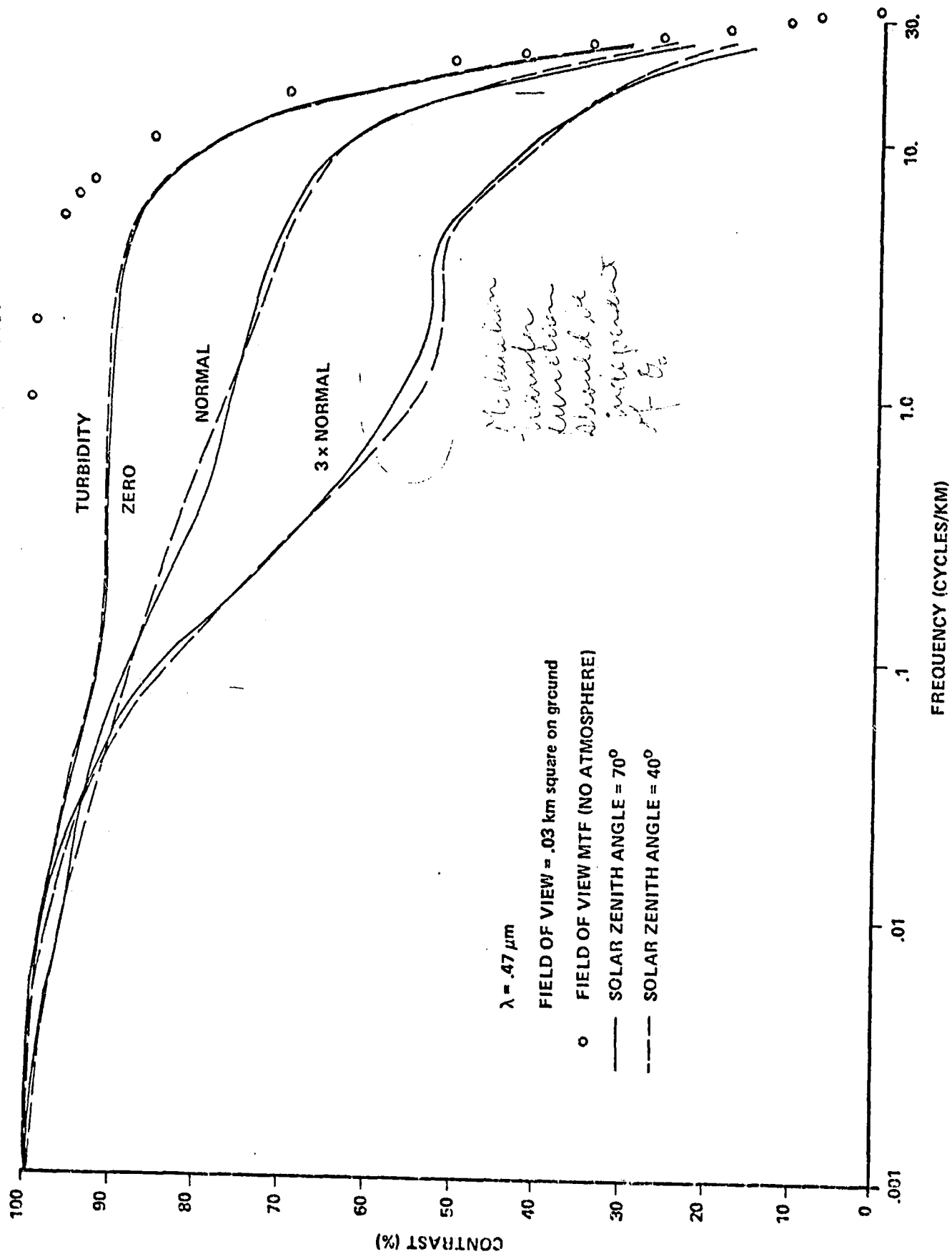


FIGURE 4.3.  
INTENSITY MTF VS ALBEDO PATTERN SPATIAL FREQUENCY

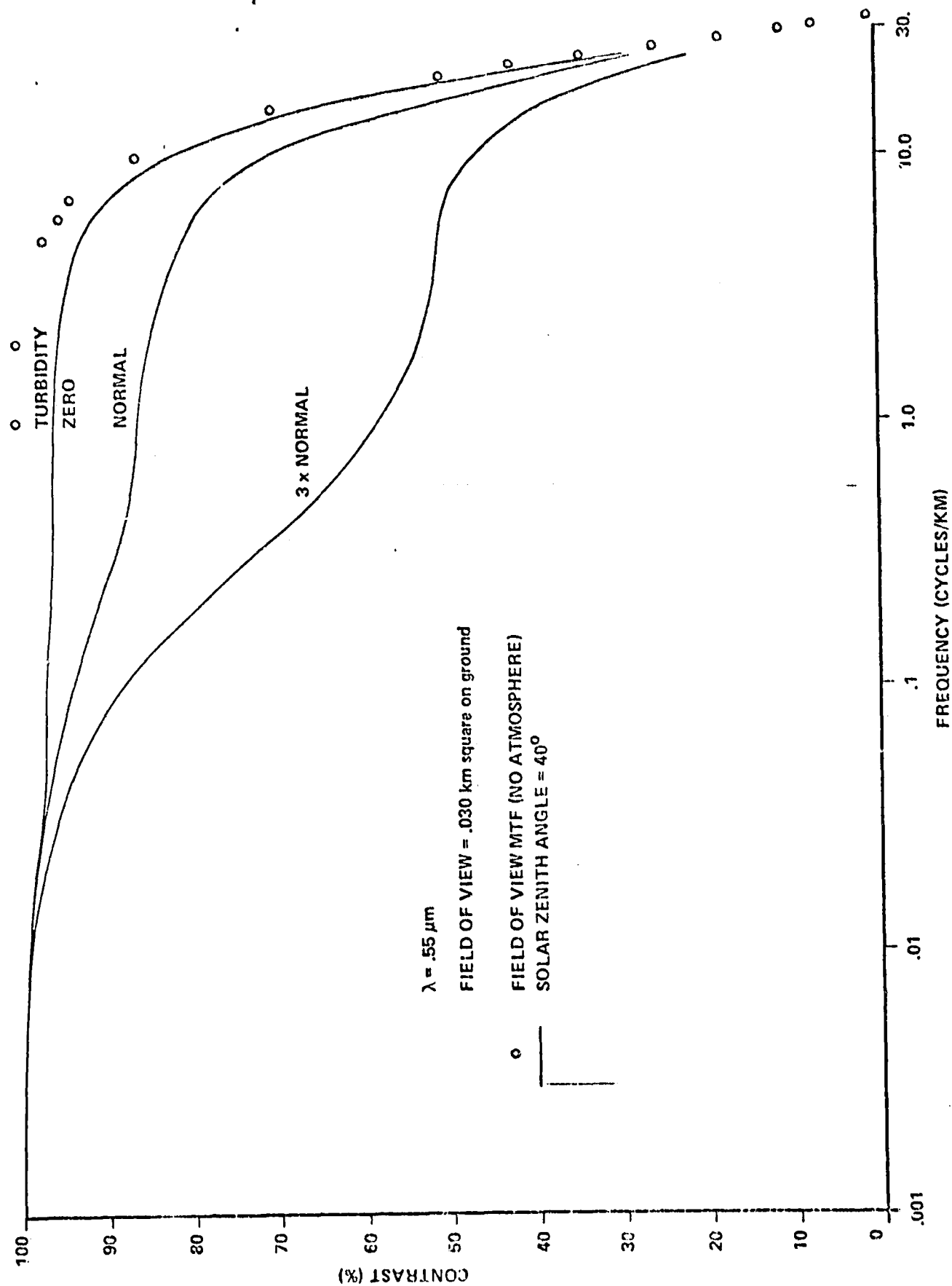


FIGURE 4.4.

INTENSITY MTF VS ALBEDO PATTERN SPATIAL FREQUENCY

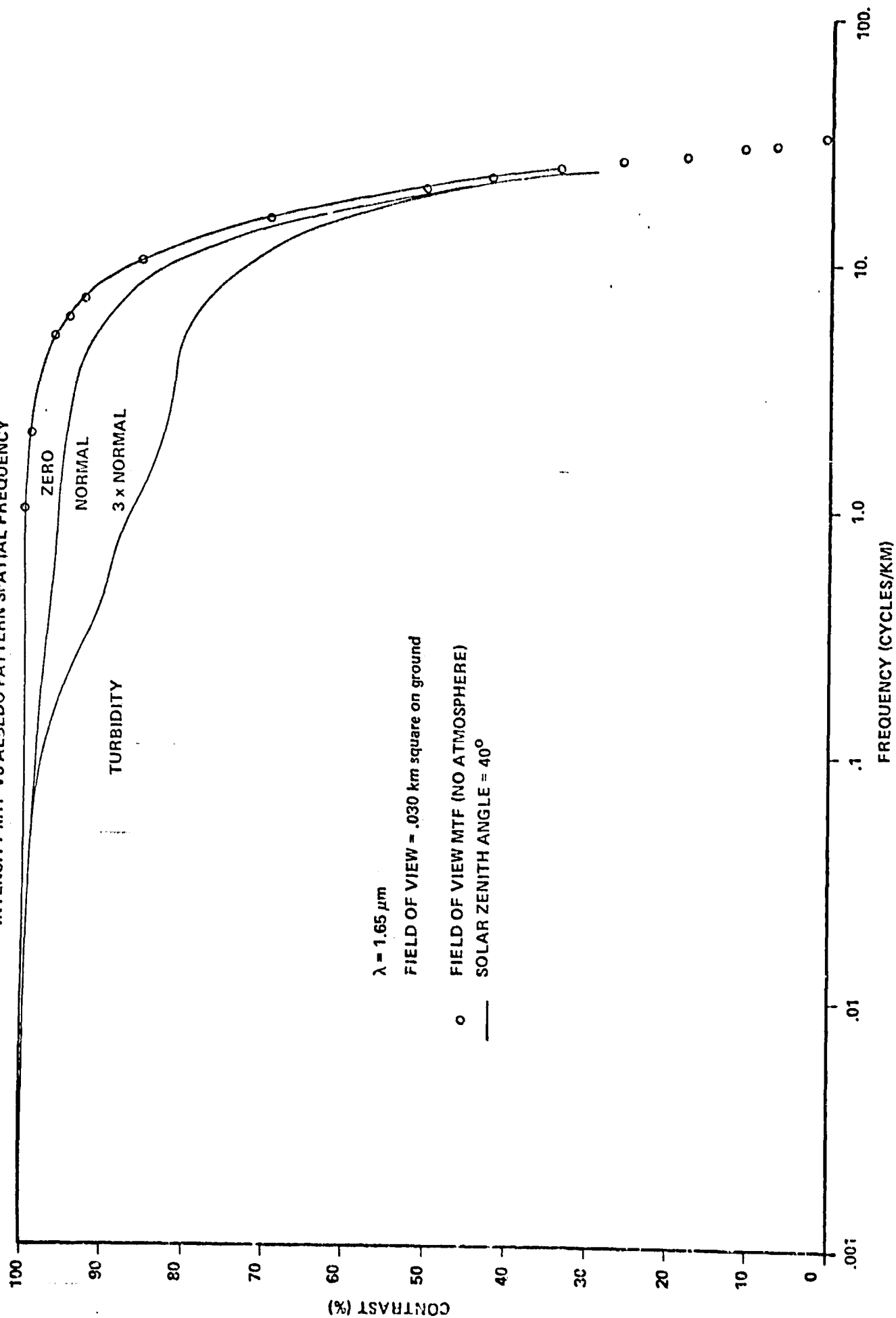
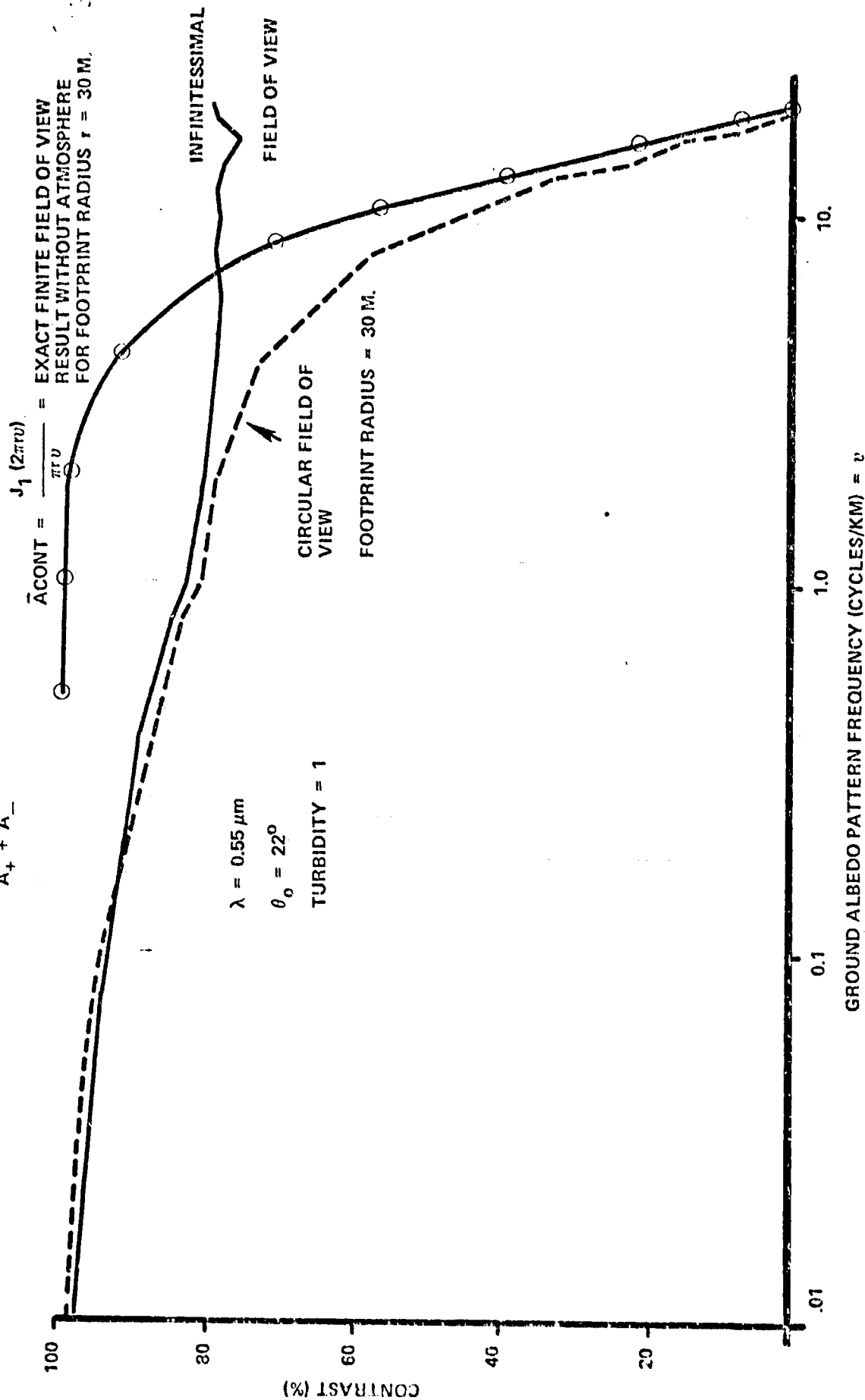




FIGURE 4.5.

EQUIVALENT ALBEDO CONTRAST AS A FUNCTION OF ALBEDO PATTERN FREQUENCY

$$\% \text{ CONTRAST} = \frac{A_+ - A_-}{A_+ + A_-}$$



is due to photons from the ground which reach the receiver without scattering and is reflected in the spread function as a Dirac delta function component. Thirdly, as already pointed out, the effect of the finiteness of the field of view is to fold in a cut-off which becomes dominant at high frequencies (on the order of  $10 \text{ km}^{-1}$  for a 30 m square field of view).

For the purpose of constructing spread functions and modulation transfer functions which correctly incorporate the actual instrumental field of view and sensitivity effects (as measured in bench tests), it is necessary to have the atmospheric MTF computed for an infinitesimal field of view. Figures 4.6 through 4.14 present results for 4000 photon simulations. The roughness of the curves is the result of statistical noise in the computation. Since these curves were plotted automatically, no smoothing has been done. For the purpose of computing reliable spread functions, these curves must be smoothed. This can reliably be accomplished by using a 5 to 7 point running average.

We must emphasize that these computations for infinitesimal fields of view are the most important and most directly useful numerical results of this study. Computed MTF's incorporating finite fields of view depend on the assumptions adopted to model the instrumental sensitivity across the field of view. For example, in our computations utilizing a square field of view, we assumed a sharp sensitivity cut-off at the edge of the FOV. The Thematic Mapper, or any real sensor, however, has a sensitivity which falls off smoothly. For the thematic mapper, the sensitivity decreases to 50% at the pixel edge and in fact extends beyond one pixel. Using the measured instrumental FOV, the full MTF may be constructed (it is simply the product of the two MTFs).

FIGURE 4.6.

INTENSITY MODULATION FUNCTION (MTF)

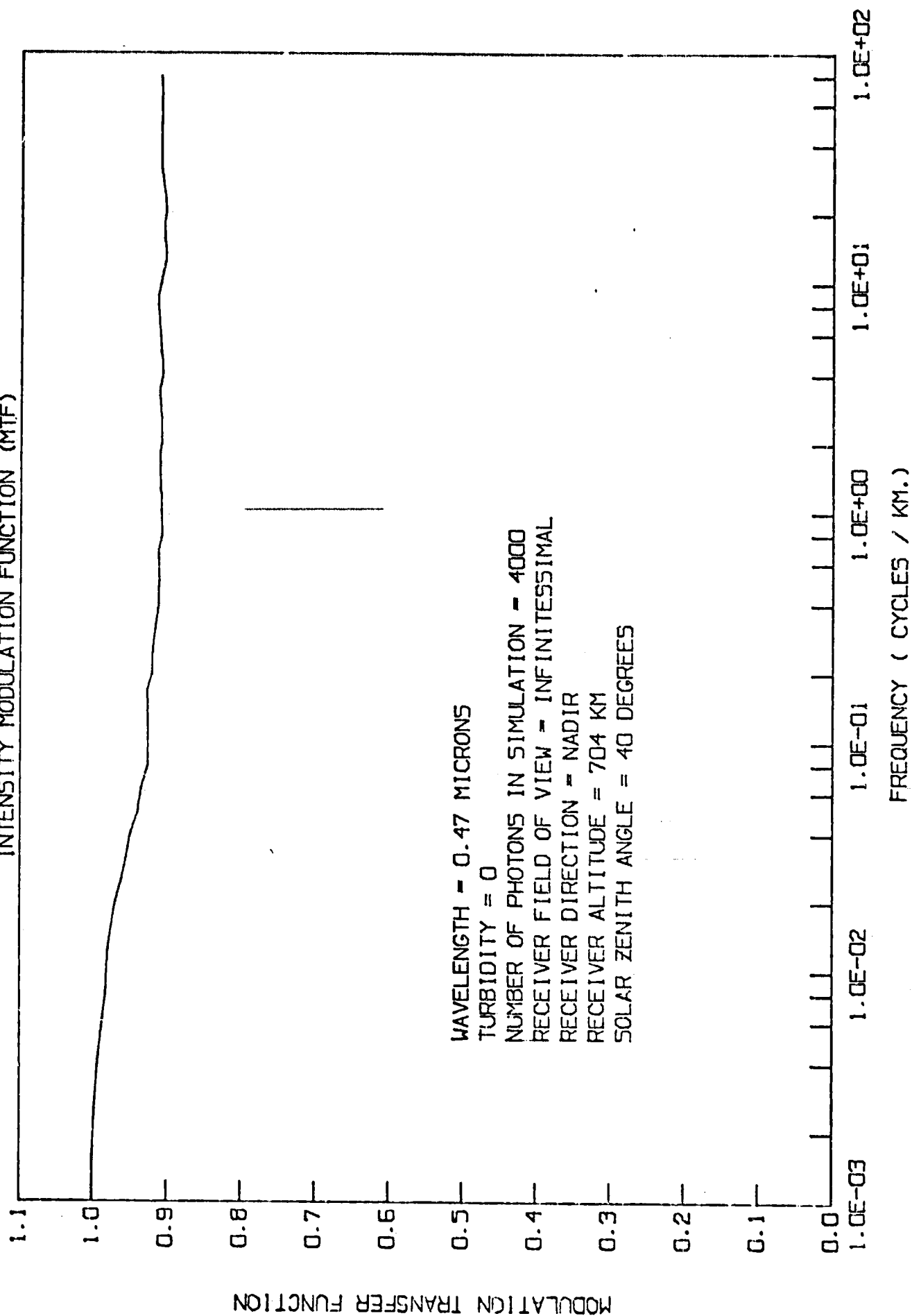
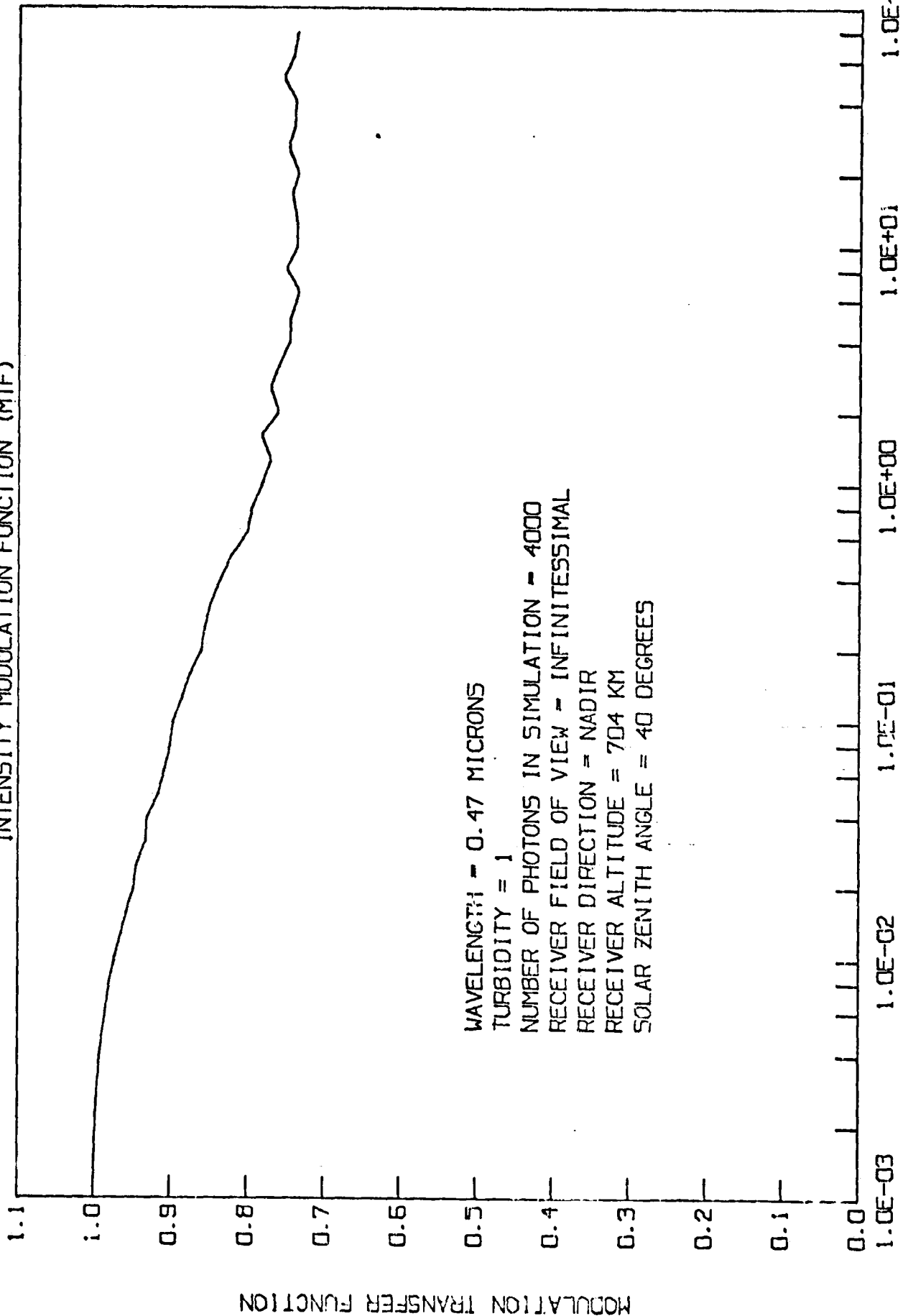


FIGURE 4.7.

INTENSITY MODULATION FUNCTION (MTF)



The point spread function of the atmosphere differs ~~from~~ ~~apart~~ between upward and downward intensity, because of the phase function.

The upward point spread is almost a  $\delta$  function & has all frequencies.

The backward setg is weakly dependent on  $\theta$ .

ORIGINAL PAGE IS  
OF POOR QUALITY

FIGURE 4.8.

INTENSITY MODULATION FUNCTION (MTF)

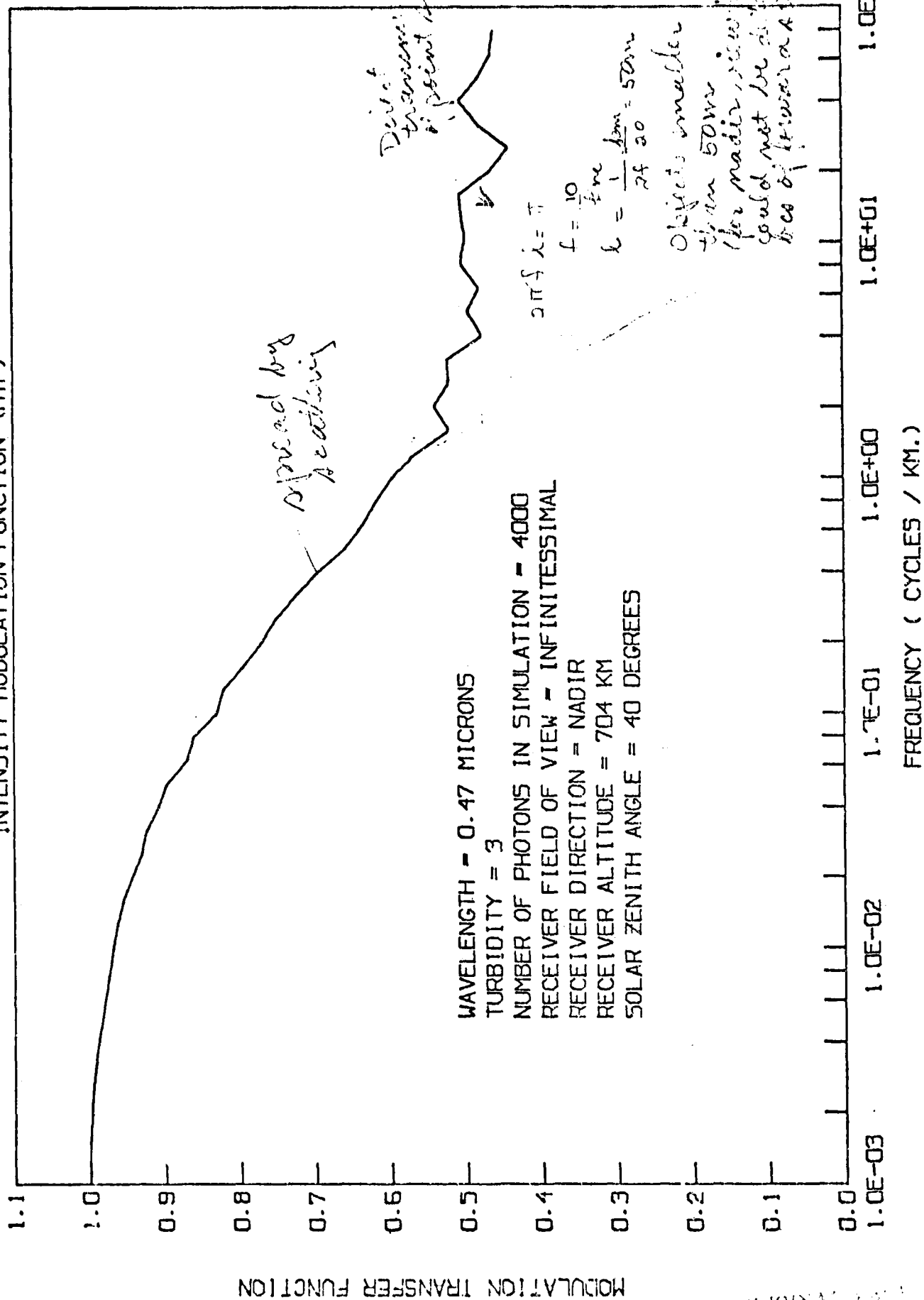


FIGURE 4.9.

INTENSITY MODULATION FUNCTION (MTF)

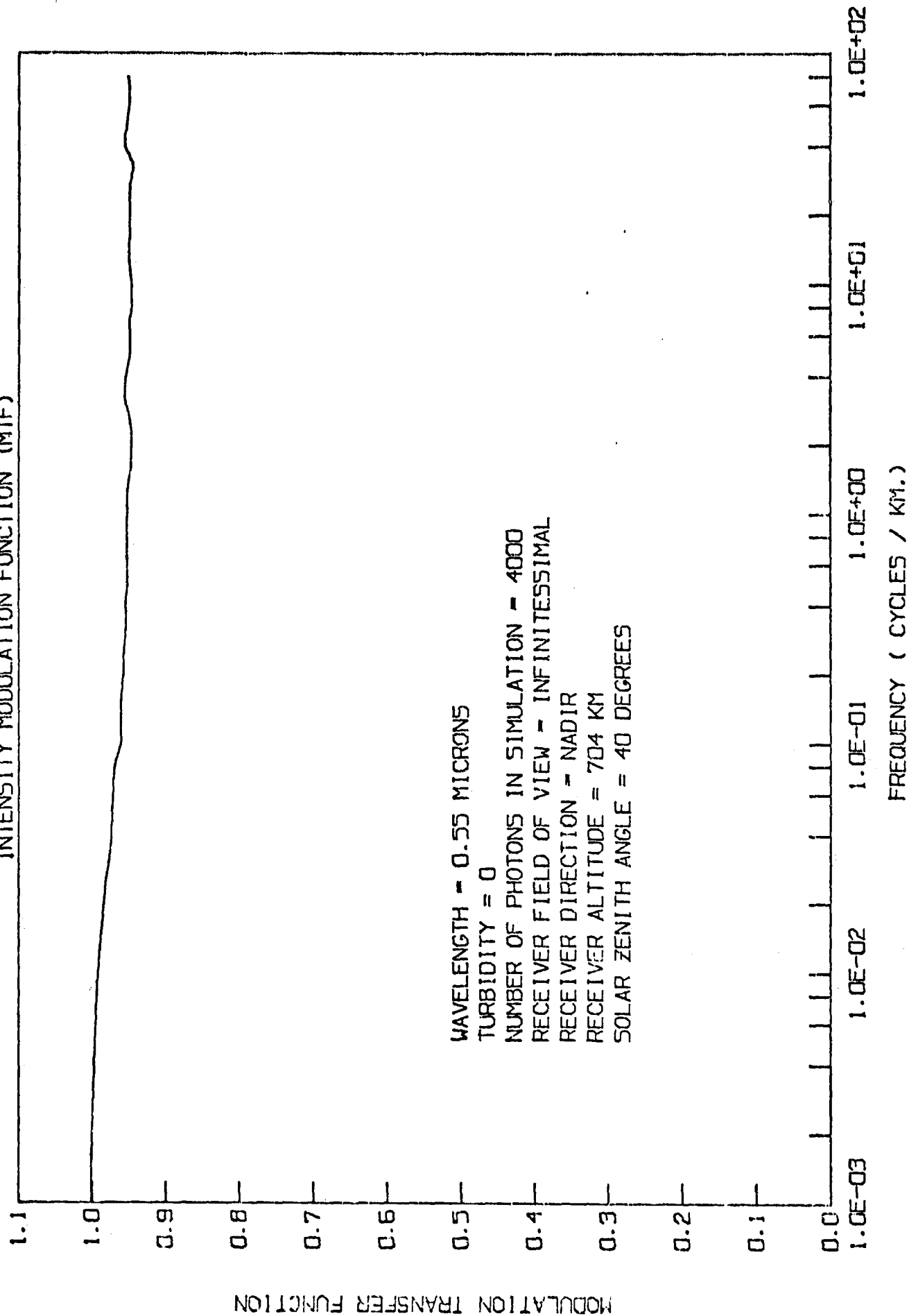


FIGURE 4.10.

INTENSITY MODULATION FUNCTION (MTF)

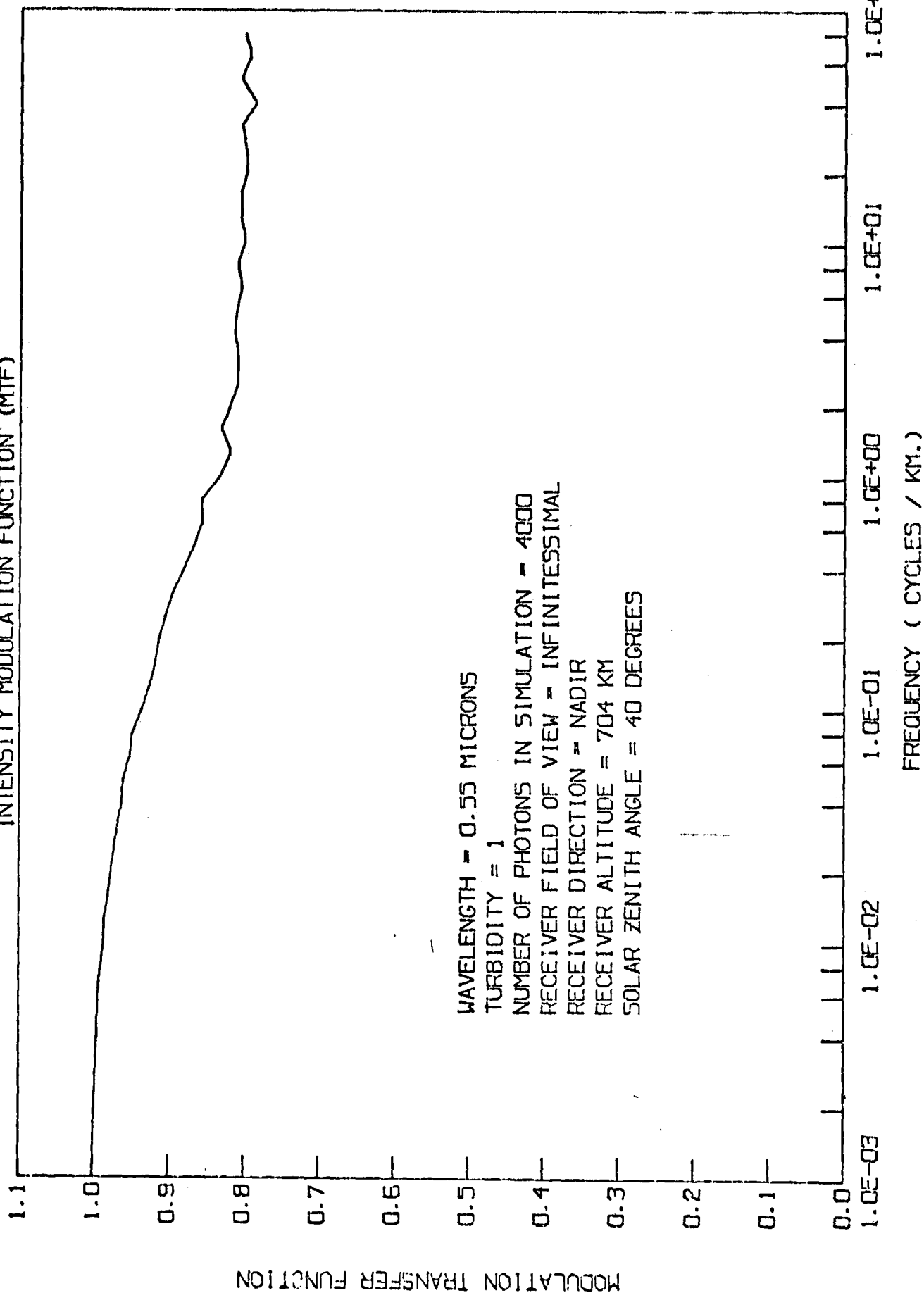




FIGURE 4.11.

INTENSITY MODULATION FUNCTION (MTF)

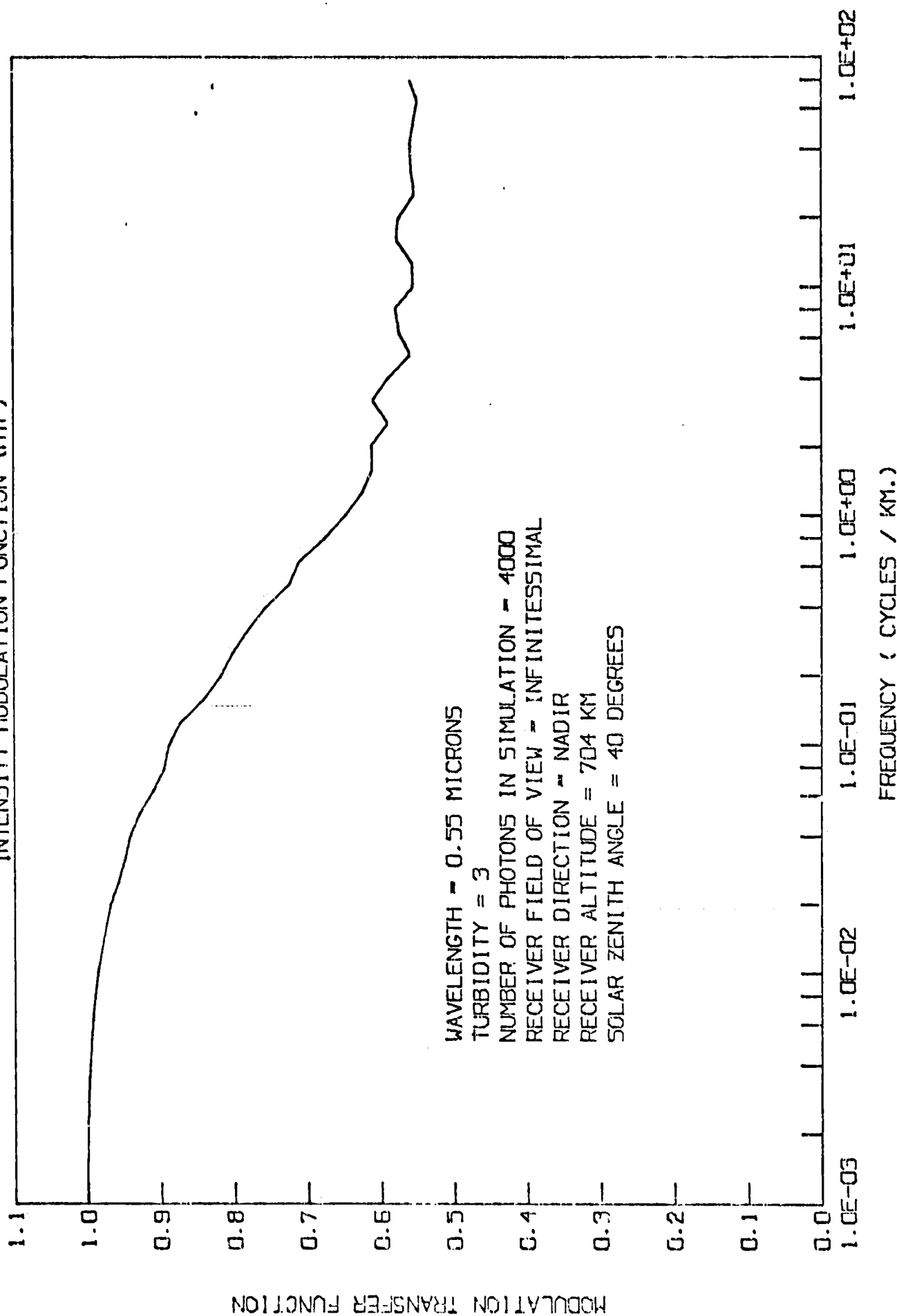
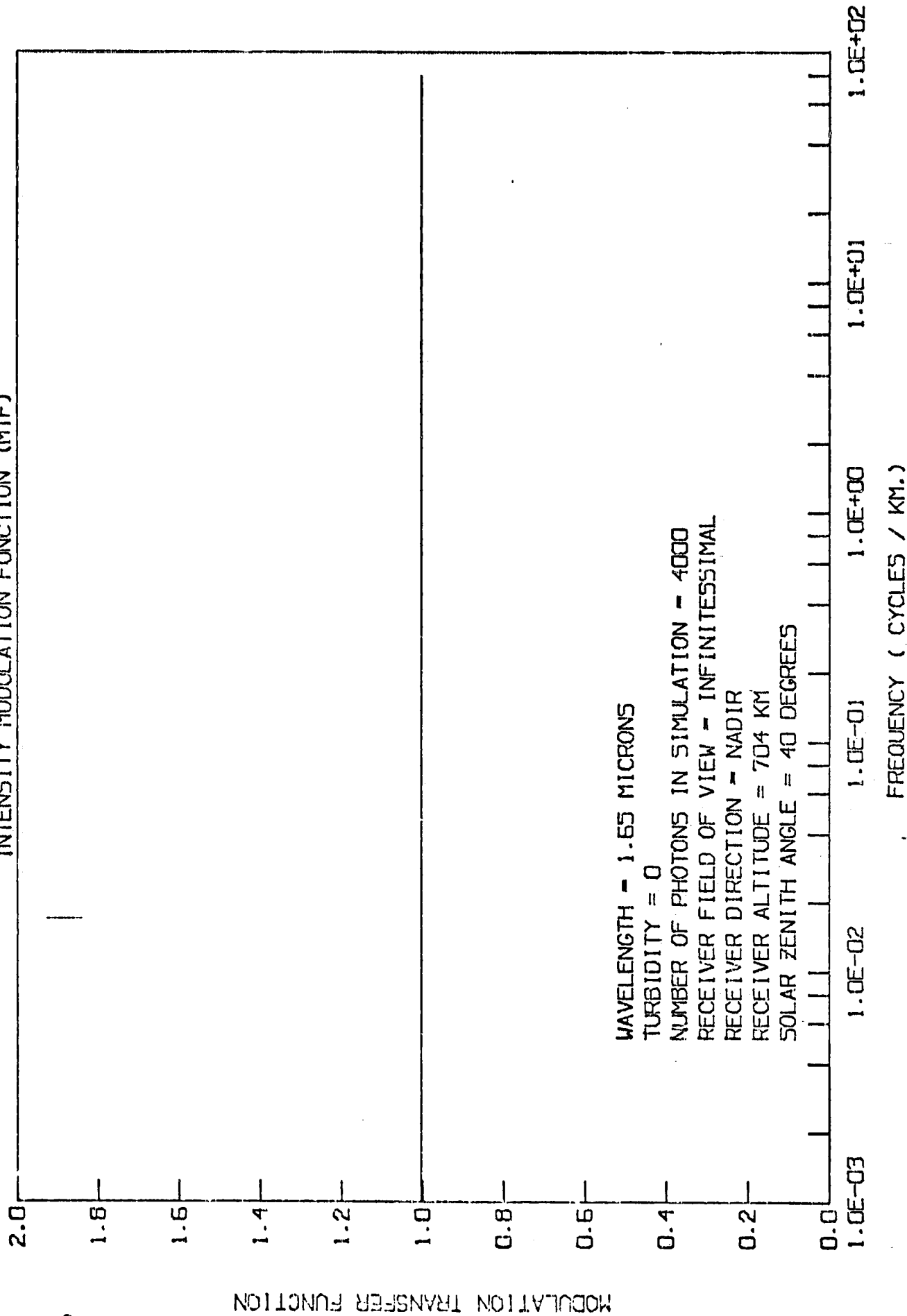


FIGURE 4.12.

INTENSITY MODULATION FUNCTION (MTF)



C-2

FIGURE 4.13.  
INTENSITY MODULATION FUNCTION (MTF)

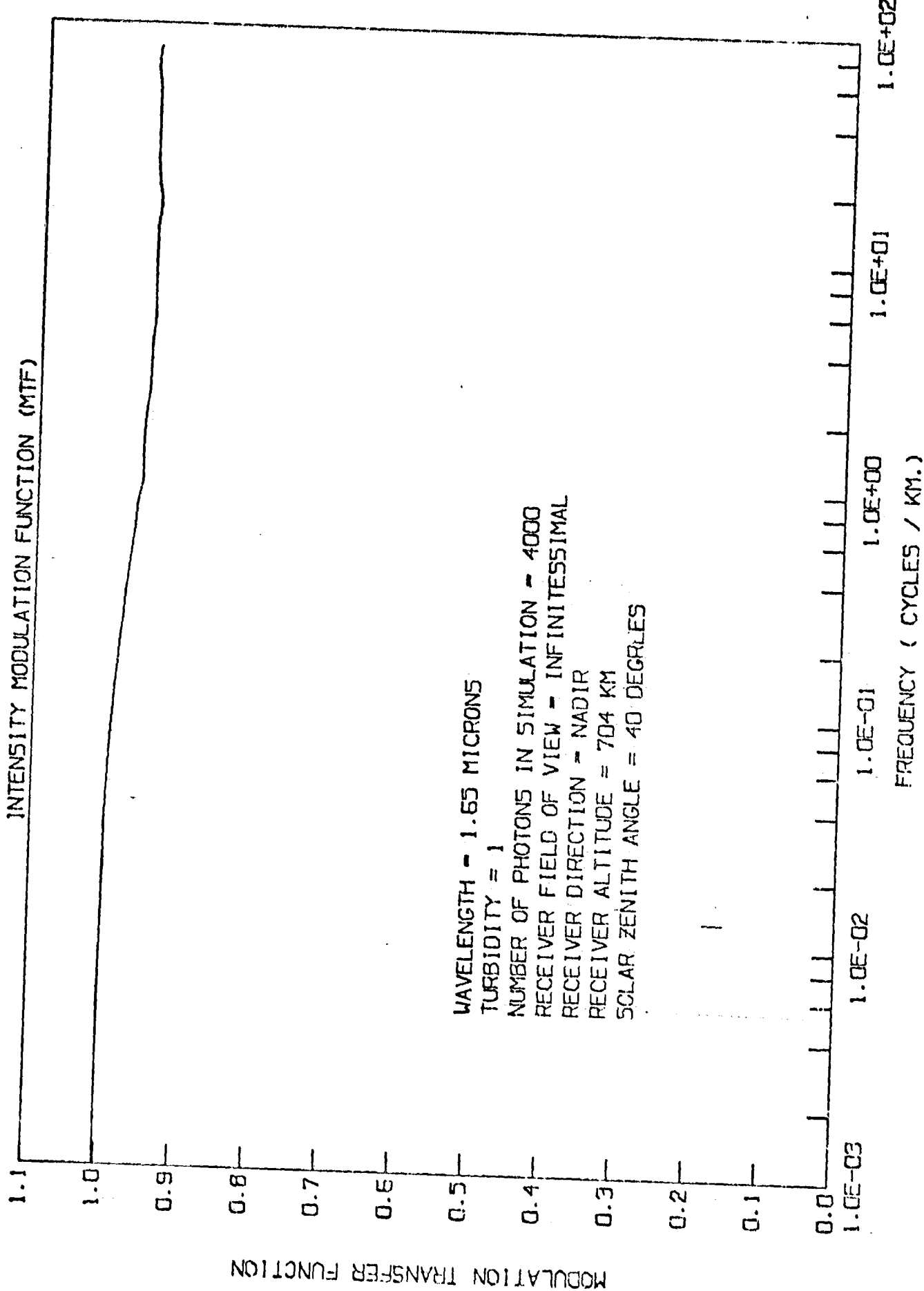
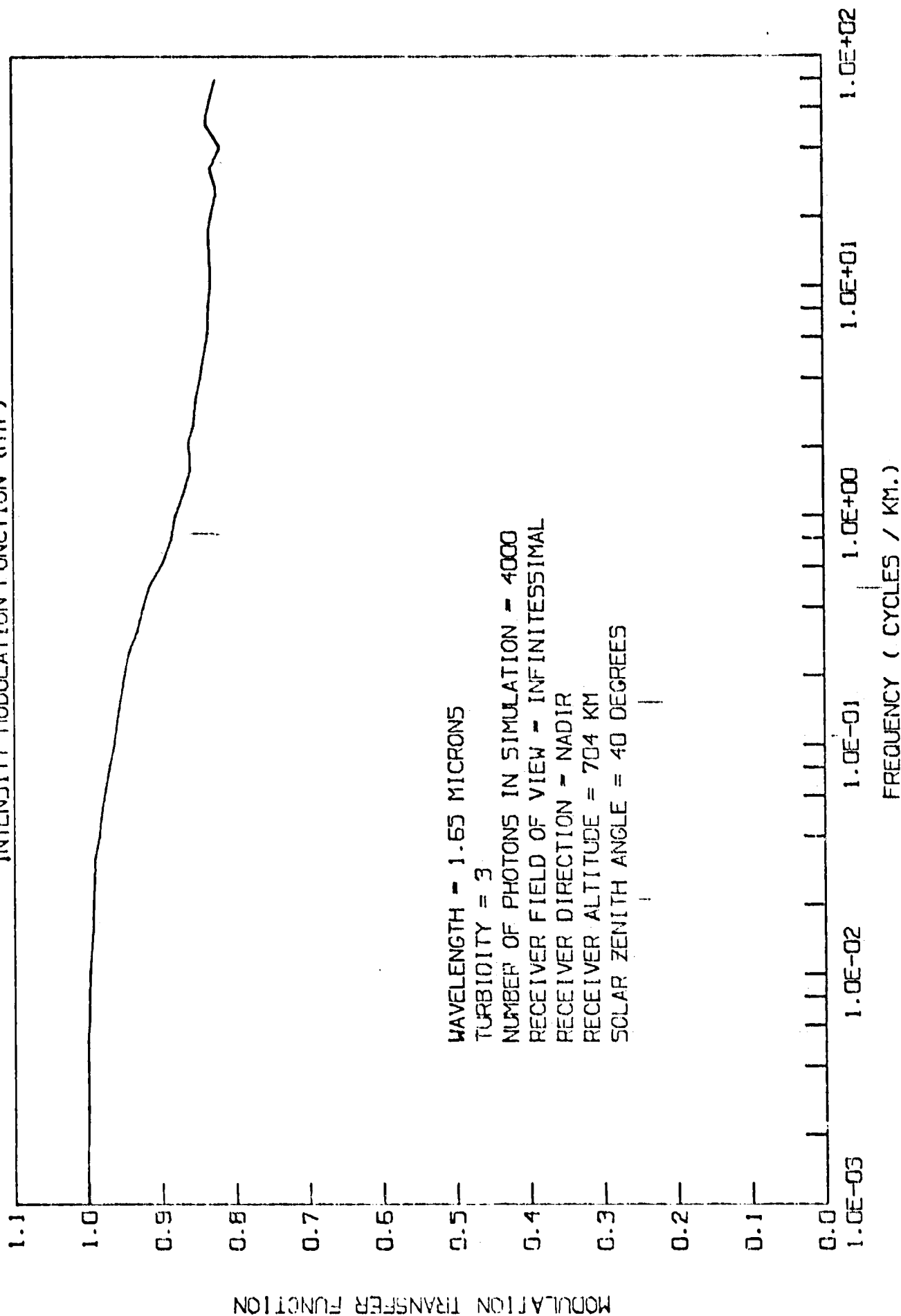


FIGURE 4.14.

INTENSITY MODULATION FUNCTION (MTF)



When the sensed intensity is calibrated in terms of a uniform plane equivalent albedo, the impact of the MTF becomes especially clear. According to the correspondences following equation 4.6, the transmission function  $T$ , is (assuming that the flux illuminating the ground plane is approximately uniform)

$$T \approx \int \alpha(r_o - r'_o) \alpha_{gs} i_s dr'_o = a(o) \alpha_{gs} i_s \quad (4.14)$$

where  $a(o)$  is the zero frequency limit of the Fourier transform of the spread function,  $\alpha$ , and  $\alpha_{gs} i_s$  is the flux incident upon the ground which has not previously interacted with the ground. The effective albedo is given by

$$A^* = \frac{i - i_o}{T + S(i - i_o)} \quad (4.15)$$

$$\begin{aligned} \text{and } i &\approx i_o + \int \alpha(r - r') \frac{g(r') \alpha_{gs} i_s}{1 - S\bar{g}} dr' \\ &= i_o + T \int \frac{\alpha(r - r') - g(r')}{a(o)} \frac{1}{1 - S\bar{g}} dr' \end{aligned} \quad (4.16)$$

where  $\bar{g}$  is the average albedo over the range of the ground-to-ground spread function. Substituting for  $i$  in equation 4.15 yields

$$A^* \approx \frac{\frac{T}{1 - S\bar{g}} \int \frac{\alpha(r - r')}{a(o)} g(r') dr'}{T + S \left[ \frac{T}{1 - S\bar{g}} \int \frac{\alpha(r - r')}{a(o)} g(r') dr' \right]}$$

Multiplication of numerator and denominator by  $\frac{1-S\bar{g}}{T}$  yields

$$A^*(r) \approx \frac{\int \frac{\alpha(r-r')}{a(o)} g(r') dr'}{1+S \int \frac{\alpha(r-r')}{a(o)} (g(r')-\bar{g}) dr'}$$

where we have used  $\int \alpha(r-r') dr' = a(o)$ . If  $S$  is small or if the ground albedo does not vary very much from its average value,  $\bar{g}$ , then the second term in the denominator may be neglected:

$$A^*(r) \approx \int \frac{\alpha(r-r')}{a(o)} g(r') dr' \quad (4.17)$$

Thus the sensed equivalent albedo is the convolution of the true ground albedo pattern  $g(r')$  with the Fourier inverse of the MTF, i.e., with the normalized spread function. This may then be used to obtain an improved estimate of the true ground albedo pattern by deconvolution.

Equation 4.17 demonstrates the chief advantage and main justification for dealing with the equivalent albedo rather than the sensed intensity: effective albedos are very directly related to the true ground albedo through the spread function.

#### 4.3 IMAGE ENHANCEMENT

As we have indicated, accurate knowledge of the spread function can be a most important tool in image enhancement. If the MTF is known, the normalized line spread function may be obtained through Fourier transformation; the point spread function may then be obtained. If the MTF is not known as would be the case for actual data obtained without auxiliary ground truth information, then the spread function may be obtained

approximately by studying the behavior of intensities in the vicinity of sharp albedo boundaries between very large regions. Consider, for example, the simple case of a high contrast boundary between two semi-infinite planes. Let the albedo pattern be the step function

$$\begin{aligned} g(x) &= 0 \quad x < 0 \\ &= 1 \quad x > 0 \end{aligned}$$

The intensity is then approximately

$$I(x) = I_0 + \int_{-\infty}^{\infty} \Lambda(x-y) g(y) \tilde{I} dy$$

where the ground illumination,  $\tilde{I}$ , is taken to be approximately constant (this is not quite true, of course).

$$\frac{dI}{dx} = \frac{d}{dx} \int_{-\infty}^x \Lambda(z) \tilde{I} dz$$

where we have explicitly used the fact that  $g(x)=1$  for  $x>0$  and transformed variables using  $x-y=z$ . We obtain a measure of the spread function, then, from the gradient of  $I$  near the boundary.

$$\frac{dI}{dx} = \Lambda(x) \tilde{I}$$

If the variability of  $I$  is considered, it adds a small term; we get

$$\frac{dI}{dx} = \Lambda(x) \tilde{I}(0) + \int_{-\infty}^x \Lambda(z) \frac{d}{dx} \tilde{I}(x-z) dz$$

If the albedo variation is between  $g_0$  and  $g_1$  rather than 0 and 1, we get (again neglecting variations in the illumination,  $\tilde{I}$ )

$$\frac{dI}{dx} = (g_1 - g_0) \Lambda(x) \tilde{I}$$

Figure 4.15 depicts the line spread functions obtained from the gradient of the intensity versus the boundary of an albedo step function (0., .6) for a wavelength of  $0.55\mu\text{m}$  and the 30 m square IFOV of the thematic mapper. The spread functions for turbidities 0, 1, and 3 are compared. The jitter in the curves is a result of statistical noise. The slight asymmetry, however, is probably real and an expression of the variation in ground illumination across the boundary.

In figure 4.16 we compare line spread functions computed from the gradient across a boundary and from the Fourier transform of the MTF. Here, the field of view is circular, 60 m in diameter since the input to the calculation was taken from some of our earlier work. The asymmetry due to the illumination term is even more evident here.

We have used the spread function (of figure 4.16) computed from the MTF to deconvolve the effective albedo for a step function albedo pattern (0.5, 0.1). The initial effective albedo is compared with both the actual albedo and the result obtained by deconvolution in figure 4.17. Present in the enhanced image is the expected overshoot and undershoot expected from the Gibbs phenomenon associated with the finite spatial bandwidth of the sample and the finite number of Fourier coefficients used in the deconvolution.

In figure 4.18 we compare the error in the unenhanced image with that remaining in the enhanced image. As may be seen, the enhanced image is quite good out to approximately



Let  $f(x) = a + b e^{-ax}$

$$f(0) = a + b = 1$$

$$f'(0) = -a = -0.8$$

$$f'(x) = -a e^{-ax}$$

$$f'(0) = -a = -0.8$$

$$f(x) = a + b e^{-ax}$$

$$f(0) = a + b = 1$$

$$f'(0) = -a = -0.8$$

$$b = 0.2$$

ORIGINAL PAGE IS  
OF POOR QUALITY

Let  $f(x) = a + b e^{-ax}$

$$f(0) = a + b = 1$$

$$f'(0) = -a = -0.8$$

$$f(x) = a + b e^{-ax}$$

$$f(0) = a + b = 1$$

$$f'(0) = -a = -0.8$$

$$f(x) = A e^{-ax} = 20 e^{-27x}$$

$$\Delta(k) = \frac{1}{\pi} \frac{27}{27^2 + k^2}$$

$$\frac{\Delta(27)}{\Delta(0)} = \frac{1}{2}$$

$$k = 27$$

$$2\pi f = 27$$

$$f = \frac{4 \text{ cycles/km}}{\text{if } a = 27}$$

$$\Rightarrow \text{Let } 2\pi f = a$$

$$f = 1 \text{ cycle/km}$$

$$\text{Then } a = 2\pi / \text{km}$$

$$\frac{1}{a} = 0.16 \text{ km, if } f = 1 \text{ cycle/km}$$

Yoram:  
compare Fig 2.3 -  
4.7

Fig. 4.15, p.101  
4.8, p.90  
2.3, p.31

FIGURE 4.15.  
 INTENSITY LINE SPREAD FUNCTION VS. DISTANCE  
 COMPUTED FROM GRADIENT OF STEP FUNCTION ALBEDO PATTERN (0.6, 0.0)

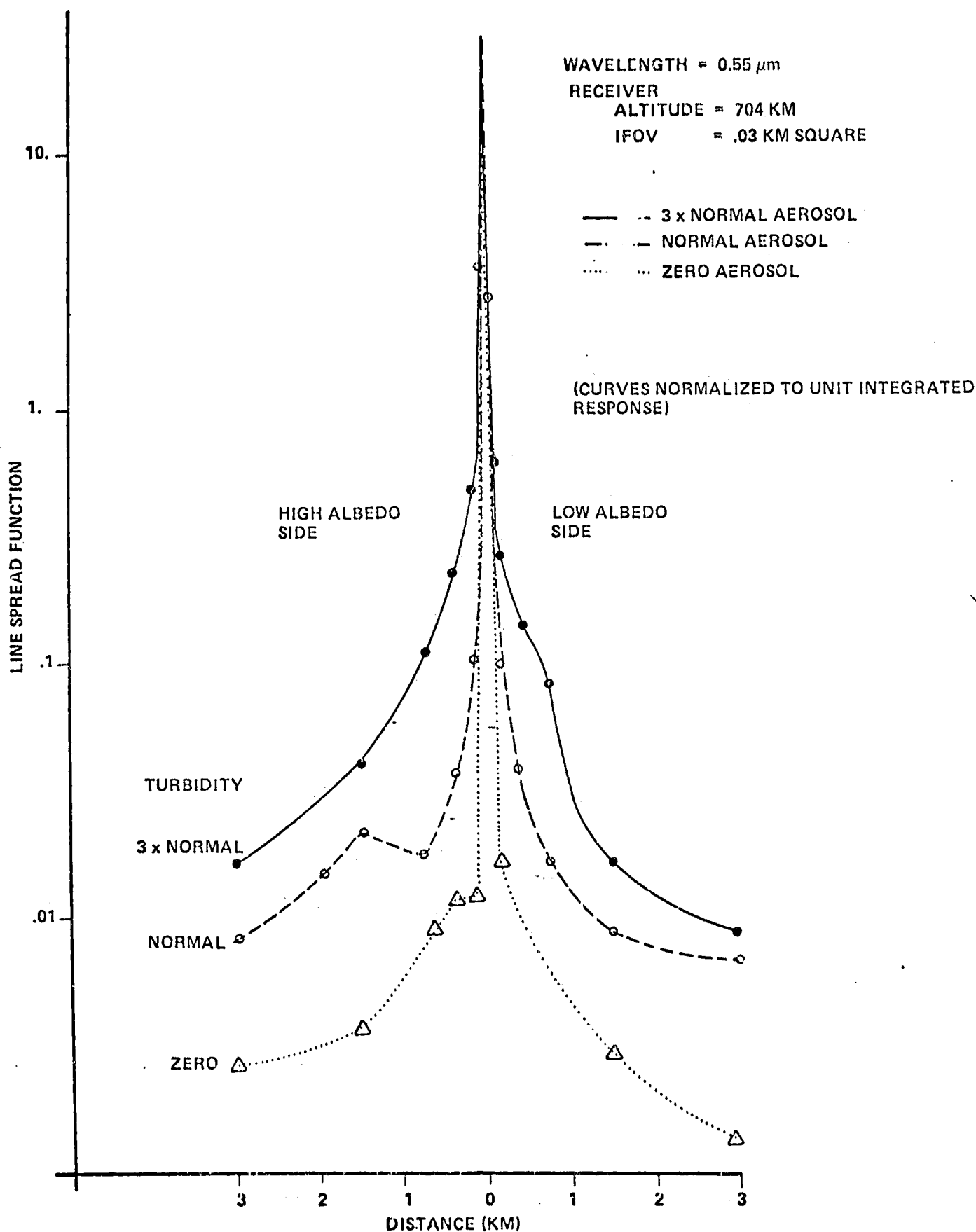


FIGURE 4.15.

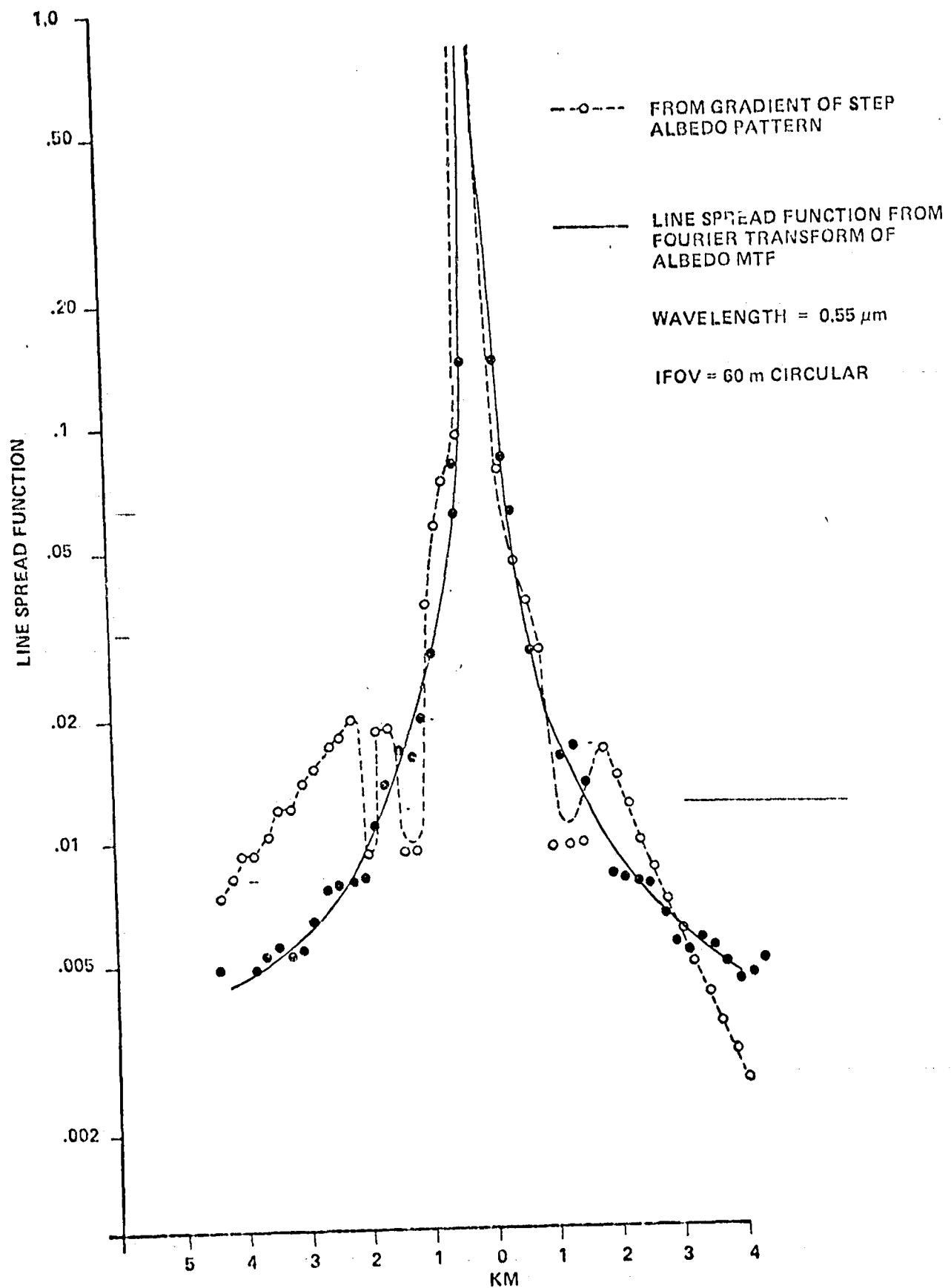


FIGURE 4.17.  
EXAMPLE OF SIMULATED IMAGE ENHANCEMENT

EFFECTIVE ALBEDO FOR STEP FUNCTION  
ALBEDO PATTERN (0.5, 0.1)

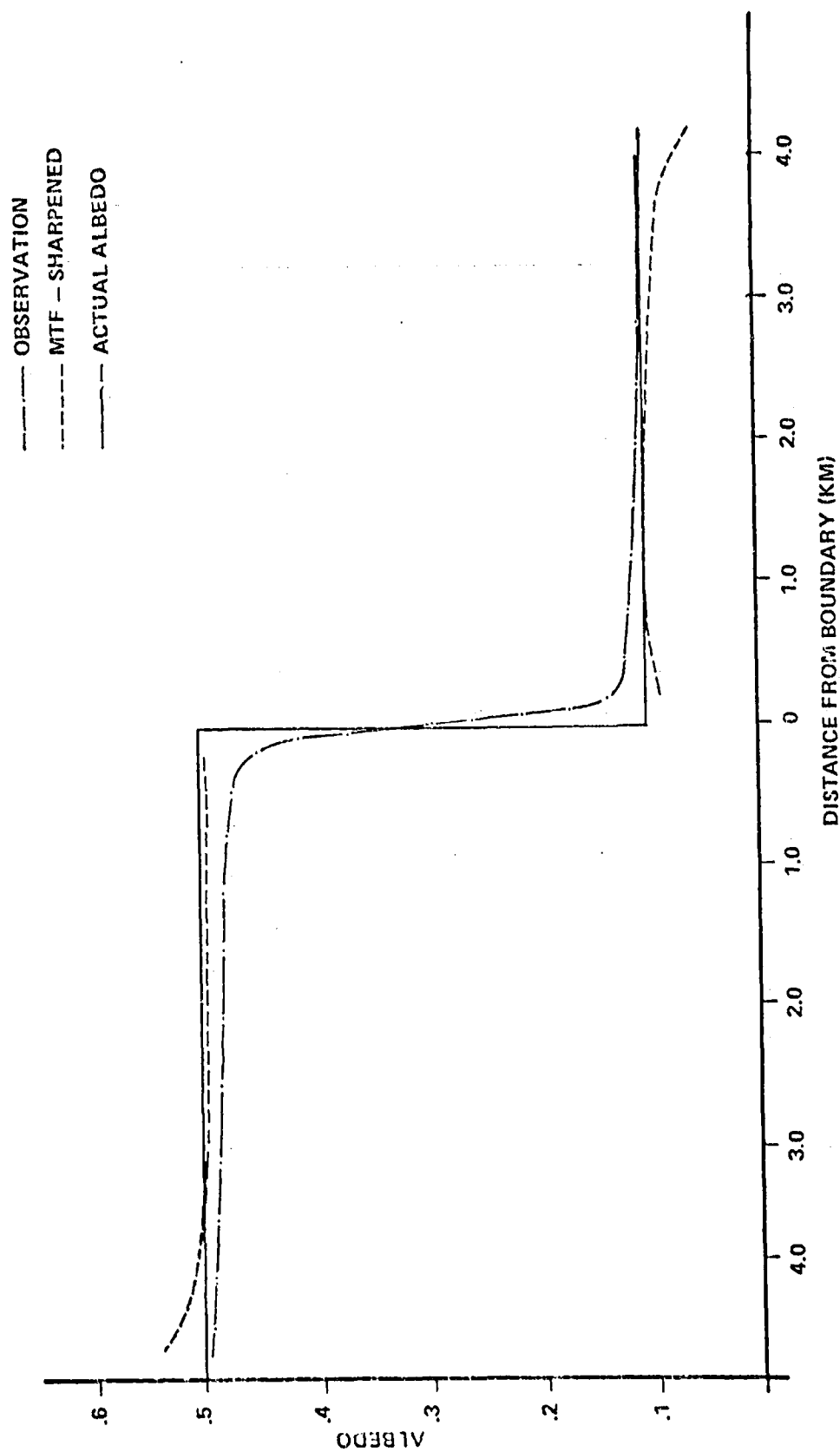
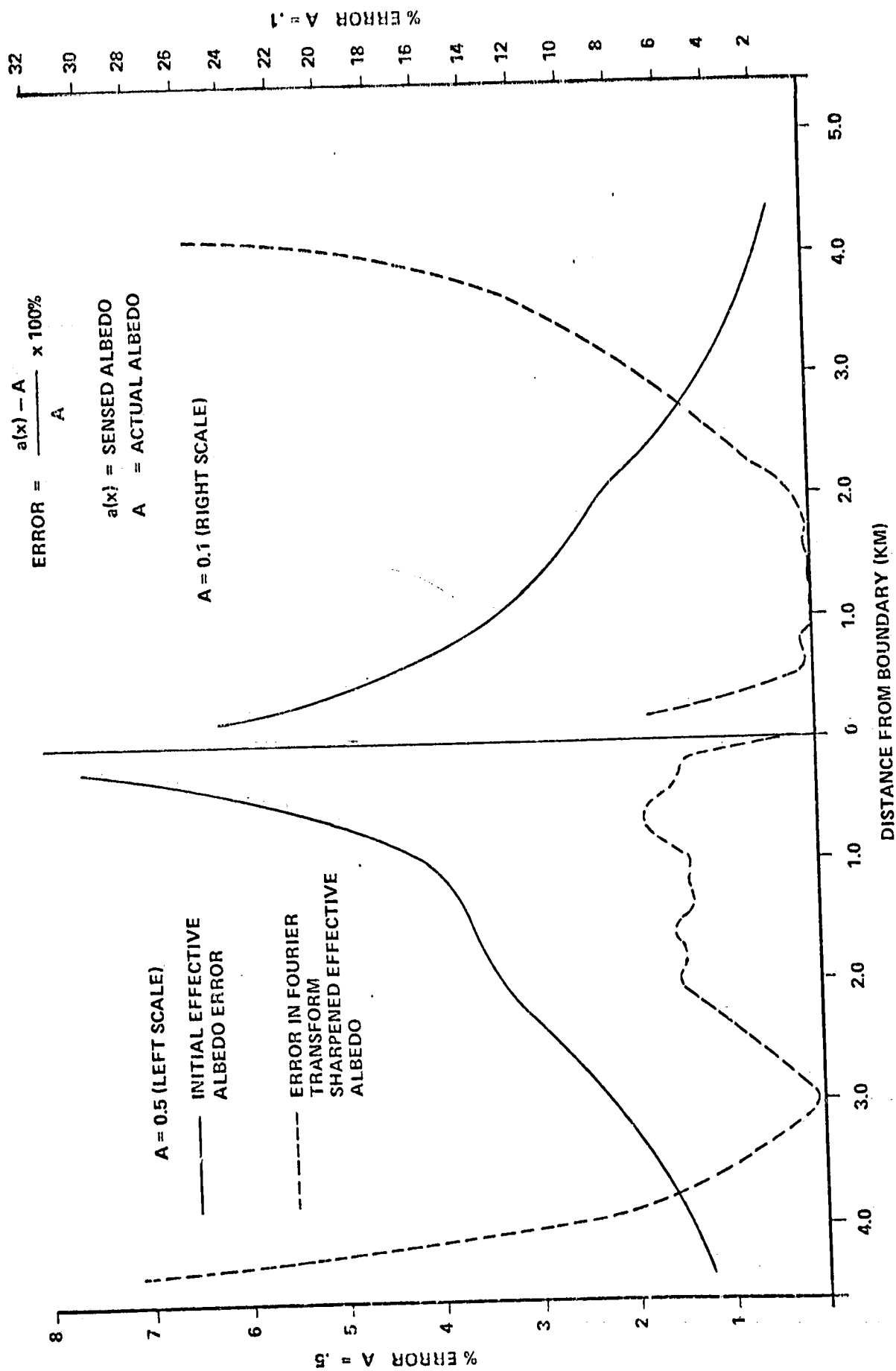


FIGURE 4.18.



2.5 km from the boundary. We might have extended this range had the spread function been computed over a wider region.

We must add some cautionary notes at this stage. First, in order to use a sharp albedo boundary in a Landsat frame to obtain the spread function, the regions on either side of the boundary must be large. As the size of the regions shrinks, the intensity pattern obtained by scanning across the boundary becomes flat nearer the boundary and spread function which would be computed from the gradient becomes narrower with a more pronounced peak, i.e., it deviates from the true spread function. Our calculations for a checkerboard pattern (figures 2.15-2.33) illustrate this effect. If these distorted spread functions are used for deconvolution, more errors will remain in the enhanced image than would be the case had the actual spread function been available. We have not yet evaluated this quantitatively, however.

The second cautionary remark which we must make concerns the possible impact of instrumental noise. If electronic noise is present, the jitter associated with it must be removed before the spread function can be used. One possible scheme for achieving a proper smoothing is to use the noisy spread function to compute the MTF. Then the MTF can be smoothed and used for deconvolution. The smoothing should always be done in the frequency domain since electronic noise will be essentially high frequency noise.

To proceed beyond Fourier deconvolution would require estimates of the spectrum of the noise. In our simulation, noise arises from the statistical jitter inherent in the Monte Carlo simulator. Electronic noise or noise induced by quantization has a different character and is, clearly, instrument dependent. We should point out that a wide variety of alternate image enhancement techniques exist, many of which are discussed in reference 5.

## SECTION 5.0

### THE IMPACT OF ATMOSPHERIC SCATTERING ON CLASSIFICATION

With the capability to evaluate the atmospheric spread function we have acquired the essential tool necessary to estimate quantitatively the impact of atmospheric scattering and ground plane inhomogeneity on the accuracy and adequacy of classification schemes. Our discussion at this point will be heuristic in the sense that the details of a general treatment of classification remain to be worked out. Nevertheless, as we hope to demonstrate, such a theory is within reach and may provide great benefits to the remote sensing field.

At the outset, we recognize the remote sensing classification problem to be best addressed within the general framework of information theory<sup>(6)</sup>. Figure 5.1 illustrates the information flow in remote classification and briefly notes the noise terms attendant at each stage in the process.

Firstly, the ground character belonging to a specified class is itself variable. For example, corn may be green or green and brown or may be wet or dry or be planted densely or sparsely, etc., and yet belong to a class, "corn."

The ground character is then coded by reflection of the incident light. Here we identify the "code" with the spectral reflectance of the ground region. The encoding is disturbed or influenced by the precise character of the ground illumination and the bidirectional reflectance characteristics of the ground region.



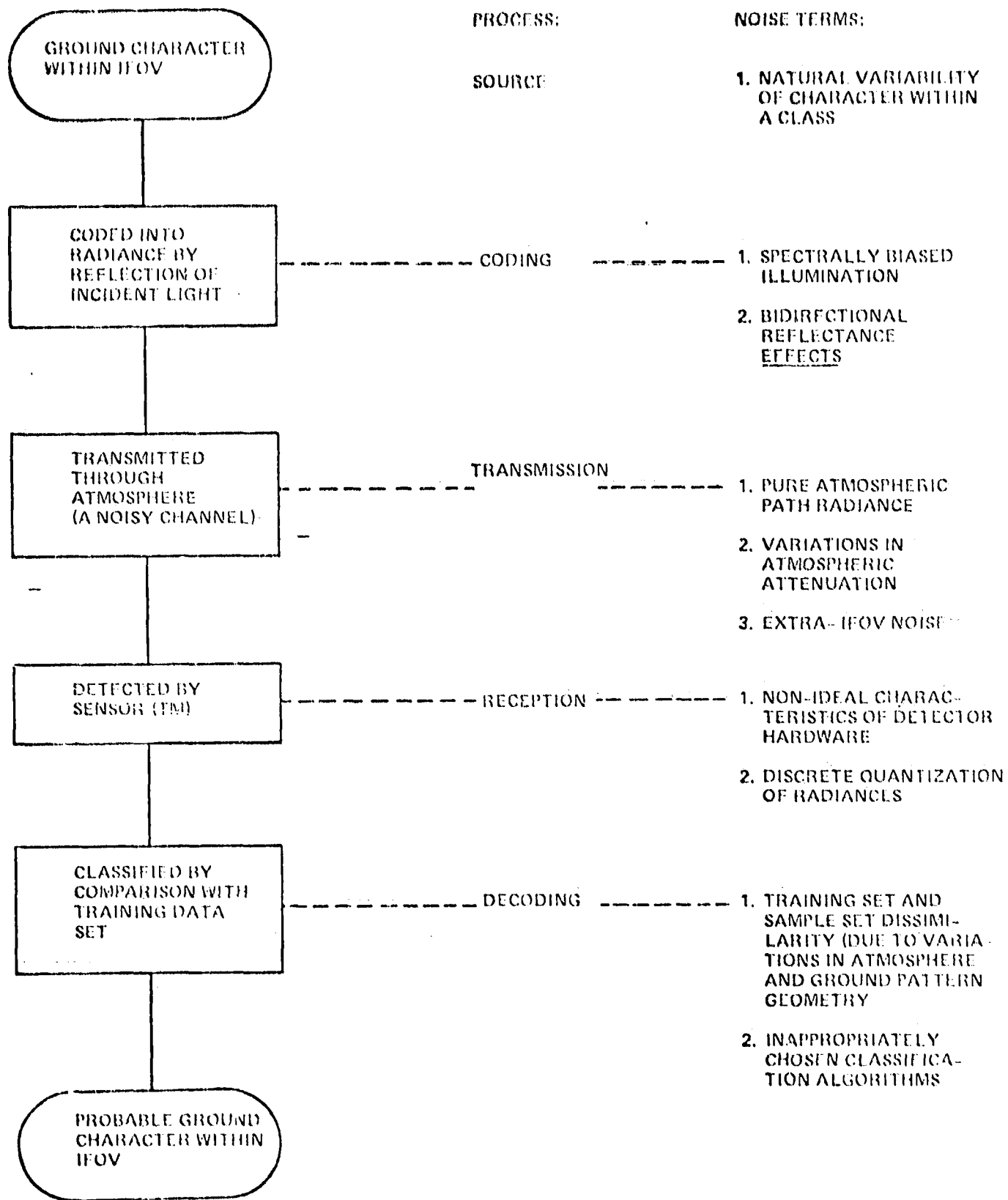


FIGURE 5.1. INFORMATION FLOW

The information is then transmitted. Transmission is identified with the radiative transfer process by which the light reflected from the ground finds its way into the remote detector. Again, noise is introduced which is related to the characteristics of the local atmosphere: radiance corresponding to pure atmospheric path radiance is introduced; variations in atmospheric attenuation constitute noise; noise is introduced by atmospheric scattering of light reflected from the ground outside the IFOV into the field of view.

The radiance is then detected by (non-ideal) hardware which introduces additional components of noise. The discretization or quantization of the detected radiances also can be viewed as a source of noise.

The received signal is then decoded. That is, the probable character of the ground within the IFOV is inferred by classification. This is essentially accomplished by comparing the sensed radiance with a truth data set (or training field data)-constructed from radiances accumulated over regions of known character. If the training data set has not been accumulated under conditions which precisely match those under which the current sampling is carried out, the mismatch can be considered as contributing noise. Variations both in the atmosphere and in ground pattern geometry can contribute to this noise term. Effects which are equivalent to noise can occur if an inappropriate or inefficient classification algorithm is employed (for example, using inappropriately chosen discriminants or cost functions).

The goals of a general theory of classification are essentially two-fold: 1) to evaluate quantitatively the impact of each of the sources of classification noise upon the achievable classification accuracy; 2) to devise new highly optimized classification schemes which are robust.

with respect to the expected sources of noise and consequent error. A third goal is also identifiable, given a sufficiently detailed and validated theory. This is the possibility that through the analysis of variances and bias of observational data sets, information relating to the state of the atmosphere can be extracted (as a byproduct of a classification effort). We might thus anticipate, for example, that we might be able to evaluate distribution weighted total aerosol burdens.

## 5.1 CLASSIFICATION

The key to the analysis of the impact of the atmospheric and ground plane variabilities upon classifications is the ability to construct the probability distribution density functions for radiances sensed above an arbitrary ground pattern. In this section, we will outline how this may be accomplished in the simplest cases. We will not, for the present, explore the various means for enhancing classification accuracy which involve (linear or non-linear) transformations of the radiances, but will assume that the radiances are used directly.

Consider, for the moment, the data collection process which results in a radiance distribution to be associated with a specified class of ground regions. A statistically significant sample of radiances is accumulated, for example, by recording the radiances near the centers of many large fields or by sampling many representative fields uniformly. Our present task is to provide a description of this kind of distribution taking into account the atmosphere and the ground plane geometry.

Let us digress, for a moment, in order to present the underlying mathematical formulae. Suppose that we wish to find the probability distribution density function associated with some function  $g(x)$  where  $x$  is a random variable and  $g(x)$  is determined once  $x$  is specified. Suppose that the probability density function for  $x$  is given by  $w(x)$ . We can define the characteristic function for  $g(X)$  by

$$F_g(\xi) = E \left\{ e^{2\pi i \xi g(X)} \right\} = \int_{-\infty}^{\infty} e^{2\pi i \xi g(x)} w(x) dx \quad (5.1.1)$$

where  $E\{\cdot\}$  denotes the expectation

The probability density distribution function for  $g$  is then given by the Fourier transform of the characteristic function:

$$\begin{aligned}
 W(g) &= F^{-1} [F_g] = \int_{-\infty}^{\infty} F_g(\xi) e^{-2\pi i \xi g} d\xi \\
 &= \int_{-\infty}^{\infty} d\xi \int_{-\infty}^{\infty} w(x) e^{-i\xi[g-g(x)]} 2\pi dx \\
 &= \int_{-\infty}^{\infty} w(x) \delta[g-g(x)] dx
 \end{aligned} \tag{5.1.2}$$

where  $\delta(x)$  is a Dirac delta function:  $\int_a^b \delta(x) dx = 1$  if  $a < x < b$   
 $= 0$  otherwise

and  $\int_a^b \delta(x-x_0) f(x) dx = f(x_0)$  if  $a < x_0 < b$   
 $= 0$  otherwise

We can apply this immediately to the problem of constructing a probability distribution-density for sampled radiances. Recall that the radiance above some point  $\underline{x}$  on the ground is given by

$$I(\underline{x}) = I_0 + \int A(\underline{x}-\underline{y}) g(\underline{y}) I_g(\underline{y}) d\underline{y}$$

While sampling,  $\underline{x}$  is a random variable so that  $I$  is also. If the sampling strategy is specified through a probability distribution density,  $w(x)$ , for the sampling point  $\underline{x}$ , then we may construct a characteristic function

for I using Equation 5.1.1 and thence, a probability distribution density function  $W(I)$  by Equation 5.1.2.

Thus we obtain the probability distribution density for sensing a radiance I:

$$W(I) = \int_{-\infty}^{\infty} d\xi \int_{\text{plane}} d\underline{x} w(\underline{x}) \exp\{-2\pi i \xi [I - I_0 - \int_{\text{plane}} A(\underline{x}-\underline{y}) g(\underline{y}) I_g(\underline{y}) d\underline{y}]\} \quad (5.1.3)$$

where  $w(\underline{x}) d\underline{x}$  is the probability of sampling within the region bounded by  $x_1 \pm \frac{dx_1}{2}$  and  $x_2 \pm \frac{dx_2}{2}$ . Equation 5.1.3 is then the single band signature of the region specified by the sampling function  $w(\underline{x})$ . It is straightforward to extend this formalism to any number of bands to obtain a multivariate probability density function expressing the signature obtained with a multispectral scanner.

In general, there remains one essential feature to be incorporated in the expression for  $W(I)$ . Even if each field to be sampled is in fact uniform, the reflectance of individual fields will have a statistical variation about some mean. In order to express this fact, we can write the reflectance as determined by the value of one or more random variables so that  $g(y)$  becomes  $g(\gamma_1, \gamma_2, \dots; y)$  and its statistical behavior is described through the probability density distribution assigned to the random variables  $\gamma_1, \gamma_2, \dots$ . We will illustrate this with an example a little later in the discussion. We should point out that the reflectance can vary randomly within a field. This effect, too, can be incorporated into the formalism.

We now have the basic tools to describe remote classification. In what follows, we will describe the process in its simplest form, leaving aside consideration of various embellishments (such as transformations of the radiances or including cost functions) which would becloud the basic issues. Initially, a training data set is sampled; that is, a statistically significant sample of radiances is accumulated for each class. For example, the signature of the class "corn" may be taken to be the distribution of intensities corresponding to pixels near the centers of large fields known (a priori) to be corn. These intensity distributions - one for each class - are then used to identify or classify radiances sensed over a new, a priori unknown region. One identifies an unknown pixel with that class whose training set distribution is closest in some sense to the radiance of the unknown pixel. For a multispectral system, the intensity distributions are multidimensional and the distances between the unknown point (with coordinates given by the intensities in each channel) and the training set distributions (usually using the means or centroids, or the peaks of the distributions as reference points) are measured in the multidimensional space.

## 5.2 CLASSIFICATION ERRORS

Errors in classification can be traced to a number of sources. First, there is the fact that the signatures of the various classes of the training set overlap to some extent. This is essentially irreducible and can be traced to a) micro-physical similarity between the overlapping classes (e.g., spectral signatures of leaves of plants in different classes are similar); b) heterogeneity within a class (signatures of say young corn and young cotton both contain the signature of the earth in which they are planted). When signatures overlap, the extent of overlap is a measure of the likelihood of error.

The second chief source of error is associated with dissimilarity between the conditions for which the training data set was accumulated and the conditions existing during the acquisition of data at an unknown site. The formalism we have developed provides a guide as to what is meant by "different conditions." We can trace signature variations to

- a) changes in the atmosphere (changes in  $I_o$ , the pure atmospheric path radiance; changes in the atmospheric spread function,  $A$ ; and changes in the ground illumination,  $I_g$ )
- b) changes in solar zenith angle (expressed through changes in  $I_o$  and  $I_g$ )
- c) changes in the environment surrounding the region or point to be classified (differing geometry or field size or changes in the character of nearby regions and the extent of these regions)



- d) changes induced by restricted sampling of the training data set (e.g., sampling unknown near field edge while sampling training fields only near their centers).

These are the error sources which may be analyzed through the application of Equation 5.1.3 and its generalizations.

Precise analysis of the impact of atmospheric scattering on classification accuracy depends, naturally, upon the details of the classification algorithm and would be specific with respect to them. Without assuming a particular classification algorithm, we can illuminate, qualitatively, some of the effects of atmospheric scattering and ground pattern geometry. We can approach this most simply by studying some simple examples which can be treated analytically. More quantitative results can be obtained through numerical studies using spread function obtained through modeling or by other means.

We will begin with an unrealistically simplified example and add realistic features progressively in order to highlight the various effects and develop some intuitive insight.

#### Example 1.

We will suppose that the albedo pattern of the ground is of the semi-infinite plane type; i.e.,  $g(x) = 1 \quad x \geq 0$   
 $= 0 \quad x < 0.$

Further, we will neglect, for now, the pure atmospheric path radiance (we assume  $I_0 = 0$ ). The form of the spread function will be

$$A(x) = \frac{u}{\pi} \frac{1}{u^2 + x^2}, \quad (5.2.1)$$

(chosen more for its analytic tractability than for its realism).

Note that the normalization of  $\Lambda$  is chosen so that  $\int \Lambda(x) dx = 1$ . For reasons of simplicity, we will restrict ourselves to one spatial dimension and one wavelength.

The intensity sensed above a point  $x$  will, with those restrictions be

$$I(x) = \int_{-\infty}^x \Lambda(y) r \, dy = \frac{r}{\pi} \left[ \tan^{-1} \frac{x}{u} + \pi/2 \right] \quad (5.2.2)$$

where  $r$  is the illumination of the ground, assumed constant here. The characteristic function is

$$F_I(\xi) = \int_{-\infty}^{\infty} w(x) \exp \left\{ 2\pi i \xi \int_{-\infty}^x \Lambda(y) r \, dy \right\} dx \quad (5.2.3)$$

With  $w(x)$  as the probability density function for sampling the intensity at  $x$ . We will assume that we sample uniformly over the ground (or rather, that we sample with uniform probability over a limited region) so that we may take

$$w(x) \begin{cases} = 0 & x < -L \\ = \frac{1}{2L} & -L \leq x \leq L \\ = 0 & x > L \end{cases} \quad (5.2.4)$$

Inserting this into 5.2.3 we obtain

$$F_I(\xi) = \frac{1}{2L} \int_{-L}^L dx e^{2\pi i \xi \frac{r}{2}} e^{2\pi i \xi \frac{r}{\pi} \text{TAN}^{-1} \frac{x}{u}} \quad (5.2.5)$$

The probability density for obtaining a value of  $I$  for the intensity while sampling is then given by

$$W(I) = \int_{-\infty}^{\infty} e^{-2\pi i \xi I} F_I(\xi) d\xi \quad (5.2.6)$$

Changing variables ( $y = \text{TAN}^{-1} \frac{x}{u}$ ), this becomes

$$W(I) = \int_{-\infty}^{\infty} e^{-2\pi i \xi I} \frac{1}{2L} \int_{\text{TAN}^{-1} \frac{-L}{u}}^{\text{TAN}^{-1} \frac{L}{u}} e^{2\pi i \xi \frac{r}{2}} e^{2\pi i \xi \frac{ry}{\pi}} \frac{u}{\cos^2 y} dy d\xi$$

so that

$$W(I) = \frac{u}{2L} \frac{\pi}{r} \frac{1}{\cos^2 \pi \left( \frac{1-r/2}{r} \right)} \quad (5.2.7)$$

$$\begin{aligned} & \text{for } \frac{r}{\pi} (\text{TAN}^{-1} \frac{-L}{u} + \pi/2) \leq I \leq \frac{r}{\pi} (\text{TAN}^{-1} \frac{L}{u} + \pi/2) \\ & = 0 \quad I > \frac{r}{\pi} (\text{TAN}^{-1} \frac{L}{u} + \pi/2) \\ & = 0 \quad I < \frac{r}{\pi} (\text{TAN}^{-1} \frac{-L}{u} + \pi/2) \end{aligned}$$

If samples are gathered only over  $L_0 \leq x \leq L_1$  the expression for  $W(I)$  becomes

$$W(I) = \frac{u}{(L_1 - L_0)} \frac{\pi}{r} \frac{1}{\cos^2 \pi \left( \frac{1-r/2}{r} \right)} \quad (5.2.7a)$$

$$\text{for } \frac{r}{\pi} \left( \tan^{-1} \frac{L_0}{u} + \pi/2 \right) \leq I \leq \frac{r}{\pi} \left( \tan^{-1} \frac{L_1}{u} + \pi/2 \right)$$

$W(I) = 0$  for  $I$  outside this range.

Note that  $\int_{-\infty}^{\infty} W(I) dI = 1$  as it must if  $W(I)$  is to be a

probability density distribution for  $I$ . The form of  $W(I)$  is evident, being a  $1/\cos^2 \frac{\pi}{r} (I - r/2)$  curve truncated at values of  $I$  corresponding to the extrema of the sampling range and normalized so that its integral is unity. This is illustrated in Figure 5.2 where we have set  $r=\pi$  for convenience. If the intensity is sampled uniformly from  $x=u$  to  $x=2u$ , the resulting probability density distribution for  $I$  has the form of the shaded region in the figure. For reference purposes, in Figure 5.3, we have plotted the intensity as a function of distance from the albedo boundary. The shaded region corresponds to the shaded region in Figure 5.2.

If  $I$  is sampled only over a limited region and if the distance of this region from the boundary increases,  $W(I)$  approaches a delta function, which is its form for an infinite uniform plane. We see now the effect of the boundary: it expands the signature associated with a uniform plane and skews it towards values of the intensity associated with the other side of the boundary.

FIGURE 5.2. INTENSITY PROBABILITY DENSITY DISTRIBUTION  
(EXAMPLE 1)

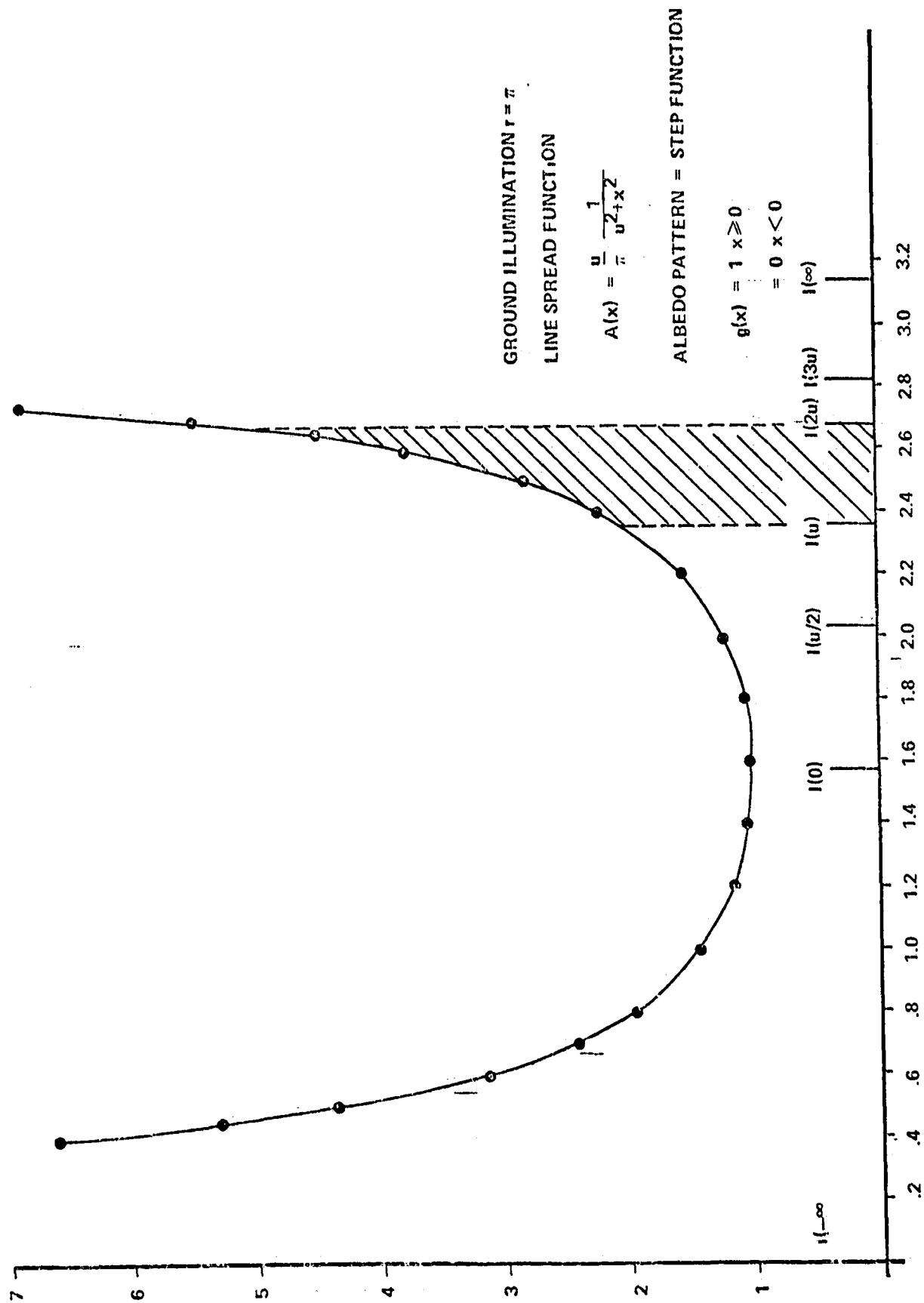
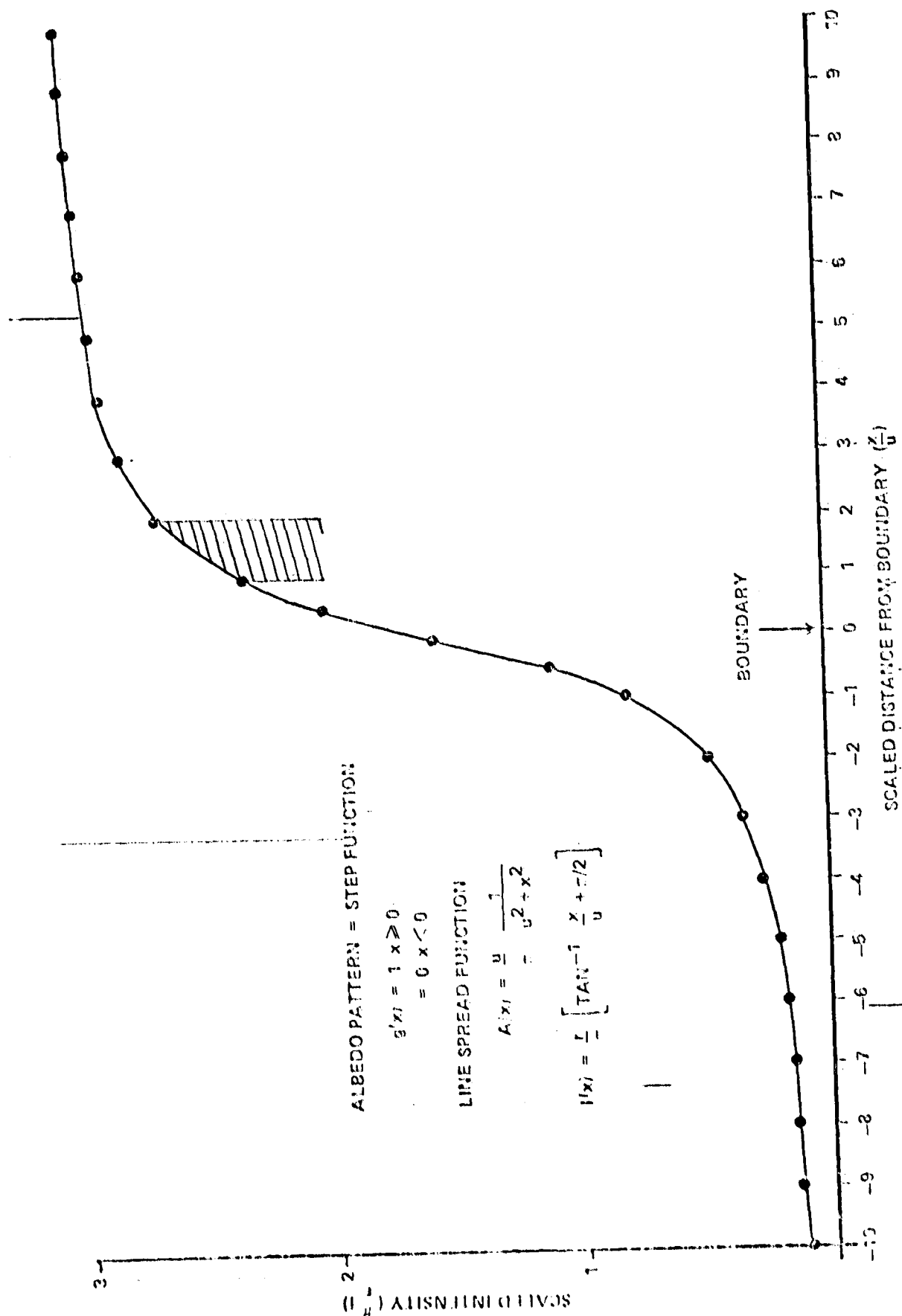


FIGURE 5.3. INTENSITY AS A FUNCTION OF DISTANCE FROM BOUNDARY



If the pure atmospheric path radiance is now taken into account, its addition merely shifts the l-axis of Figure 5.2. A glance at Table 3.1 shows that this shift can be quite substantial.

If the value of the albedos on either side of the boundary are changed, the result is a change in scale of the l-axis. Since Figure 5.2 depicts results for albedos 0 and 1.0, this scale change is always a scale compression for other albedo values.

Since, for any atmosphere of finite optical thickness, some photons are transported directly from the IFOV to the detector without scattering, realistic spread functions must contain a component proportional to a delta function. It is this delta function component which is responsible for the flattening out of the MTF at high frequency when the receiver field of view is infinitesimal.

#### Example 2.

The spread function for our first example may be modified to incorporate directly transmitted photons:

$$A(x) = (1-C) \frac{u}{\pi} \frac{1}{u^2 + x^2} + C \delta(x). \quad (5.2.8)$$

Note that in physical cases the constant C is proportional to  $\exp(-\tau)$ , where  $\tau$  is the atmospheric optical thickness. Equation 5.2.2 for the intensity is modified to

$$I(x) = (1-C) \frac{r}{\pi} \left[ \text{TAN}^{-1} \frac{x}{u} + \pi/2 \right] + Cr H(x) \quad (5.2.9)$$

where  $H(x)$  is the Heaviside function (a unit step at the origin):

$$H(x) = 1 \quad x > 0, \quad H(x) = 0 \quad x < 0, \quad H(0) = .5$$

The effect of this change in the form of  $I$  is to split the probability density distribution for  $I$  into two parts, separated by an amount proportional to  $C$ .  $W(I)$  is given by

$$W_I(I) = \int_{-\infty}^{\infty} W_X(x) \exp \left\{ -2\pi i \xi \left[ (1-C) \frac{r}{\pi} \left( \text{TAN}^{-1} \frac{x}{u} + \pi/2 \right) - Cr H(x) \right] \right\} dx d\xi \quad (5.2.10)$$

or

$$W_I(I) = \left( \frac{1}{I_1 - I_0} \right) \frac{u\pi}{(1-C)r \cos^2 \left[ \frac{\pi}{r(1-C)} \left( C - \frac{r(1-C)}{2} \right) \right]}$$

$$\text{for MAX} \left| 0, \frac{r(1-C)}{\pi} \left( \text{TAN}^{-1} \frac{I_0}{2} + \frac{\pi}{2} \right) \right| \leq 1 \leq$$

$$\text{MIN} \left| \frac{r(1-C)}{2}, \frac{r(1-C)}{\pi} \left( \text{TAN}^{-1} \frac{I_1}{2} + \frac{\pi}{2} \right) \right|$$



$$W_I(l) = \left( \frac{1}{l_1 - l_0} \right) \frac{\pi}{(1-C)r \cos^2 \left[ \frac{\pi}{r(1-C)} \cdot \left( 1 - \frac{r(1+C)}{2} \right) \right]}$$

$$\text{for } \text{MAX} \left[ \left( \frac{r(1+C)}{2} \right), \frac{r(1-C)}{\pi} \left( \text{TAN}^{-1} \frac{l_0}{u} + \pi/2 \right) + Cr \right] \leq l \leq$$

$$\text{MIN} \left[ \frac{r(1-C)}{\pi} \left( \text{TAN}^{-1} \frac{l_1}{u} + \pi/2 \right) + Cr, r \right]$$

$$= 0 \quad \text{for all other values for } l$$

$W_I(l)$  is shown in Figure 5.4. - It is clear that the impact of the direct transmission term (the delta function term) is to increase the separation of the signatures and hence to reduce classification errors.

We must point out that at this stage we have not yet included in our example the fact that the field of view of the sensor is finite. It is therefore of interest to make a qualitative comparison of the MTF's for our example spread functions with the MTF's computed for infinitesimal fields of view and realistic atmospheres. The MTF's for our example spread-function are shown in Figure 5.5. The qualitative-similarity with actual MTF's is striking (see Figures 4.7 and 4.8). Naturally, quantitative agreement is not to be expected.

If the sensor has uniform sensitivity across a finite field of view, the effect on the signature (or  $W(l)$ ) is to fill the gap between  $l=r(1-C)/2$  and  $l=r(1+C)/2$ ;  $W(l)$  becomes equal to a non-zero constant in this region.

FIGURE 5.4. INTENSITY PROBABILITY DENSITY DISTRIBUTION FUNCTION

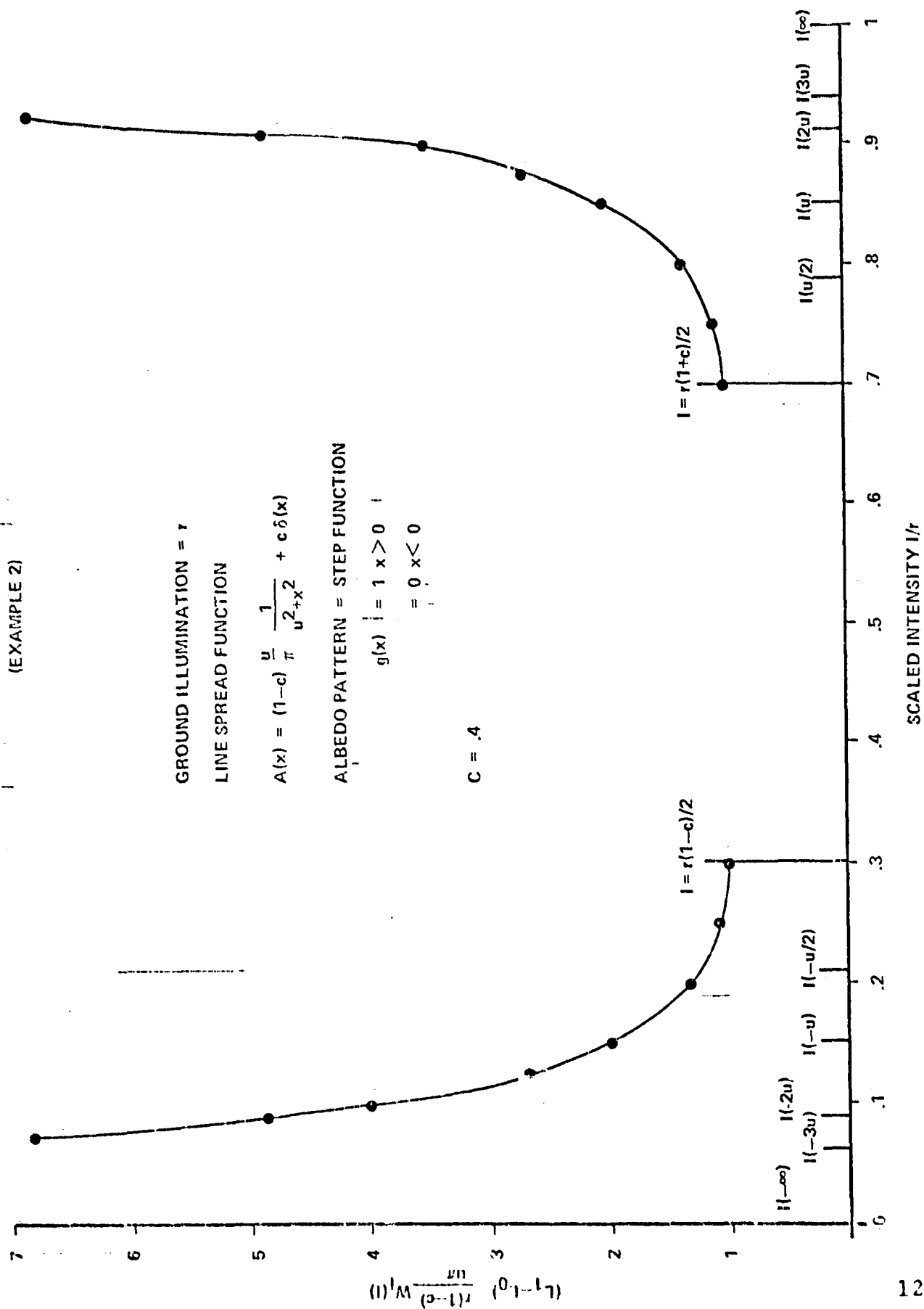
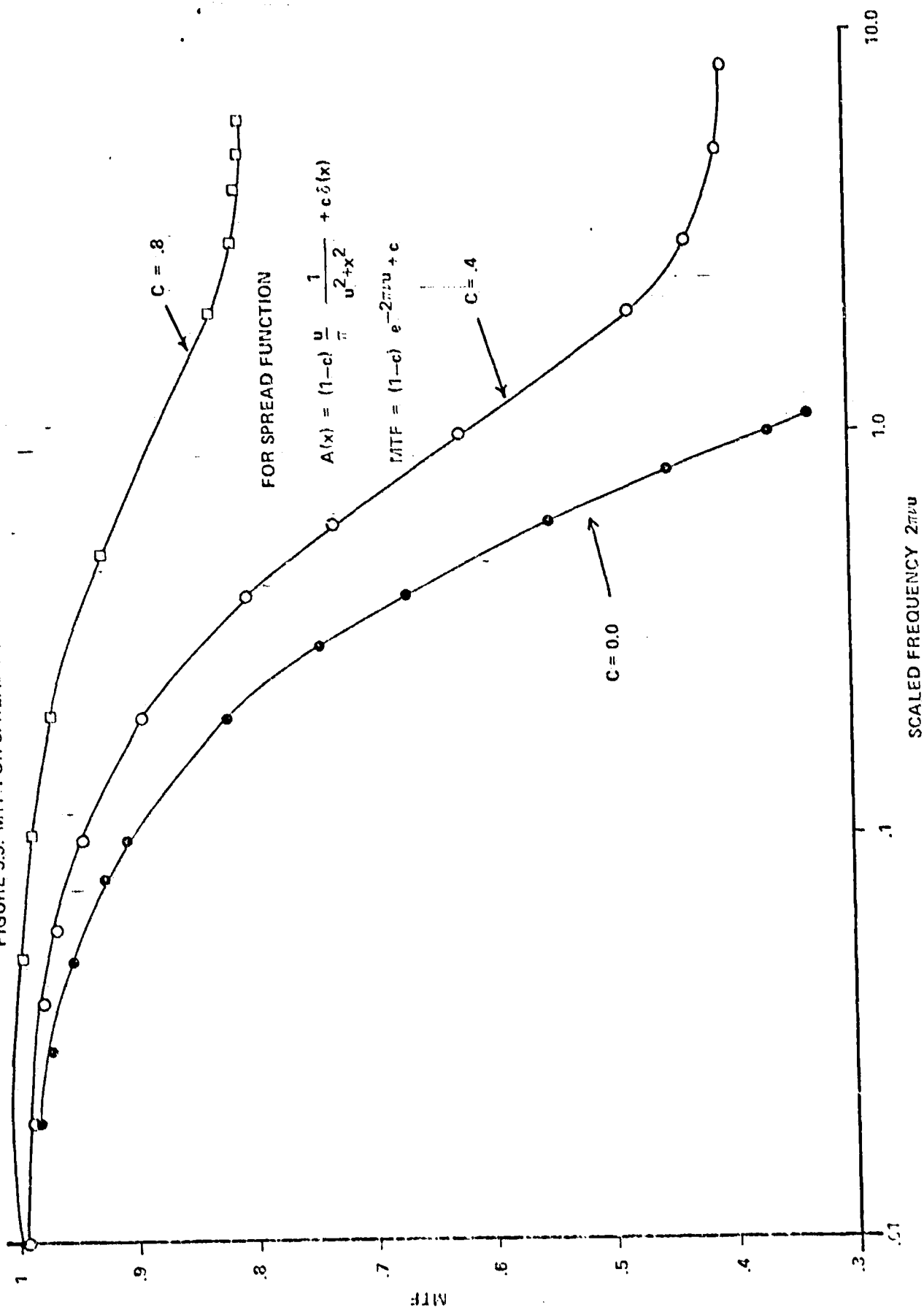


FIGURE 5.5. MTF FOR SPREAD FUNCTIONS OF EXAMPLES 1 AND 2



The examples treated heretofore have been artificial to the extent that the physical variability of the ground albedo within a class or amongst samples from a single area has been omitted. In order to provide for this variability, one must integrate over an ensemble of albedos. The ground albedo is taken to be a function of a random variable (or a set of random variables) and has, for each class, a probability distribution density function. Introducing this concept, the probability density distribution for the intensity becomes

$$W(I) = \int w(x) \prod_{j=1}^n w_{gj}(\gamma_j) \exp\{-2\pi i \xi [I - I(x, \gamma_1, \gamma_2 \dots \gamma_n)]\} \cdot dx d\gamma_1 d\gamma_2 \dots d\gamma_n \quad (5.2.11)$$

where

$$I(x, \gamma_1, \gamma_2 \dots \gamma_n) = I_0 + \int_{-\infty}^{\infty} A(x-y) g(y; \gamma_1, \gamma_2 \dots \gamma_n) r dy$$

The meaning of  $g(y; \gamma_1, \gamma_2 \dots \gamma_n)$  can be made clear by an example. Suppose we wish to describe the distribution of intensities obtained by sampling a family of semi-infinite planes. Let the albedos of the bright and dark sides have statistical variation about some mean values. Then

$$I(x, \gamma_1, \gamma_2) = I_0 + \int_{-\infty}^0 A(x-y) \gamma_1 r dy + \int_0^{\infty} A(x-y) \gamma_2 r dy \quad (5.2.12)$$

and the distributions of  $\gamma_1$  and  $\gamma_2$  are specified by probability density distribution  $w_{g_1}(\gamma_1)$  and  $w_{g_2}(\gamma_2)$  which might, for example be Gaussian:

$$w_{g_1}(\gamma_1) = \frac{1}{\sqrt{2\pi}\sigma_1} e^{-(\gamma_1 - \bar{\gamma}_1)^2 / 2\sigma_1^2}$$

$$w_{g_2}(\gamma_2) = \frac{1}{\sqrt{2\pi}\sigma_2} e^{-(\gamma_2 - \bar{\gamma}_2)^2 / 2\sigma_2^2}$$

or uniform

$$w_{g_1}(\gamma_1) = \frac{1}{g_1' - g_1''} ; w_{g_2}(\gamma_2) = \frac{1}{g_2' - g_2''}$$

(where  $g_1', g_1''$  and  $g_2', g_2''$  are upper and lower limits of the allowed range of variation). \_\_\_\_\_

The impact of introducing variability in the albedos is essentially to smear out the probability distribution density for I. This is easy to see for the case of uniform planes. In this instance, the intensity is given by

$$I = I_0 + \gamma r$$

If  $\gamma$  has a Gaussian distribution, we obtain

$$W(I) = \int w(x) \frac{1}{\sqrt{2\pi}\sigma} e^{-(\gamma - \bar{\gamma})^2 / 2\sigma^2} \exp\{-2\pi i \xi [I - I_0 - \gamma r]\} dx dr d\xi$$

$$\begin{aligned}
&= \int w(x) \frac{1}{2\pi} e^{-(\gamma - \bar{\gamma})^2 / 2\sigma^2} \delta[I - I_0 - \gamma r] d\gamma dx \\
&= \frac{1}{\sqrt{2\pi}} \frac{1}{r\sigma} e^{-\left(\frac{I - I_0}{r} - \bar{\gamma}\right)^2 / 2\sigma^2}
\end{aligned}$$

or

$$W(I) = \frac{1}{\sqrt{2\pi}} \frac{1}{r\sigma} e^{-[I - (I_0 + \bar{\gamma}r)]^2 / 2r^2\sigma^2}$$

We obtain, as might be expected, a Gaussian distribution for  $I$  with mean  $I_0 + \bar{\gamma}r$  and variance  $r^2\sigma^2$  where  $\sigma^2$  is the variance of the distribution of albedos and  $r$  is the illumination of the ground (which here, for simplicity, has been assumed to be independent of albedo). This is to be compared with the result corresponding to non variable albedos for the same infinite plane case:-

$$W(I) = \delta(I - I_0 - \gamma r)$$

Even the simple spread function used for examples 1 and 2 yields expressions which are analytically difficult when variations in the albedo are considered. We yet may gain some insight into the impact of an albedo boundary on the signatures, however. The intensity probability density distribution for an ensemble of uniform planes turned out to be unskewed because the intensity probability distribution for a single uniform plane is symmetrical - it is a delta function. If, on the other hand, we consider averaging the intensity probability distributions for examples 1 and 2 over ensembles of albedos, the skew in, say, the bright side distribution will be reflected in a skew in the averaged distribution.

This has important consequences in the interpretation of training data sets. The intensity probability distributions obtained from observations of a patchwork earth will be smeared or spread by atmospheric scattering and will be skewed towards the distribution peaks corresponding to the surroundings of the region whose signature is being measured. The degree of skewness in the distributions has a direct bearing upon the precise choice of classifier (e.g., on the choice of thresholds or discriminants).

### 5.3 RECOMMENDATIONS

We should, at this stage, make a few specific recommendations in regard both to classification procedures and to analytical work which should be taken up.

The atmospheric effect which is most likely to have a deleterious effect upon classification accuracy is the variability of the pure atmospheric path radiance: it provides a shift in single band intensities which can be large with respect to class separation and can therefore significantly impact classification accuracy. As yet, we have discovered no clean, simple means for estimating this term absolutely. There is one method, however, which might provide a way to minimize its impact. If the intensity probability distribution for an entire unknown region is compiled using methods (sampling strategies) which match those used to compile the training set, a correlation of one with the other should yield a value for the difference of  $I_0$  between the two cases. When this difference is subtracted uniformly from the unknown data, classification accuracies should improve. This procedure is, however, sensitive to differences in field size distribution between the data sets.  $I_0$  should be estimated in this way independently for each sensor band. By examining the behavior of this correction with wavelength, some information relating to aerosol burden may be obtained. To enhance the value of this type of information and to provide the best estimates of the corrections to be applied to unknown data sets, the training data set should be acquired when the turbidity is minimum. If this is done, the correlations between  $I_0$  and, for example, the parameters  $T$  and  $S$  can be used to obtain values for  $T$  and  $S$  and enable one to transform the unknown data to obtain equivalent albedos. The probability density distribution of the data thus transformed is likely to be considerably cleaner and result in higher classification accuracies.



The shifts and skew in the intensity probability distributions introduced through atmospheric scattering and finite field size effects should be taken into account in the specification of cost functions and thresholds used to classify the data.

Realistic estimates for the full spread function should be used to study the precise impact upon accuracy of any given classification algorithm (including transformations of the data). Quantitative results can most economically and precisely be obtained through judicious modeling.

A quantitative treatment of remote classification should be pursued along the lines we have indicated. Elements which remain to be included are: 1) the joint impact of the forms of spectral dependence of the reflectances for the various classes; 2) the impact of the quantization of intensities; 3) the impact of instrumental noise; 4) quantification of information content and effective channel capacity; 5) direct evaluation of equivocation probabilities. Among other results, we might be able to specify simple transformations of the multispectral data which improve classification accuracy.

## SECTION 6.0

### CONCLUSIONS

The simulation studies reported here highlight the presence of a number of effects which are likely to be troublesome if disregarded in the analysis of the data to be acquired by the Thematic Mapper. Our analysis of these effects has, in addition, provided some concrete suggestions for techniques which might be employed to minimize or eliminate many of these problems.

We have seen that the presence of an albedo boundary on the earth may affect the radiances associated with points on the ground as much as 1 km away from the boundary. This is due primarily to light which has been reflected from the ground outside the IFOV and scattered by the atmosphere into the sensor. Thus, the effect is enhanced by increases in the optical thickness of the atmosphere (increasing turbidity and/or decreasing wavelength).---Because of variations in the illumination of the ground associated with ground scattered light, the boundary effects are more pronounced on the bright side of a boundary.

For the purpose of analysis, we have seen that it is very useful to characterize the remotely sensed radiances by three functions (in addition to the ground albedo pattern):  $I_0$ , the pure atmospheric path radiance;  $A(r)$  the atmospheric spread function; and  $I_g(r)$ , the ground illumination. We note that all of these are influenced by the optical state of the atmosphere;  $I_0$  and  $I_g$  are functions of the solar zenith angle; and  $I_0$  and  $A$  are functions of the receiver nadir angle.

If no ground truth or auxiliary data is available, we have seen that it is generally not possible to separate the ground albedo  $g(r)$  from the ground illumination,  $I_g$ : they

always appear as a product:  $g(r) I_g(r)$ . We have, however, suggested indirect means for mitigating this difficulty. If the ground albedo is nearly uniform or if the variations in the ground albedo are rapid with respect to the range of the spread function, the radiances may be transformed by the non-linear transformation of equation 3.4 provided that estimates of  $I_0$ ,  $T$ , and  $S$  are available. The resulting effective albedos are then directly related to the physical albedo through convolution with the normalized spread function. Since  $I_0$ ,  $T$ , and  $S$  appear to be approximately linearly related, a knowledge of  $I_0$  suffices to determine  $T$  and  $S$  approximately. From our analysis of the classification problem, it appears that an operationally useful estimate of  $I_0$  may be obtained from the correlation of the signatures of unknown data sets with training field data sets (taking care that the data to be correlated are selected in similar ways). An estimate of the spread function must then be made in order to deconvolve the extra IFOV radiance. This might be done in several ways. One method which might prove to be operationally feasible is to use the gradient of the intensity near field boundaries as a guide to the selection of a candidate spread function from a dictionary of spread functions (previously compiled through modeling). Because of finite field size effects, only the inner part of the spread function can be estimated using the intensity gradient method. It might therefore be possible to specify the inner spread function through measurement of intensity gradients and to obtain the remainder through analytic continuation if the tail of the spread function can be characterized. The atmospheric spread function has not yet been sufficiently thoroughly studied to permit this, however.

Once an operationally adequate estimate of the spread function has been made, there remains the problem of deconvolution. This can be done numerically using fast Fourier transform techniques. Numerical deconvolution is, on the other hand, extremely time consuming and costly when very

many pixels must be processed. A better approach would be to use optical techniques for the deconvolution.

This study has provided some of the tools which would be needed for the implementation of image enhancement techniques. We have compiled a short catalog of MTF's in a form suitable for combination with actual instrumental MTF's and construction of spread functions for the sensor-atmosphere system. Our model analysis of the behavior of the intensity near the boundary of two semi-infinite planes indicated the presence of an extended range over which the intensity varied linearly in a semi-log plot:  $I \sim a + b \ln x$ . This implies that the line spread function possesses a  $1/x$  behavior over this range and that the point spread function has an approximate  $1/r^2$  behavior in a corresponding range. Preliminary analysis further indicates that the spread function should decay exponentially at large distances.

There are a number of aspects of the remote sensing radiative transfer problem which we have not yet examined. The impact of variability in aerosol type should be assessed. We have, in this study, restricted ourselves to a single size distribution and refractive index. The specific influence of nearby clouds remains to be investigated. Further, it is probable that the bidirectional reflectance properties of various kinds of target fields can have a significant impact on sensed radiances and upon classification errors. This should definitely be addressed in future studies.

We believe that further work should be done to implement the classification formalism which was briefly considered in Section 5. As part of this effort, the spread function and practical means for evaluating it should be studied. Our formalism would provide the easiest, least expensive and most precise means for analyzing the impact upon classification error of, for example, errors in the spread function.

quantization noise, specific sampling strategies, ground illumination effects, specific transformations of the data (such as conversion to effective albedo), specific choices for discriminants, etc. Within this framework, proposed schemes for classification improvement could be thoroughly tested under precisely controlled model conditions. The results of these tests could then be verified by trial with observational data.

## REFERENCES

1. W.A. Pearce, CTTRANS: A Monte Carlo Program for Radiative Transfer in Plane Parallel Atmospheres With Imbedded Finite Clouds - Development, Testing, and User's Guide. Final contractor report under NASA Contract NAS 620857, December 1976 (prepared for NASA Goddard Space Flight Center, Greenbelt, Maryland).
2. C. Cox and W.J. Munk, J. Opt. Soc. Am. 44 838-850 (1954).
3. GSFC Specification: Thematic Mapper System and Associated Test Equipment. GSFC No. 5-726-9. Goddard Space Flight Center, Greenbelt, Maryland, May 1976.
4. The approach adopted here parallels an approach to photographic images outlined in, "The Structure of the Developed Image," by E.H. Perrin in The Theory of the Photographic Process, C.F. Kenneth Mees and T.H. James, ed.--MacMillan Co., New York, New York, 1969 (p499).
5. M.M. Sondhi, Proc. IEEE 60 842 (1972). Several other papers in this special issue of Proc. IEEE are also relevant and interesting.
6. See for example, An Introduction to Statistical Communication Theory, David Middleton, McGraw Hill Book Co., New York, N.Y., 1960.